Final Research Performance Progress Report

High Frequency Transverse Combustion Instabilities in Low-NOx Gas Turbines

Submitted: 11/11/2022

WORK PERFORMED UNDER AGREEMENT

DE-FE0031285
Project Period: 10/01/2017 – 06/30/2022

SUBMITTED BY

Georgia Tech Research Corporation
505 Tenth St. NW
Atlanta, GA – 30332-0420
DUNs #: 09-739-4084

PRINCIPAL INVESTIGATOR

Principal Investigator: Timothy C. Lieuwen
P: 404.894.3041
F: 404.894.2760
tim.lieuwen@aerospace.gatech.edu

SUBMITTED TO

U. S. Department of Energy
National Energy Technology Laboratory

Mark Freeman
Mark.Freeman@netl.doe.gov

Introduction

This program addresses the topic of combustion instabilities under the goal of developing "Low-NOx Combustion Technology for 'Air-Breathing' Advanced Turbines". With recent advances in high-temperature withstanding materials, the push towards higher efficiency has resulted in efforts to design high temperature, low NOx gas turbines. The development of such low NOx systems is often plagued with combustion instabilities. These instabilities manifest with acoustic modes that are longitudinal, transverse or both. A large body of literature and work exists addressing the underlying mechanisms and models for longitudinal instabilities and these have been successfully implemented in the design tools for low NOx gas turbines. The flame response aspect of the thermoacoustic feedback loop was often modeled in an acoustically compact framework since for low frequencies, the flame length scale was small compared to the acoustic wavelength. This enabled simplification where the modeling focused only on the overall flame response and not the local spatial distribution of the flame response. In addition, additional mechanisms such as the direct effect of pressure fluctuations on the flame response could be neglected. In contrast, high frequency instabilities which often are transverse in nature, have received relatively less attention in the literature. The flame is no longer acoustically compact and thus the local distribution of heat release must be accurately understood. The flame responds to velocity fluctuations, equivalence ratio fluctuations as before, but also to pressure fluctuations through kinetic effects. These aspects of high-frequency instabilities make it a challenging problem that requires a detailed elucidation of the underlying mechanisms and creating models for them. In this program we significantly improved the understanding of these instabilities through a combination of experiments (informed by interactions with OEMs), modeling of measured data and reduced order modeling of flame response. The results from the program can be used as basis for robust design tools that are essential for successfully developing gas turbines that operate in an environmentally acceptable manner with mitigation strategies for high-frequency instabilities.
The proposed work in this program was naturally broken down into tasks:

1. Task-1 focused on the Project Management and Planning that was continuously evolved to achieve the goals of the program.
2. Task-2 focused on the design of an experimental rig with room for optical and pressure diagnostics for measurements in an industry relevant, but lab-scale multi-nozzle can combustion system. The results from these measurements were also modeled using well-established modal dynamics equations showing the conditions under which different modal interactions occurred – specifically, mode suppressions, quasi-periodicity, dynamics of spin ratio (spinning vs standing waves) under different operating conditions of fuel-staging.
3. Task-2 focused on reduced order modeling for the flame response under both the velocity-coupled and pressure-coupled mechanisms. These were performed through a combination of phenomenologically simplified flame response equations solved analytically and numerically. The resulting flame response models illustrated the differences in flame response across various transverse modes as well as difference in individual nozzle responses to the same transverse mode depending upon the location of the nozzle in the combustor head-end. These results were then collectively used to design an optimization tool that can optimize for nozzle positioning given operating parameters and also optimize for operating parameters for fixed nozzle positions. This optimization tool can serve as a robust initial design tool for OEMs to design the combustion system and its operating parameter space to minimize the effect of transverse instabilities.

Task 2 – Experimental Characterization of High-frequency Transverse Instabilities

As part of this Task, a lab-scale multi-nozzle can combustor was designed to ensure that a high-frequency transverse mode gets self-excited and identifying combustor design and operating parameters to achieve the same.

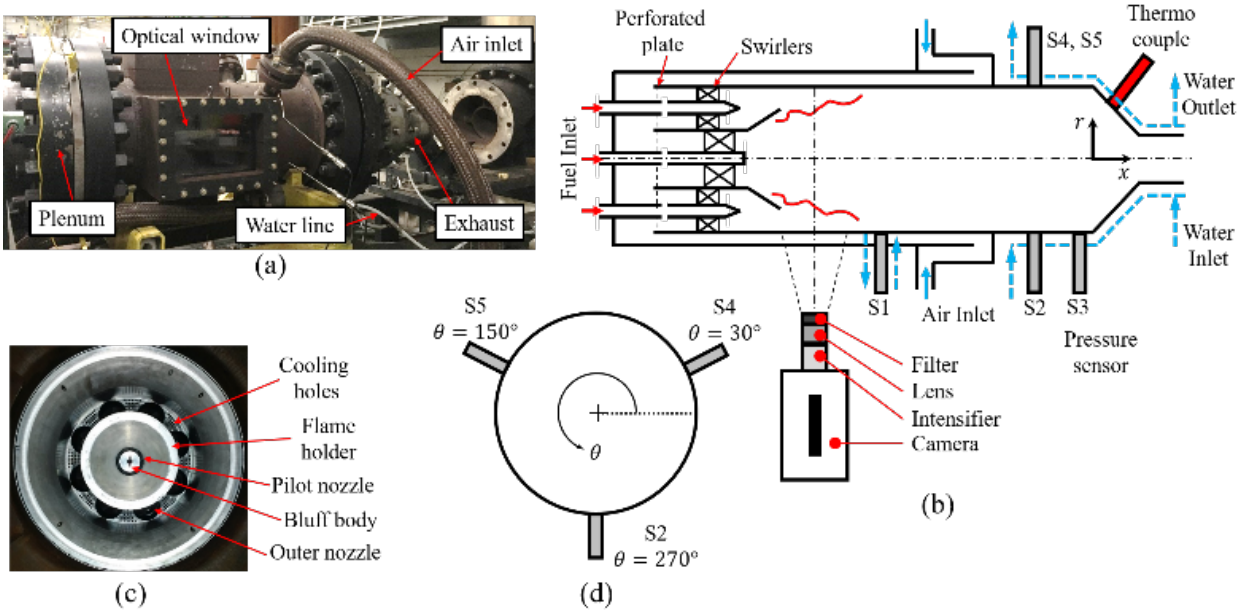

Figure 1 – Experimental rig: (a) image of the combustor (b) side-schematic of the combustor and camera setup (c) image of multi-nozzle (d) sensor configurations.

Figure 1 shows the experimental facility. Air from four inlets enters near the axial midpoint of the rig and flows through an annular section in the upstream direction, cooling the chamber wall. At the front of the test article, the preheated air passes through one of eight outer and center pilot nozzles (Figure 1(b)). Each nozzle consists of a swirler and fuel injector. The swirl direction of the pilot and outer nozzles is clockwise (CW) and counter-clockwise (CCW), respectively. Fuel flow through the outer and pilot is controlled separately, quantified by the pilot ratio, $PR = \frac{\dot{m}_p}{\dot{m}_p + \dot{m}_o}$ where $\dot{m}_p$ and $\dot{m}_o$ are the fuel flow rate through the pilot and a single outer nozzle, respectively. The combustor liner consists of a quartz tube and a metal liner whose diameter is 0.29 m and total length is 1.2 m, respectively. The combustor product accelerates near the downstream contraction area and exits the system through the water-cooled exhaust.

Five 6021A Kistler pressure sensors (sensitivity: 6200 pC/kPa, range: 10 MPa, accuracy: ±10%) are flush mounted at different axial and azimuthal locations (Figure 1(b) and (d)), and they are connected to the Kistler 5181A differential charge amplifier (sensitivity: 10mV/pC, range: ±10V, accuracy: ±0.2%). A pressure in time series is recorded at the sampling frequency of 20 kHz, and then the signals are digitized by a National Instrument (NI 9215).

CH* chemiluminescence imaging is performed at various test conditions, with the camera positioned level, and perpendicular to the centerline of the combustion chamber. (Figure 1(b)) A Photron Fastcam SA-X2 is used to capture video data at a sampling rate of 12,500 Hz, with a resolution of 1024x1024 pixels. At this resolution, the camera's on-board hard drive is capable of

storing 5452 images. Two partitions are used, so each partition is 2726 images spanning a time 0.218 sec, each. Image decks are downloaded from the camera hard drive to an external hard drive through a gigabit Ethernet cable. A Nikon Nikkor 35 mm diameter lens with focal length of 50 mm is used. Incident light is first optically filtered using a lens with peak wavelength transmission at 434 nm, and then intensified using a LaVision High Speed IRO, with the gate set to the full width of the open camera shutter. The optical filter, lens, IRO, and camera are all attached end to end in this order (Figure 1(b)). In each take, the optical inlet to the filter is placed approximately 0.3 m from the centerline of the test section.

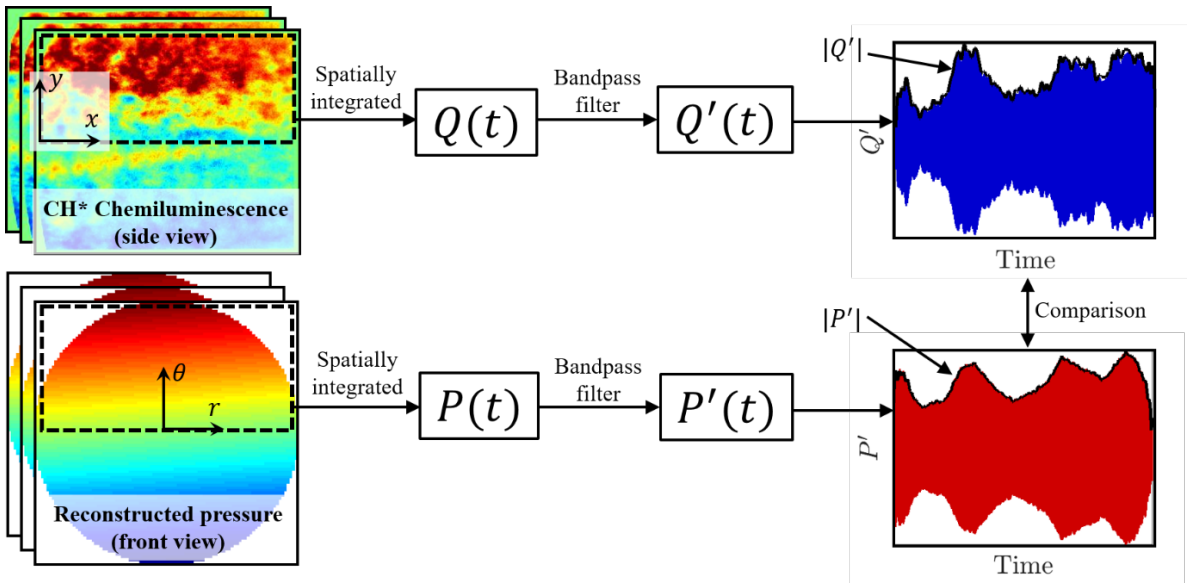

Figure 2 – Post-processing procedure of the image and reconstructed pressure time series.

The objective of CH* images is to compare the heat release fluctuation data with the pressure signal. It is assumed that the intensity of the images is proportional to the heat release rate. However, since the camera records the line-of-sight integrated images, the pressure must be reconstructed and integrated equivalently. Therefore, the following quantities are evaluated from the images and the pressure signal:

$$Q(t) = \int_{x_1}^{x_2} dx \int_{0}^{R} dy \underbrace{\int_{-R}^{R} q(x,y,z,t)dz}_{=Q_{img}(x,y,t)} \tag{1}$$

$$P(t) = \int_{0}^{\pi} d\theta \int_{0}^{R} p_{r\theta}(r,\theta,t) r dr \tag{2}$$

Here, Q_{img} is the heat release of each image, which is already integrated in z-direction, $x_{1,2}$ are the axial coordinate of the left and right edges of the image, and Q is the top half integrated heat release. In short, Q is the sum of the intensity of the top half image. $p_{r\theta}$ is the reconstructed pressure distribution (reconstruction method is introduced in the past report.) in the azimuthal and radial space at the axial location of sensor 2, and P is the top half integrated pressure fluctuation. Q and P are then bandpass filtered at around their peak frequencies in a similar way described in the past report, given by Q' and P', respectively. Lastly, the magnitude and the phase of each signal

are extracted by taking the Hilbert transform. The procedure is described in Figure 2. One can expect that if the heat release fluctuation is positively correlated with the pressure signal, then the magnitude of heat release is maximized when the nodal line is horizontal ($\theta_n = 0$), and vise versa. For comparison with heat release data, the pressure data is down sampled from 20 kHz to 12.5 kHz.

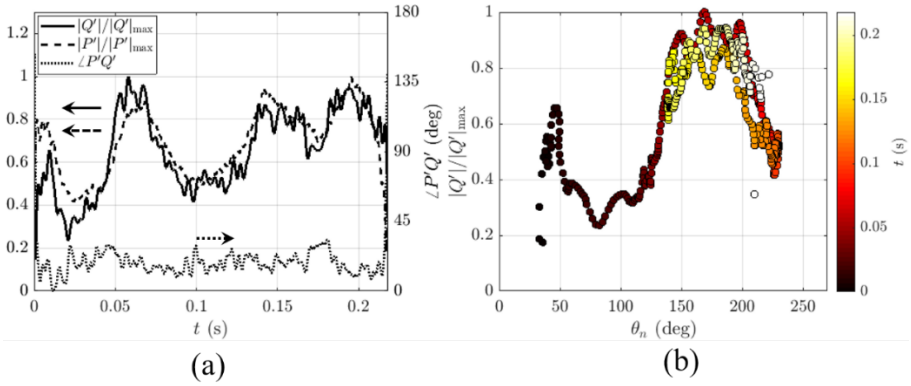

Figure 3 – (a) comparison between the heat release fluctuation and reconstructed pressure signal. (b) Magnitude of heat release fluctuation with respect to nodal line position. The color denotes the time series.

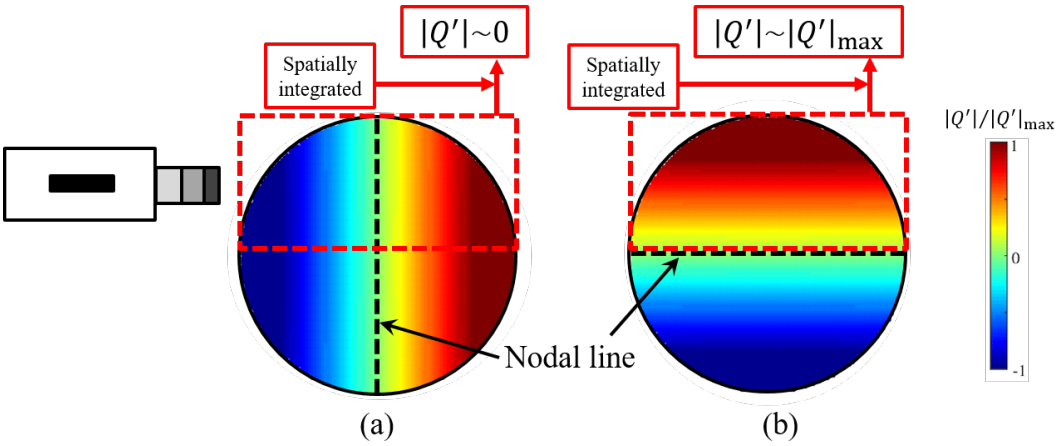

Figure 4 – Integrated heat release fluctuation with respect to nodal line position: (a) vertical, (b) horizontal.

The magnitudes and the phase difference between the reconstructed pressure and the heat release fluctuation are described in Figure 3. Figure 3(a) shows a positive correlation between the magnitudes of these two quantities. In addition, the phase difference between two quantities in Figure 3(b) is $\angle P'Q' = \angle P' - \angle Q' \approx 20°$. However, recall that the axial location of heat release fluctuation is different from that of the reconstructed pressure, i.e., CH* images are taken at upstream near the flame region, whereas the pressure is reconstructed at sensor 2 downstream. Considering the phase lag between sensor 1 and 2 (which is presented in the past report), the corrected phase difference is about $\angle P'Q' \approx -30°$. These two observations clearly satisfy the Rayleigh criterion where $|\angle P'Q'| < 90°$.

Figure 3(b) illustrates the magnitude of heat release fluctuation with respect to nodal line location, and the color denotes the time duration. The beginning and ending portion of the data is

distorted due to Hilbert transform. The nodal line starts at 50° and oscillated at around 180°. Notice that the magnitude is minimum when the nodal line passes 90°. This is because when the nodal line is vertical, the top half of the heat release fluctuation cancels out (Figure 4(a)). The reason for the magnitude not being zero is that the mode is not pure standing, but rather a mixed mode ($SR \approx 0.4$). On the other hands, the magnitude is maximized when the line oscillates at around 180°. One can also observe that as the line deviates from 180°, the magnitude decreases, and vice versa. This observation apparently shows the effect of the nodal line location on the heat release fluctuation. In addition, unlike the longitudinal mode where the nodal line location in axial position is relatively fixed, the nodal line for the azimuthal mode rotates and/or oscillates vigorously during the instability, which leads the fluctuation in pressure magnitude measured at a fixed azimuthal location.

The first transverse mode of this combustor occurs at about 1600 Hz. In this study, we present results from two different operating conditions, which are summarized in Table 1.

Table 1 Operating test conditions

Case	Preheat temp. (K)	Air flow (kg/s)	Equiv. ratio	Thermal Power (MW)	Combustor pressure (kPa)	Pilot ratio	Dominant mode
1	625	1.45	0.55	2.11	185	0.095	SW
2	625	1.34	0.55	1.95	172	0.090	CW

The four sensors allow us to decompose the measured pressure into the instantaneous amplitude and relative phases of the CW and CCW waves. For each of the two test points analyzed here, the combustor was set at that condition for at least 40 seconds and the last 30 seconds data was used for the analysis. The data is then filtered with a bandpass filter of width ± 30 Hz around the peak frequency of 1600 Hz to isolate the first transverse mode from the broadband noise. The filtered signal is Hilbert transformed to convert it into an analytic pressure signal, given by $\hat{p}$. The analytic signal is then fitted to the following equation.

$$\hat{p}(\theta,t) = F(t)e^{i(\theta+\psi_F(t)-\omega_F t)} + G(t)e^{-i(\theta-\psi_G(t)+\omega_G t)} \tag{3}$$

where the first and the second terms on the right side correspond to the CCW and CW waves, respectively. Here, $F(t), G(t)$ and $\psi_F(t), \psi_G(t)$ are slowly varying amplitudes and phasors of each wave, respectively, and ω_F, ω_G are the oscillatory angular frequencies. It is a common observation that the two waves have slightly different frequencies, i.e., $\omega_F \neq \omega_G$, such as due to low levels of residual mean swirl. Note that the amplitudes and phasors vary much slower than the acoustic frequency, i.e., $\omega_{F,G}\tau_{F,G} \ll 1$. Eq.(3) can then be rewritten in matrix form:

$$\hat{p}(\theta,t) = \begin{bmatrix} e^{i\theta} & e^{-i\theta} \end{bmatrix} \underbrace{\begin{bmatrix} \hat{F} \\ \hat{G} \end{bmatrix}}_{=X} \quad \text{where} \quad \begin{cases} \hat{F}(t) = F(t)e^{i(\psi_F(t)-\omega_F t)} \\ \hat{G}(t) = G(t)e^{-i(-\psi_G(t)+\omega_G t)} \end{cases} \tag{4}$$

Given the measured data, the matrix, X, is evaluated using the method of least squares. This provides the time dependence of the two terms, $\hat{F}$ and $\hat{G}$, in the matrix X. The wave amplitudes and phases are then obtained as $F = |\hat{F}|$ and $\psi_F - \omega_F t = \angle\hat{F}$, respectively. The phase difference between two waves, $\phi = \angle\hat{F} - \angle\hat{G}$, is then given by:

$$\phi(t) = \psi_F(t) - \psi_G(t) - \Delta\omega(t)t \tag{5}$$

where $\Delta\omega = \omega_F - \omega_G$, and $\Delta\omega \ll (\omega_F + \omega_G)/2$.
Once the wave parameters have been extracted, several additional quantities of interest can be calculated. The spin ratio, SR, which quantifies whether the wave is dominated by standing or spinning waves, is defined as:

$$SR(t) = \frac{F(t) - G(t)}{F(t) + G(t)} \tag{6}$$

Here, $SR = 0$ indicates a pure standing wave (SW) and $SR = \pm 1$ means a pure spinning mode in CCW $(+)$ or CW $(-)$ direction. Otherwise, the mode is a combination of standing and spinning modes. Notice that the spin ratio and the phase difference are mathematically independent of each other, as they are determined by different parameters.
The anti-nodal position, θ_a, is defined as the location where the pressure magnitude is maximum. It can be found from the partial derivative of $|\hat{p}(\theta, t)|^2$ with respect to θ to yield:

$$\theta_a(t) = -\frac{1}{2}\left(\psi_F(t) - \psi_G(t) - \Delta\omega(t)t\right) \tag{7}$$

The angular velocity of the anti-nodal line, Ω_a, is a time derivative of θ_a, i.e., $\Omega_a = \frac{d\theta_a}{dt}$. One can relate the anti-nodal position and phase difference as:

$$\phi(t) = -2\theta_a(t) \tag{8}$$

Three important points should be noted. First, the anti-nodal line is mathematically related to phase difference by Eq.(8), but not to spin ratio. Second, the phase difference depends on the anti-nodal position, which is a function of the coordinate system. In other words, the direction of $\theta = 0°$ in reference frame decides the anti-nodal position as well as the phase difference. Lastly, the pressure magnitude at a given sensor location depends on both the wave amplitudes, *F* and *G*, and the location of the anti-nodal line by Eq.(9). This latter dependence is an additional degree of freedom that complicates interpretation of data, which is not present during axial instabilities. This effect of anti-nodal position on the pressure magnitude diminishes as the FG product gets smaller, such as when the mode converges to a spinning mode, i.e., $F = 0$ or $G = 0$.

$$\left|\hat{p}(\theta,t)\right|^2 = F^2 + G^2 + 2FG\cos\left(2\left(\theta - \theta_a\right)\right) \tag{9}$$

Data were taken over a broad range of conditions, with results showing SW and CW modes at different conditions. Figure 5(a) and (b) plot the normalized magnitude of the filtered pressure signals and $(F + G)$ for cases 1 and 2 over 2 seconds, or approximately 3200 cycles of oscillation. The sensor 1 and 3 are omitted as they are similar to the sensor 4 and 2, respectively. The rms value of raw and filtered signal for the sensor 2 drops from 0.074 to 0.051 for case 1 and from 0.086 to 0.029 for case 2. The magnitude is extracted from the Hilbert transform of the oscillatory signal and normalized by its mean pressure. For case 1, dominated by a SW, sensor 2 has magnitude of about 0.075, and slowly oscillates around this value over a time scale of approximately 0.067 s, or 15 Hz. Sensor 4 has much lower magnitude; this variation in magnitude across sensors is expected for a SW mode. In addition, $(F + G)$ is relatively constant around 0.075. In contrast, much more significant oscillation in amplitude is observed in case 2, dominated by a CW mode, and both sensors have comparable maximum and minimum amplitudes. $(F + G)$ is also fluctuating over a larger range of amplitudes.

Figure 5c and d plot the spin ratio for case 1 and 2 over a much longer time interval - 30 seconds, or about 50,000 cycles of oscillation. The spin ratio for the SW mode dominated case 1 oscillates around zero. In contrast, the spin ratio for case 2 dominantly fluctuates around a value of about -0.6, but also intermittently hovers around a value of both zero and 0.6. This indicates

that the dominant mode is the CW, but also shows other attractors that the system is erratically pulled towards, namely a SW and CCW mode.

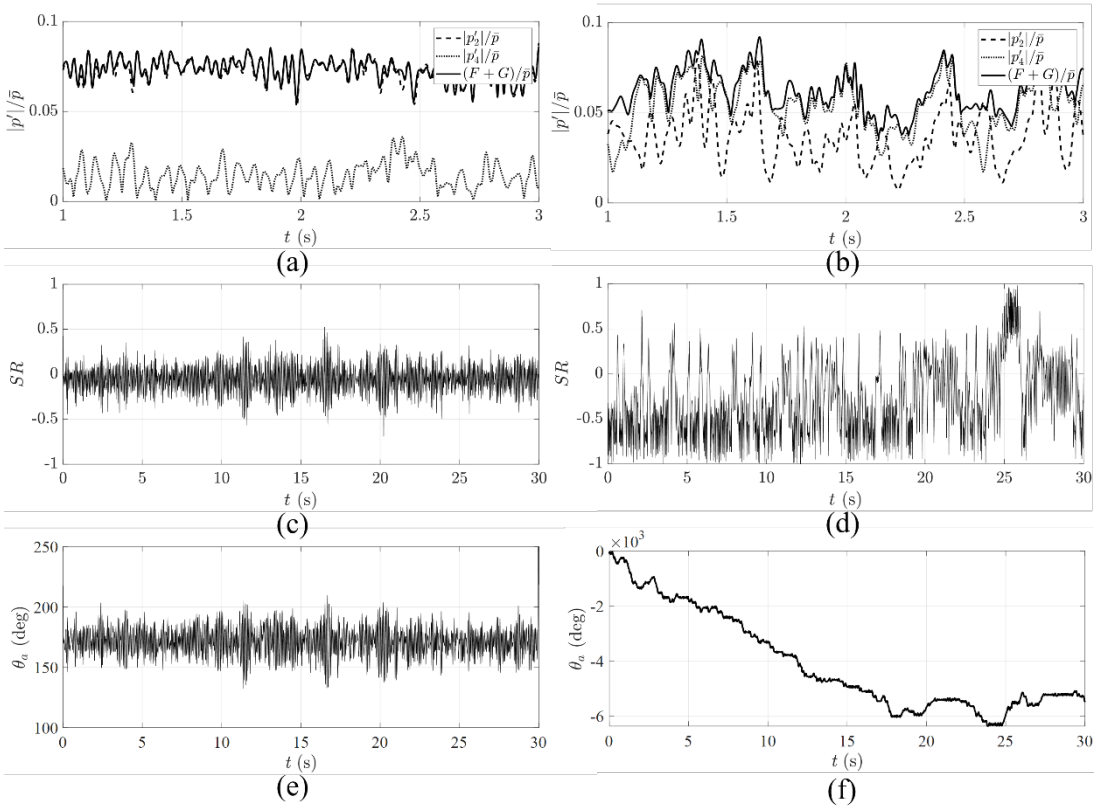

Figure 5 – Magnitude of filtered pressure signals and $(F+G)$ normalized by the combustor pressure (a) case 1 and (b) case 2. Time dependence of spin ratio for (c) case 1 and (d) case 2. Time dependence of anti-nodal position for (e) case 1 and (f) case 2.

Figure 5e and f plot the anti-node position over the same time-interval of 30 seconds. For case 1, the anti-nodal line remains at a remarkably constant location across the entire test, around 170°. This explains why the magnitude of sensor 2 is much larger than that of sensor 4, i.e., sensor 2 is closer to the anti-nodal line than sensor 4. For case 2, the anti-nodal line does not hover around a fixed value but continuously moves, primarily rotating in the CW direction, but sometimes in the other direction as well.

Next, we first investigate the relationship between the spin ratio and the anti-nodal angular velocity. Figure 6 (a) and (b) plot the spin ratio and anti-nodal velocity in time series for these same two cases. For case 1, the spin ratio and anti-nodal velocity are highly correlated with a positive value – when one increases, the other increases, and vice versa. For case 2, however, the correlation is not always positive, but sometimes negative for a very high/low spin ratio. To illustrate this point, Figure 6 (c) and (d) plot the spin ratio histograms conditioned on the anti-nodal velocity, normalized by averaged angular frequency. Figure 6 (c) shows that the spin ratio and the anti-nodal velocity are positively correlated, with a nearly linear relationship when $|SR| < 0.4$. This positive correlation implies that when the spin ratio increases from zero towards a positive value (CCW dominant), then the anti-nodal line rotates in the CCW direction, and vice versa. Recall that SR and Ω_a (or θ_a) are mathematically independent of each other, i.e., this

correlation is not something inherent to the decomposition approach, but rather reflects the fact that the SR and Ω_a are physically coupled to each other.

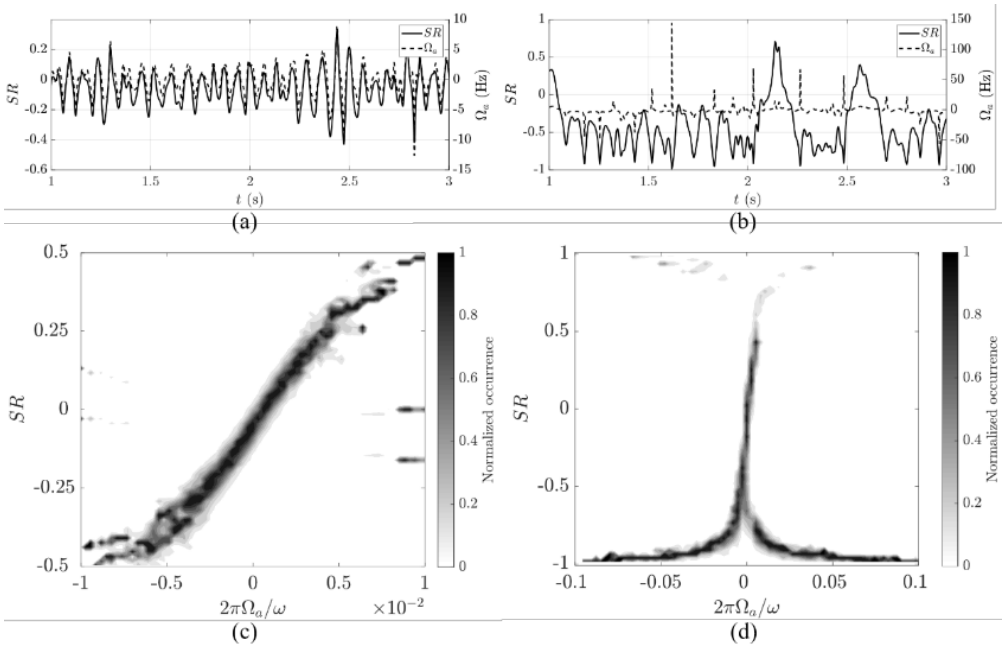

Figure 6 – Time dependence of the spin ratio and anti-nodal velocity for 2 seconds (a) case 1 and (b) case 2. Conditional histogram of spin ratio with respect to normalized anti-nodal velocity for 30 seconds (c) case 1 and (d) case 2. The number of occurrences is normalized by its maximum occurrence in each bin of the normalized velocity.

Turning to case 2 (Figure 6(d)), this positively linear correlation is also observed in a limited region; when $|SR| < 0.4$, but does not occur for $|SR| > 0.4$. Rather, the anti-nodal velocity exhibits a completely different character for SR values close to -1. Similar behavior appears to occur for $SR \sim 1$ cases, but the system spends far less time in this region and so it is not entirely clear.

Previously, we have introduced a methodology to extract the amplitudes of CW/CCW waves as well as their phases. This information offers the spin ratio and the phase difference in time series. Given that these quantities consist of a superposition of low dimensional and high dimensional (turbulent) dynamics, it is useful to develop phase-averaging techniques to filter out the contribution of turbulent components and visualize the low dimensional attractor of the linearly unstable system. This attractor is visualized in spin ratio, SR, and phase difference, ϕ, phase space as follows:

1. Divide phase space (SR, ϕ) into $M \times M$ grid.
2. For each grid, evaluate mean value, (SR_i, ϕ_i).
3. From time series data, find every points satisfying $|SR - SR_i| < \epsilon_{SR}$ and $|\phi - \phi_i| < \epsilon_\phi$ simultaneously, denoted by $\big(SR(t_i), \phi(t_i)\big)$.
4. Identify every data points, $\big(SR(t_i + \Delta t), \phi(t_i + \Delta t)\big)$.
5. Compute ensemble average of $\big(SR(t_i + \Delta t), \phi(t_i + \Delta t)\big)$, denoted by $\Big(\overline{SR}(t_i + \Delta t), \bar{\phi}(t_i + \Delta t)\Big)$.

6. Plot vector from $\left(SR(t_i), \phi(t_i)\right)$ to $\left(\overline{SR}(t_i + \Delta t), \bar{\phi}(t_i + \Delta t)\right)$ in phase space.
7. Repeat these steps for each SR and ϕ pair. Results are plotted for all pairs with > 100 realizations.

For the results presented here, we used $M = 15$ and $\Delta t = 10$ cycles. When plotted in this way, limit cycle oscillations appear as fixed points in phase space. Figure 7 plots the phase portrait in the spin ratio and phase difference space for case 1 and 2. Here, the gray scale denotes the joint histogram of the spin ratio and phase difference, providing a measure of the amount of time that the system spends in this region of phase space. The vector field is converted into streamlines and no streamlines are shown in regions where less than 100 realizations occur. Note that the bottom boundary of the portrait is connected to top boundary owing to the periodicity of the phase difference value. It should be emphasized that the specific phase difference value does not have a physical meaning because it is determined by the coordinate system.

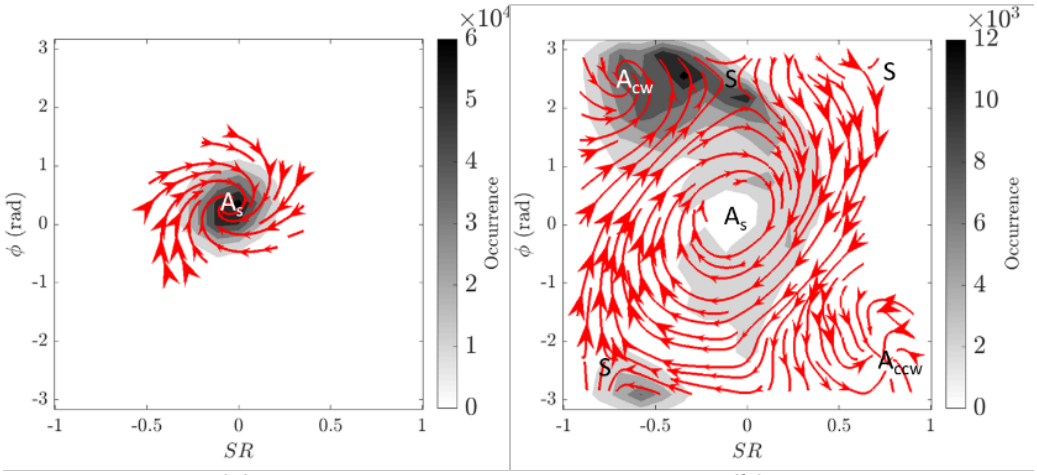

Figure 7 – Phase portrait in spin ratio and phase difference space (a) case 1 (b) case 2. Phase space velocity is indicated by size of vector arrow.

The density distribution for the case 1 in Figure 7 (a) is circular centering at $(SR, \phi) = (0, 0.2)$. The vector trajectories clearly show that the attractor is a stable node, denoted here as "A_s", as the vectors show a clear CW spiral structure into this point. The phase portrait for case 2 (Figure 7(b)) is significantly more complex with three different regions and fixed points. First, it indicates two fixed points, one at $(-0.7, 2.5)$, denoted "A_{CW}", and the other at $(0.75, -2.2)$, denoted "A_{CCW}". Multiple saddle points are also observed, denoted as "S". The higher number of realizations observed near A_{CW} than A_{CCW} implies that A_{CW} is much stronger than A_{CCW}. In other words, the state can be easily expelled from A_{CCW} by the external perturbations and converge to A_{CW}. In addition, it seems that a node similar to that in Figure 7(a) is at the center, but it is difficult to assure whether the node is a stable attractor because of the low realizations. To sum up the structure of the phase portrait, three fixed points exist, i.e., A_s, A_{CW}, and A_{CCW}, and the strength of each attractor depends on test conditions. For case 1, A_s is so strong that the system does not switch to other modes but remains as the standing wave (SW). For case 2, A_{CW} is the most dominant attractor, but the random noise stochastically perturbs the system to switch its mode to the SW or CCW. However, A_S and A_{CCW} must be much weaker attractors than A_{CW}, as the system can easily deviate from A_S or A_{CCW} by noise and converge to A_{CW}. The overall picture that emerges from

this data is that the system has three distinct fixed points, defined by SW, CW, and CCW spinning waves. The strength and/or basin of attraction of these fixed points varies significantly with operating conditions and inherent noise in the system causes the system to visit all three regions of the phase space, given a sufficiently long observation period.

Next, we investigate how azimuthal fuel staging affects the modal dynamics of the transverse instability. To examine the fuel staging effects, we used two separate fuel lines for the outer nozzle, enabling to flow different fuel flow rate through each line. In addition, we changed the fuel configuration to explore the non-uniform flame/temperature effect. The uniform flame/temperature case will be considered as a baseline. In this study, we swept the total mass flow rate of air and fuel, maintaining other parameters, such as preheat temperature and global equivalence ratio, constants. The sweep was carried out with uniform $\mathrm{OR} = 0.5$) and non-uniform azimuthal fuel staging $\mathrm{OR} < 0.5$). We will first examine the uniform fuel staging cases at three different mass flow rates and then briefly explore the non-uniform staging cases, which are summarized in Table 2.

Table 2 – Operating conditions for fuel staging cases

Case	Fuel config.	Preheat temp. (K)	Equiv. ratio (-)	PR (-)	OR (-)	Air mass flow (kg/s)
1	1	600	0.55	0.1	0.5	1.2
2						1.4
3						1.54
4	2				0.45	1.14
5						1.53

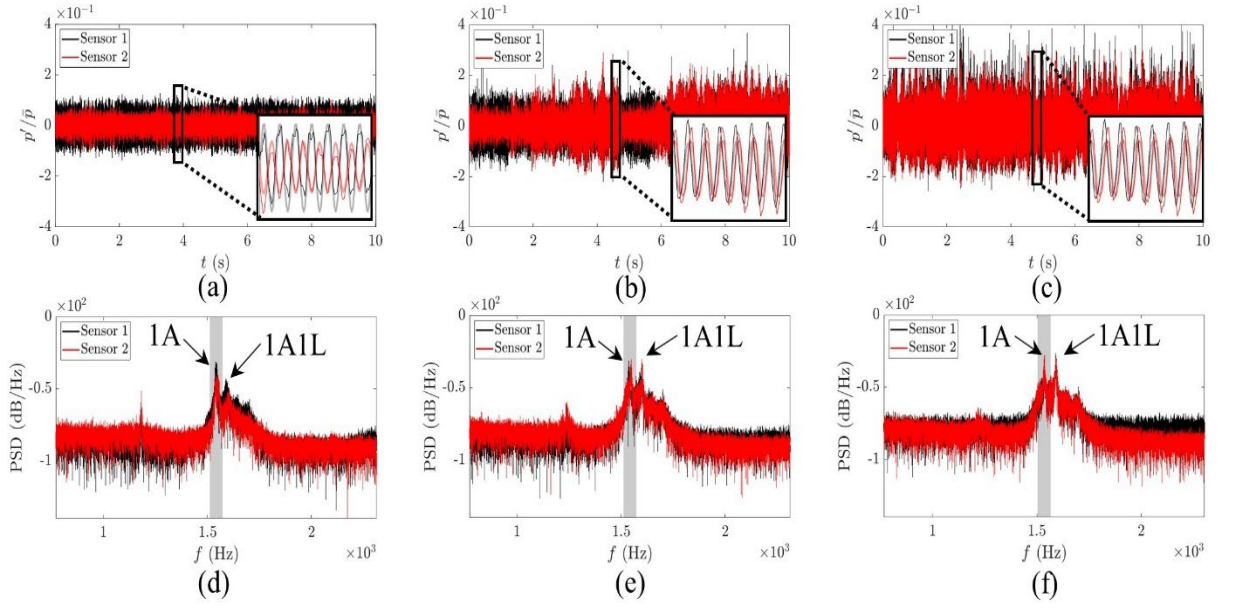

Figure 8 – Raw pressure signals from sensor 1 and 2 for (a) case 1, (b) 2, and (c) 3. The signals are normalized by static pressure. In subfigures (a) – (c), thick and thin lines denote the band-pass filtered and raw signals, respectively. PSD from sensor 1 and 2 for (d) case 1, (e) 2, and (f) 3.

First, consider the dynamics of uniform fuel staging case. Figure 8 (a) – (c) shows the raw and filtered pressure signals for 10 seconds measured from two sensors, S1 and S2, for case 1 - 3. S3 and S4 are omitted here as they are similar to S1 and S2, respectively. The signals are normalized by its static pressure. The power spectrum density (PSD) of the raw signals described in Figure 8 (d) – (f) shows two distinct peaks. The mode shape analysis demonstrated that the first and second peaks correspond to the first pure azimuthal (1A) and the first azimuthal/longitudinal (1A1L) modes, respectively. In this study, we focus on 1A mode only, i.e., the signal is filtered around the first peak with a bandwidth shown as shaded region. For case 1, the signal amplitudes are relatively small and steady. The amplitudes of raw and filtered signals from S1 are greater than those from S2. For case 2, the overall amplitudes increase, and they are not steady, but rather show intermittency. For example, the amplitude of S1 is similar to that of S2 most of the time, but sometimes S1 is greater than S2 such as between 5 and 6 seconds. For case 3, the overall amplitudes further increase compared to cases 1 and 2. The amplitudes of S1 and S2 are fluctuating, but they are similar to each other most of the time.

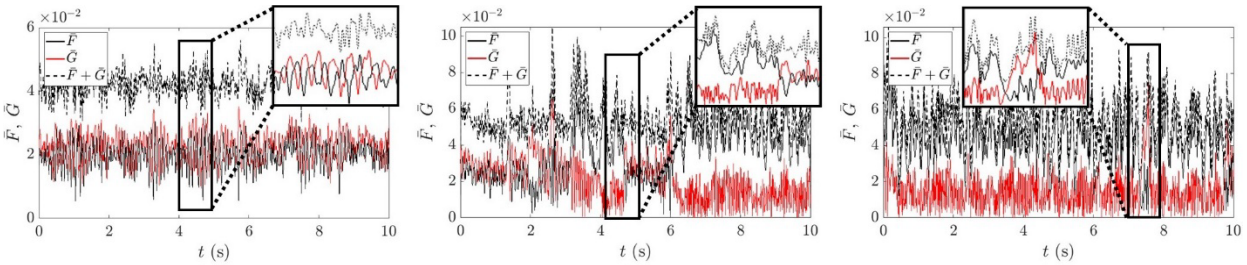

(a) (b) (c)

Figure 9 – Magnitudes of CW, CCW waves, and anti-node in time series for (a) case 1, (b) 2, and (c) 3. They are all normalized by static pressure, i.e., $\bar{F} = F/\bar{p}$, $\bar{G} = G/\bar{p}$.

The amplitudes of CW and CCW waves were extracted from the filtered signals and plotted in Figure 9. The amplitude of the pressure anti-node is also shown here for the comparison. For case 1, F and G are fluctuating around a constant value of 0.02, which will be close to a standing wave, but they are oscillating out of phase to each other. In addition, the oscillations are close to sinusoidal with frequency much lower than the acoustic frequency. This will induce the oscillation in spin ratio around zero. The anti-node amplitude is also fluctuating, but it is not sinusoidal, but rather irregular, which seems to be driven by a noise contribution. These trends of F and G completely change for case 2. Specifically, F and G are not oscillating around a similar value all the time, but they intermittently switch their dominance. From 0 to 2 seconds, for example, F and G have a similar amplitude of oscillation, but from 6 to 10 seconds, F dominates over G. Note that despite this transition, the anti-node amplitude, or the sum of two amplitudes, does not dramatically change, which is well illustrated in the zoom in figure. These trends are similar to case 3 except that now F dominates over G in most of the time, i.e., the transition to a standing wave occurs only once for 10 seconds.

Figure 10 describes SR, φ_{FG}, their probability density function (PDF), and the frequency spectrum for each case. Starting from case 1, the spin ratio is oscillating around zero as expected, but the phase difference is also oscillating in sinusoidal manner. Since the phase difference is directly related to the anti-node, oscillation in phase difference is equivalent to the oscillation in anti-nodal line. Also note that the oscillations of spin ratio and phase difference are not synchronized, but the oscillation in phase difference leads that in spin ratio by about 90 deg, e.g.,

from 5 to 6 seconds in Figure 10 (a). This phase lag will result in a circular orbit in averaged phase portrait, discussed later. The PDF of spin ratio and phase difference shows unimodal distribution. The peak of the spin ratio PDF is around zero, indicating that the instability mode is close to standing wave. The peak of the phase difference PDF is around 0.4 or 72 degrees, indicating that the anti-node is located at around -36 degree since $\theta_a = -\varphi_{FG}/2$. The spectrum in spin ratio and phase difference shows a strong peak at around 10 Hz, implying a coherent oscillation.

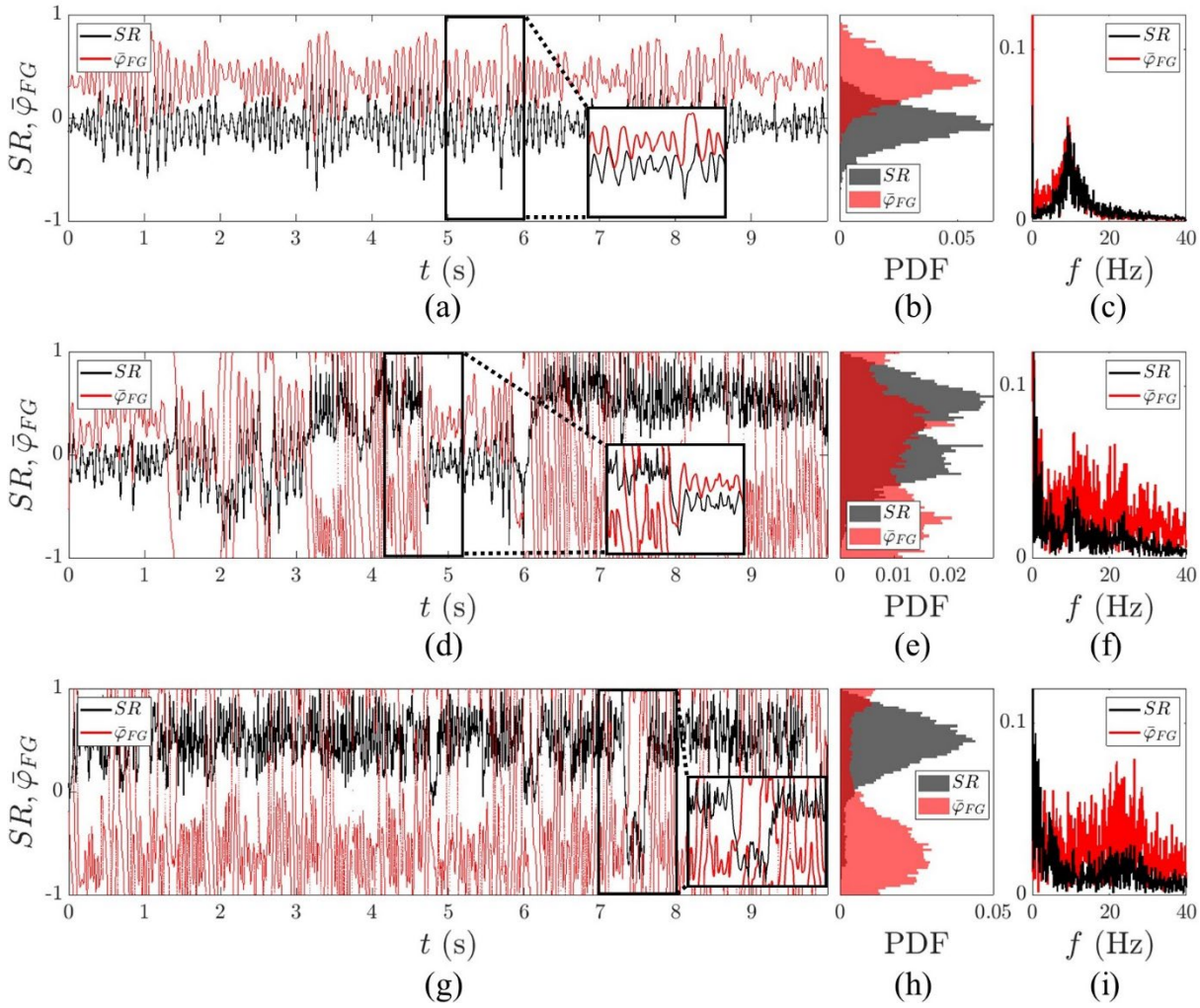

Figure 10 – SR and φ_{FG} in time series for (a) case 1, (d) 2, and (g) 3. The phase difference is normalized by π, i.e., $\bar{\varphi}_{FG} = \varphi_{FG}/\pi$. PDF of SR and φ_{FG} for (b) case 1, (e) 2, and (h) 3. Frequency spectrum of SR and φ_{FG} for (c) case 1, (f) 2, and (i) 3.

For case 2, the spin ratio and phase difference intermittently switch between two points. Specifically, the spin ratio hops between zero and a positive value, whereas the non-dimensional phase difference hops between 0.4 and -0.6. In addition, their transitions occur at the same time, i.e., when the spin ratio switches from zero to a positive value, the phase difference shifts from 0.4 to -0.6, and vice versa. Besides, when the phase difference lingers around -0.6, it sometimes drifts to one/the other directions equivalent to the rotation of anti-nodal line. The PDF of spin ratio exhibits a bimodal distribution, implying a bistable regime in the system. Lastly, unlike case 1, the spectrum shows no dominant peak. Turing to case 3, the spin ratio and phase difference mostly

linger around zero and -0.6, respectively. The PDF shows a unimodal distribution for both spin ratio and phase difference, indicating that the system has one stable equilibrium point. The spectrum does not have a strong peak similar to case 2.

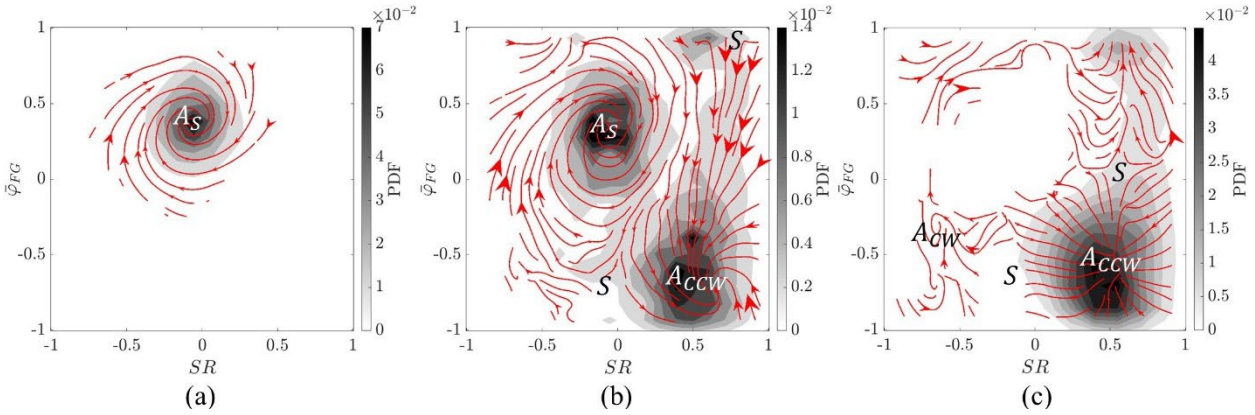

Figure 11 – Averaged phase portrait in spin ratio and phase difference space for (a) case 1, (b) 2, and (d) 3. The phase difference is normalized by π. The gray scale denotes the joint pdf of spin ratio and phase difference. The red arrows and their head size indicate the trajectories and velocity magnitude.

Figure 11 represents the averaged phase portrait for each case. Here, the gray scale denotes the joint PDF in spin ratio and phase difference, the red arrows indicate the trajectories obtained from the phase averaged technique, and the arrow size denotes the velocity of the trajectories. Note that the bottom boundary of the portrait is connected to top boundary owing to the periodicity of the phase difference value. For case 1, the phase portrait shows the trajectories converging to the center, $(SR, \bar{\varphi}_{FG}) = (0, 0.4)$, and the joint PDF shows a unimodal distribution. This indicates that the system has one stable attractor at the center, denoted by A_S where the subscript 'S' means a standing wave. Although the turbulent noise may perturb the system, the attractor is so strong that the system is not able to escapes from it. In addition, the trajectories are spiraling in CW direction, which is expected from the phase lag between the spin ratio and the phase difference in time series described earlier. For case 2, the structure of the phase portrait becomes much complex. First, the CW spiral trajectories at $(0,0.4)$ observed from case 1 still exist, but the intensity of the attractor is weaker than case 1, manifested by lower value of the joint PDF. Instead, the system shows another stable attractor at $(SR, \bar{\varphi}_{FG}) = (0.5, -0.75)$, denoted by$A_{CCW}$, which corresponds to the dominant CCW spinning wave. This preference in CCW direction may be a result of azimuthal convective phenomena, i.e., the outer nozzles are swirling in CCW direction. Two saddle points, denoted by 'S', were also observed near the top and bottom boundaries. To sum up the overall structure, the system can stabilize at two stable attractors, standing and CCW spinning modes, and the turbulent noise seems to perturb the system allowing to hop between these two attractors. For case 3, A_{CCW} still exists at the bottom right corner, but A_S is not visible. Rather, a CW wave attractor, A_{CW}, appears at the bottom left corner although the joint PDF around it is sparse. This implies that A_{CW} may be a stable attractor, but its strength is so weak that the system can be readily expelled from the attractor by the external noise, and it converges to A_{CCW}. The system then stays around this attractor most of the time. In conclusion, Figure 11 suggests that the system contains multiple attractors, standing and spinning waves. The strength of each attractor depends on the operating conditions. As the mass flow rate increases, the dominant attractor transitions from

standing to spinning waves, but the external noise perturbs the system to travel around these attractors.

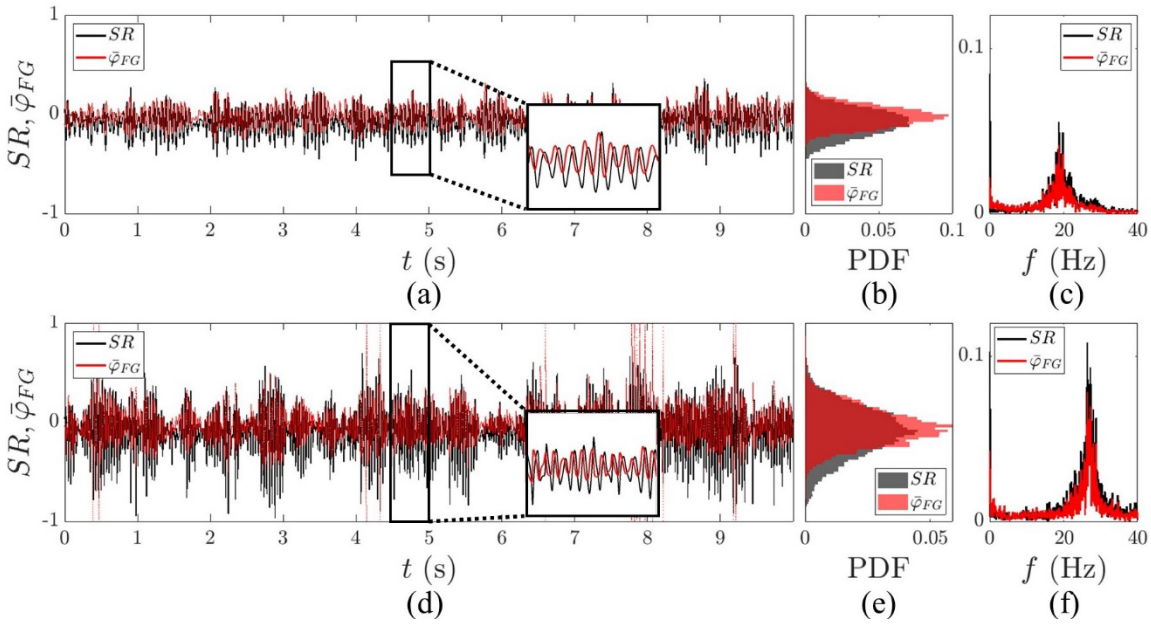

Figure 12 – SR and $\bar{\varphi}_{FG}$ in time series for (a) case 4 and (d) 5. PDF of SR and $\bar{\varphi}_{FG}$ for (b) case 4 and (e) 5. FFT of SR and $\bar{\varphi}_{FG}$ for (c) case 4 and (f) 5.

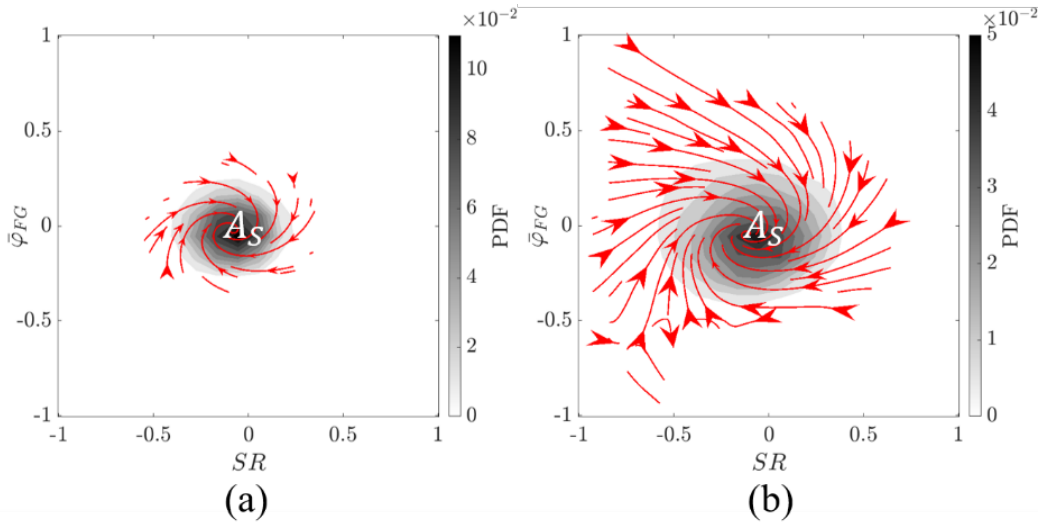

Figure 13 – Averaged phase portrait in $(SR, \bar{\varphi}_{FG})$ space for (a) case 4 and (b) 5.

Next, we focus on the dynamics due to non-uniform fuel staging. Here, we present only SR and $\bar{\varphi}_{FG}$ as well as their phase portraits for brevity. Figure 12 shows SR and $\bar{\varphi}_{\mathrm{FG}}$ in time series, their PDFs, and the FFT for case 4 (low flow rate) and 5 (high flow rate). From these plots, we can make the following observations. First, for non-uniform staging cases, the instability mode always exists as a standing wave no matter what the flow rate is. Second, the oscillation amplitudes in SR and $\bar{\varphi}_{\mathrm{FG}}$ increases with increasing mass flow rate, which can be seen from the variance of the PDF as well as the peak amplitude in the FFT. Third, the oscillation frequency also increases with the

mass flow rate shown in the FFT. This increase in frequency was not shown earlier as the mode switches to a spinning wave for a high flow rate. Lastly, when comparing cases 1 and 4 where their flow rates are close to each other, the oscillation amplitudes are similar, but the frequency for case 4 is much higher. This demonstrates that the azimuthal non-uniformity increases the oscillation frequency of SR and $\overline{\varphi}_{\mathrm{FG}}$.

Figure 13 represents the phase portraits for cases 4 and 5. Note that the stable attractors are fixed at $(\mathrm{SR}, \overline{\varphi}_{\mathrm{FG}}) = (0, 0)$ for both cases, indicating that the anti-node is located at 0°. This is probably because the hotter flames, which strongly interact with the acoustics, are distributed in a horizontal direction, locking the anti-nodal line at 0°. Similar reasoning can be used to explain the standing wave for high flow rate, i.e., since the anti-nodal line is fixed at 0° by flame non-uniformity, it requires a much higher flow rate to break the standing wave, which is not observed in this data. Regarding the differences between the two cases, the distribution of joint PDF is much wider for case 5, suggesting that the amplitude of the oscillation gets larger with increasing flow rate. In addition, the trajectories are faster for case 5 than case 4. This shows that the system oscillates faster with a higher flow rate, which is consistent with the high frequency in Figure 12(f).

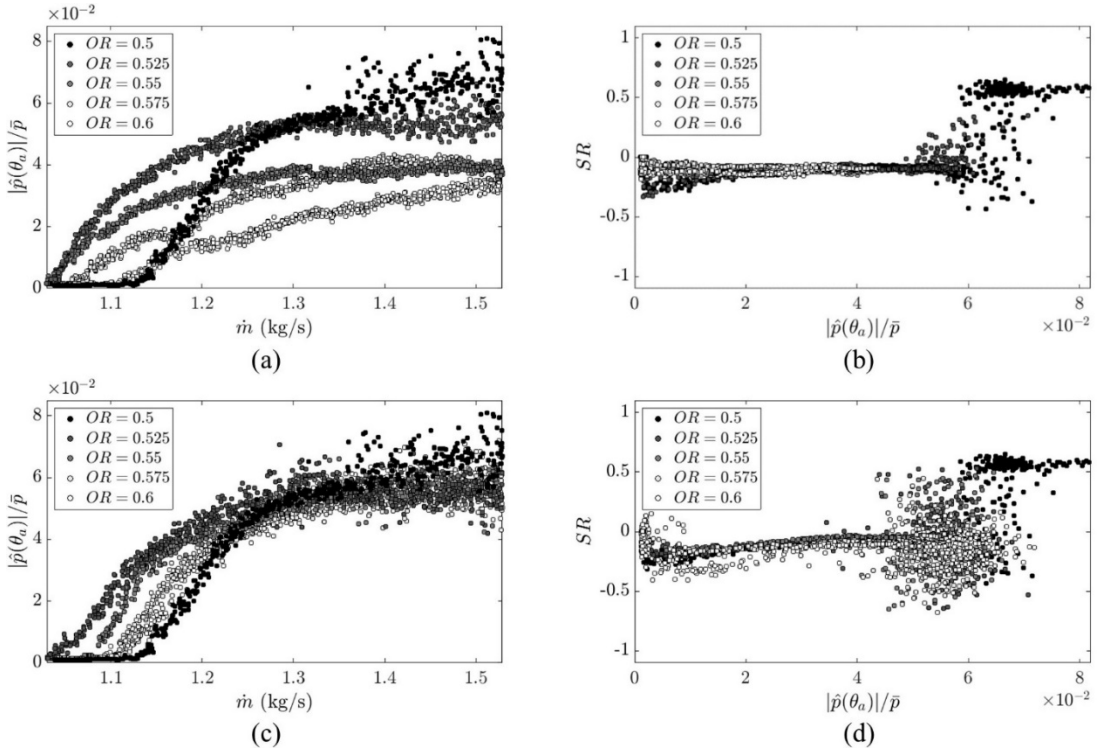

Figure 14 – Normalized anti-node magnitude as a function of mass flow rate at different OR values with fuel configuration (a) 2 and (c) 3. SR as a function of normalized anti-node magnitude at different OR values with fuel configuration (b) 2 and (d) 3. the values of magnitude and SR were obtained by averaging their time series during steady state.

Finally, consider the comparison between the uniform and non-uniform staging cases. For the azimuthal mode, pressure magnitude measured at a fixed position is generally not an appropriate indicator of the instability amplitude because the pressure magnitude is a function of F, G and $\overline{\varphi}_{\mathrm{FG}}$, which can vary with slow time scale. For a standing wave, for example, the rotation/oscillation of the anti-nodal line affects the magnitude measured at a fixed location. In addition, a transition from

standing to spinning wave changes the magnitude. Therefore, we used the pressure magnitude at the anti-node as an indicator because it provides a relatively steady value under anti-node oscillation or mode switching. Figure 14(a) and (b) summarize the effects of fuel staging configuration 2 on the modal dynamics of the instability. Figure 14(a) represents the anti-node magnitude as a function of mass flow rate with different ORs. Here, cases with different ORs are added to explore the fuel staging effect in detail. It is observed that as the mass flow rate increases, the magnitude monotonically increases for all ORs, but it is maximized with uniform fuel staging ($\mathrm{OR} = 0.5$). When the OR is 0.6, the magnitude is minimum. It is speculated that the instability may disappear with a much higher OR. It is also interesting to note that the onset of the instability, referred to as the Hopf bifurcation point, depends on fuel staging. Specifically, the mass flow rate required to trigger the instability decreases with the OR from 0.5 to 0.55, but it increases with the OR from 0.55 to 0.6. This suggests that sufficient non-uniform fuel staging is also beneficial to reduce the instability conditions. Figure 14(b) shows SR as a function of anti-node magnitude with different ORs. For a uniform staging case, the instability starts from a standing wave at low magnitudes. At intermediate magnitudes, the mode switches between standing and spinning waves. At high magnitudes, the mode is stabilized at a spinning wave. When the OR is set to 0.525, the standing and bistable regimes are observed, but not the spinning wave. Below the OR of 0.525, only the standing wave appears. To summarize the observations, the instability starts as a standing wave, and as the magnitude grows, it passes a bistable regime, where, standing and spinning waves both exist, and finally reaches a stable spinning wave above a certain threshold. Figure 14(c) and (d) show the same plots with Figure 14(a) and (b) but with fuel configuration 3. Figure 14(c) demonstrates that the onset of the instability follows similar trends with those for fuel configuration 2, i.e., Hopf bifurcation point advances and delays as the OR increases. As the flow rate increases, however, the pressure magnitudes collapse to each other, implying that the fuel configuration 3 has little effect of mitigating/suppressing the instability. In addition, Figure 14(d) shows that the instability mode exhibits not only a standing wave at low magnitudes but also a switching mode at large magnitude regardless of OR. This suggests that fuel configuration 3 has a negligible impact on modal dynamics.

Having studied the modal dynamics due to fuel staging from the experimental experiments, we next turn to an analysis framework for modeling these dynamics. The stochastic, nonlinear wave equation, presented below, closely follows prior studies:

$$\frac{\partial^2 p}{\partial t^2} - \frac{c^2}{R^2}\frac{\partial^2 p}{\partial \theta^2} = h_1\left(p, \frac{\partial p}{\partial t}\right) + \xi_1(t) + h_2\left(p, \frac{\partial p}{\partial t}\right)\xi_2(t) \tag{10}$$

Here, p is the acoustic pressure, c the sound speed, R the chamber radius, ξ_1 an additive background noise term, ξ_2 a parametric noise term, and $h_{1,2}$ represents all other source/sink and wave propagation terms due to unsteady heat release, temperature non-uniformity, bulk flow effects, and nonlinearities. Notice that the wave equation has been spatially integrated in the axial and radial directions, and that mean flow, density gradient, and losses at boundaries are encapsulated in these general functions, $h_{1,2}(p, dp/dt)$. Note that the solutions of the homogeneous wave equation, given by:

$$p(\theta, t) = \sum_{m=1}^{\infty}\left[\eta_{1,m}(t)\cos(\mathrm{m}\,\theta) + \eta_{2,m}(t)\sin(\mathrm{m}\,\theta)\right] \tag{11}$$

constitute a complete, orthogonal set of basis functions. As such, the essence of the Galerkin method is to use these basis functions for writing the solution of the more general, nonlinear Eq.(10). There is no approximation when the infinite summation is retained, but truncation

necessarily introduces approximations. We truncate this summation as a single mode that nonlinearly interacts with itself – the heat release nonlinearities, which generally dominate nonlinear effects in lean premixed systems, lead to strong self-interactions of a mode with itself. Thus, we shall approximate the acoustic pressure associated with a given n^{th} eigenmode as:

$$p(\theta,\mathrm{t}) \approx \eta_1(t)\cos(\mathrm{n}\,\theta) + \eta_2(t)\sin(\mathrm{n}\,\theta) \tag{12}$$

where η_1 and η_2 are the amplitudes of two orthogonal standing modes of azimuthal wavenumber, n. The subscript, n, in η has been omitted here. Next, we can treat the function $h_1(p, dp/dt)$ in Eq.(10) quite generally by expanding it as a Taylor series:

$$\begin{aligned} h_1\left(p,\frac{dp}{dt}\right) = {} & B_{00}(\theta) + B_{10}(\theta)p + B_{01}(\theta)\dot{p} + B_{20}(\theta)p^2 + B_{11}(\theta)p\dot{p} + B_{02}(\theta)\dot{p}^2 \\ & + B_{30}(\theta)p^3 + B_{21}(\theta)p^2\dot{p} + B_{12}(\theta)p\dot{p}^2 + B_{03}(\theta)\dot{p}^3 + B_{40}(\theta)p^4 \\ & + B_{31}(\theta)p^3\dot{p} + B_{22}(\theta)p^2\dot{p}^2 + B_{13}(\theta)p\dot{p}^3 + B_{04}(\theta)\dot{p}^4 \end{aligned} \tag{13}$$

where $\dot{p}$ is the time derivative of p, and B_{ij}'s are coefficients of $p^i\dot{p}^j$. $h_1(p, dp/dt)$ is truncated at fourth order. The coefficients B_{ij} are non-time varying but can vary azimuthally; physically this would occur because of discrete nozzle locations, azimuthally non-uniform temperature distribution, azimuthally non-uniform thermo-acoustic coupling strength, etc. In order to account for this in a general fashion, we write them as the following series:

$$\begin{aligned} B_{01}(\theta) &= -\alpha + \underbrace{\beta\left(1 + \sum_{m=1}^{\infty} C_{m,01}\cos(m\theta) + \sum_{m=1}^{\infty} S_{m,01}\sin(m\theta)\right)}_{=\beta_0(\theta)} \\ B_{ij}(\theta) &= b_{ij}\left(1 + \sum_{m=1}^{\infty} C_{m,ij}\cos(m\theta) + \sum_{m=1}^{\infty} S_{m,ij}\sin(m\theta)\right) \quad for\ i \neq 0, j \neq 1 \end{aligned} \tag{14}$$

Although not necessary, it is convenient to decompose the linear growth/damping term, B_{01}, into a linear damping term, α, which is not dependent on θ, and the linear growth term, $\beta_0(\theta)$, which is a function of θ. We next follow the standard steps in the Galerkin expansion approach and integrate these equations from 0 to 2π with respect to θ, producing two sets of second order differential equations,

$$\begin{aligned} \ddot{\eta}_1 + \left[\alpha - \beta\left(1 + \frac{C_{2n,01}}{2}\right)\right]\dot{\eta}_1 + \omega_1^2\eta_1 &= f_1(\eta_1,\eta_2,\dot{\eta}_1,\dot{\eta}_2) \\ \ddot{\eta}_2 + \left[\alpha - \beta\left(1 - \frac{C_{2n,01}}{2}\right)\right]\dot{\eta}_2 + \omega_2^2\eta_2 &= f_2(\eta_1,\eta_2,\dot{\eta}_1,\dot{\eta}_2) \end{aligned} \tag{15}$$

Here,

$$\begin{aligned} f_1(\eta_1,\eta_2,\dot{\eta}_1,\dot{\eta}_2) = {} & \frac{\beta}{2}S_{2n,01}\dot{\eta}_2 + \frac{b_{10}}{2}S_{2n,10}\eta_2 \\ & + \frac{b_{30}}{8}\begin{bmatrix} (6 + 4C_{2n,30} + C_{4n,30})\eta_1^3 + 3(2 - C_{4n,30})\eta_1\eta_2^2 \\ +3(2S_{2n,30} + S_{4n,30})\eta_1^2\eta_2 + (2S_{2n,30} - S_{4n,30})\eta_2^3 \end{bmatrix} \\ & + \frac{b_{21}}{8}\begin{bmatrix} (6 + 4C_{2n,21} + C_{4n,21})\eta_1^2\dot{\eta}_1 + (2 - C_{4n,21})(\eta_2^2\dot{\eta}_1 + 2\eta_1\eta_2\dot{\eta}_2) \\ +(2S_{2n,21} - S_{4n,21})\eta_2^2\dot{\eta}_2 + (2S_{2n,21} + S_{4n,21})(\eta_1^2\dot{\eta}_2 + 2\eta_1\eta_2\dot{\eta}_1) \end{bmatrix} \\ & + \frac{b_{12}}{8}\begin{bmatrix} (6 + 4C_{2n,12} + C_{4n,12})\eta_1\dot{\eta}_1^2 + (2 - C_{4n,12})(\eta_1\dot{\eta}_2^2 + 2\eta_2\dot{\eta}_1\dot{\eta}_2) \\ +(2S_{2n,12} - S_{4n,12})\eta_2\dot{\eta}_2^2 + (2S_{2n,12} + S_{4n,12})(\eta_2\dot{\eta}_1^2 + 2\eta_1\dot{\eta}_1\dot{\eta}_2) \end{bmatrix} \\ & + \frac{b_{03}}{8}\begin{bmatrix} (6 + 4C_{2n,03} + C_{4n,03})\dot{\eta}_1^3 + 3(2 - C_{4n,03})\dot{\eta}_1\dot{\eta}_2^2 \\ +3(2S_{2n,03} + S_{4n,03})\dot{\eta}_1^2\dot{\eta}_2 + (2S_{2n,03} - S_{4n,03})\dot{\eta}_2^3 \end{bmatrix} \end{aligned} \tag{16}$$

$$+\zeta + \int_0^{2\pi} h_2(\eta_1, \eta_2, \dot{\eta}_1, \dot{\eta}_2)\sin(n\theta)\,\xi_2\,d\theta$$

$$f_2(\eta_1, \eta_2, \dot{\eta}_1, \dot{\eta}_2) = \frac{\beta}{2}S_{2n,01}\dot{\eta}_1 + \frac{b_{10}}{2}S_{2n,10}\eta_1$$
$$+\frac{b_{30}}{8}\begin{bmatrix}(6-4C_{2n,30}+C_{4n,30})\eta_2^3 + 3(2-C_{4n,30})\eta_1^2\eta_2 \\ +(2S_{2n,30}+S_{4n,30})\eta_1^3 + 3(2S_{2n,30}-S_{4n,30})\eta_1\eta_2^2\end{bmatrix}$$
$$+\frac{b_{21}}{8}\begin{bmatrix}(6-4C_{2n,21}+C_{4n,21})\eta_2^2\dot{\eta}_2 + (2-C_{4n,21})(\eta_1^2\dot{\eta}_2 + 2\eta_1\eta_2\dot{\eta}_1) \\ +(2S_{2n,21}+S_{4n,21})\eta_1^2\dot{\eta}_1 + (2S_{2n,21}-S_{4n,21})(\eta_2^2\dot{\eta}_1 + 2\eta_1\eta_2\dot{\eta}_2)\end{bmatrix}$$
$$+\frac{b_{12}}{8}\begin{bmatrix}(6-4C_{2n,12}+C_{4n,12})\eta_2\dot{\eta}_2^2 + (2-C_{4n,12})(\eta_2\dot{\eta}_1^2 + 2\eta_1\dot{\eta}_1\dot{\eta}_2) \\ +(2S_{2n,12}+S_{4n,12})\eta_1\dot{\eta}_1^2 + (2S_{2n,12}-S_{4n,12})(\eta_1\dot{\eta}_2^2 + 2\eta_2\dot{\eta}_1\dot{\eta}_2)\end{bmatrix}$$
$$+\frac{b_{03}}{8}\begin{bmatrix}(6-4C_{2n,03}+C_{4n,03})\dot{\eta}_2^3 + 3(2-C_{4n,03})\dot{\eta}_1^2\dot{\eta}_2 \\ +(2S_{2n,03}+S_{4n,03})\dot{\eta}_1^3 + 3(2S_{2n,03}-S_{4n,03})\dot{\eta}_1\dot{\eta}_2^2\end{bmatrix}$$
$$+\zeta + \int_0^{2\pi} h_2(\eta_1, \eta_2, \dot{\eta}_1, \dot{\eta}_2)\cos(n\theta)\,\xi_2\,d\theta$$

And,

$\omega = nc/R,\ \ \omega_1^2 = \omega^2 - b_{10}(1 + C_{2n,10}/2),\qquad \omega_2^2 = \omega^2 - b_{10}(1 - C_{2n,10}/2)$

and $\zeta(t)$ is a spatially averaged additive noise source. These describe the 2nd order harmonic oscillators of two orthogonal standing waves coupled through the source terms. Note that even order nonlinearities (e.g., terms multiplied by b_{20}, b_{11}, and b_{40}, etc) are eliminated during the spatial averaging , i.e., only the odd order terms survive. Similarly, azimuthal non-uniformity terms higher than $4n$ order are averaged out, and only $2n$ and $4n$ terms have an impact on the dynamics. Consider the effects of non-uniformity on two oscillators. From Eq.(15), one can see that the term, $\alpha - \beta(1 \pm C_{2n,01}/2)$, determines the linear stability of each oscillator. Specifically, when $C_{2n,01} = 0$, two oscillators have identical linear growth/damping rate. i.e., they are both linearly stable or unstable. However, when $C_{2n,01} \neq 0$, their linear growth/damping rate would be different. For instance, one oscillator could be linearly unstable while the other is stable. In addition, $C_{2n,10}$ influences the natural frequencies of the two oscillators and, consequently, controls whether the natural frequencies of the two eigenmodes are identical or different. For example, when $C_{2n,10} > 0$ and $b_{10} < 0$, the natural frequency of η_1 is greater than that of η_2.

Given the fact that $\eta(t)$ is oscillating harmonically with a temporally varying amplitude and phase, it is convenient to utilize a Van der Pol decomposition to rewrite the temporal dynamics, $\eta(t)$.

$$\eta_1(t) = A(\tau)\cos(\omega_1(\tau)t + \phi_A(\tau)) = A(\tau)\cos(\bar{\omega}t + \varphi_A(\tau))$$
$$\eta_2(t) = B(t)\cos(\omega_2(\tau)t + \phi_B(\tau)) = B(t)\cos(\bar{\omega}t + \varphi_B(\tau)) \qquad (17)$$

where

$$\bar{\omega} = \frac{\omega_1(\tau) + \omega_2(\tau)}{2},\quad \Delta\omega = \omega_2(\tau) - \omega_1(\tau),$$
$$\varphi_A(\tau) = \phi_A(\tau) - \frac{\Delta\omega t}{2},\quad \varphi_B(\tau) = \phi_B(\tau) + \frac{\Delta\omega t}{2} \qquad (18)$$

We assume that the characteristic time scales over which the amplitude and phase ($A,\ B$ and φ, respectively) vary are much slower than the acoustic time scale, i.e., $\tau \gg 1/\bar{\omega}$. Assuming ζ is

Gaussian white noise, one can perform deterministic and stochastic averaging to produce first order differential equations for the slowly varying amplitudes and phase (not shown here for space). These equations exhibit a very broad range of behaviors, and the formulation has 2 independent linear and 24 independent nonlinear coefficients. Notice that in reality, some of these parameters may be interconnected to each other, preventing us from isolating them separately in experiments. The model problems considered allow us to isolate each parameter, and thus, help us understand their individual effects. This section works from simple cases that are amenable to analytical results and insights to more involved problem that captures the observed dynamics. Specifically, we consider the model equations below. First, without loss of generality, we define the azimuthal origin such that $S_{2,01} = 0$. Second, we consider a subset of the larger independent parameter space by (1) setting $C_{4,ij} = S_{4,ij} = 0$; this is equivalent to assuming that $4n$ non-uniformity is negligible relative to $2n$, and (2) setting the nonlinear coefficients, b_{30}, b_{12}, and b_{03} to zero. In the zero frequency spacing case that is analytically considered in the next section, these assumptions eliminate the coupling between amplitude and phase dynamics, enabling us to solve for all FP's and their stability. It will be shown later that the simulation with these assumptions still can capture the experimental observations quite well. The governing equations then simplify to:

$$\begin{aligned}
\dot{A} &= \frac{1}{4}\left[\beta\left(2 + C_{2,01}\right) - 2\alpha\right]A - k_{A1}\sin\varphi\, B + k_{A2}A^3 + (k_3 + k_{A3}\cos 2\varphi)AB^2 \\
&\quad + \frac{\Gamma}{4\bar{\omega}^3 A} + \frac{\zeta_A}{\bar{\omega}} \\
\dot{B} &= \frac{1}{4}\left[\beta\left(2 - C_{2,01}\right) - 2\alpha\right]B - k_{B1}\sin\varphi\, A + k_{B2}B^3 + (k_3 + k_{B3}\cos 2\varphi)BA^2 \\
&\quad + \frac{\Gamma}{4\bar{\omega}^3 B} + \frac{\zeta_B}{\bar{\omega}} \\
\dot{\varphi} &= \Delta - \frac{\tilde{b}_{10}S_{2,10}}{2}\left(\frac{A/B}{\Delta + 2} + \frac{B/A}{\Delta - 2}\right)\cos\varphi + \left(k_{\varphi A}A^2 + k_{\varphi B}B^2\right)\sin 2\varphi \\
&\quad + \left(\frac{1}{A} + \frac{1}{B}\right)\frac{\zeta_\varphi}{\bar{\omega}}
\end{aligned} \tag{19}$$

where

$$k_{A1} = \frac{b_{10}S_{2,10}}{2(\Delta - 2)}, k_{B1} = \frac{b_{10}S_{2,10}}{2(\Delta + 2)}, k_{A2} = \frac{b_{21}}{32}\left(3 + 2C_{2,21}\right), k_{B2} = \frac{b_{21}}{32}\left(3 - 2C_{2,21}\right)$$

$$\begin{aligned}
k_3 = \frac{b_{21}}{16}, k_{A3} = -\frac{b_{21}}{32}\left(\frac{3\Delta + 2}{\Delta - 2}\right), k_{B3} = -\frac{b_{21}}{32}\left(\frac{3\Delta - 2}{\Delta + 2}\right), k_{\varphi A} \\
= \frac{b_{21}}{64}\left(\frac{3\Delta - 2}{\Delta + 2}\right), k_{\varphi B} = \frac{b_{21}}{64}\left(\frac{3\Delta + 2}{\Delta - 2}\right)
\end{aligned} \tag{20}$$

The tildes on α, β and b_{ij} have been omitted. Recall that $C_{2,01}, S_{2,10}$ and $C_{2,21}$ are parameters that describe the non-uniformities in the source term response, such as dQ/dt, to $\dot{p}, p$ and $p^2\dot{p}$, respectively. Note that these parameters and Δ cause the coefficients in the $\dot{A}$ and $\dot{B}$ equations to differ; stated differently, if $\Delta = C_{2,01} = S_{2,10} = C_{2,21} = 0$, the equations for $\dot{A}$ and $\dot{B}$ are symmetric.

Consider the deterministic limit cycle solutions (i.e., the fixed points (FP) of A, B, and φ) and their stability with pressure coupled azimuthal non-uniformity parameter, $S_{2,10} = 0$, and no frequency shift, $\Delta = 0$. The effects of nonzero values of these parameters will be numerically

investigated later. For the deterministic FP analysis, the time derivative of each variable as well as the noise terms set to zero, leading to the following equations:

$$\begin{aligned} 0 &= \frac{1}{4}\left[\beta\left(2 + C_{2,01}\right) - 2\alpha\right]A + k_{A1}A^3 + (k_2 + k_{A2}\cos 2\varphi)AB^2 \\ 0 &= \frac{1}{4}\left[\beta\left(2 - C_{2,01}\right) - 2\alpha\right]B + k_{B1}B^3 + (k_2 + k_{B2}\cos 2\varphi)BA^2 \\ 0 &= \left(k_{\varphi A}A^2 + k_{\varphi B}B^2\right)\sin 2\varphi \end{aligned} \tag{21}$$

The FPs are given by:

$$\begin{aligned} &\text{FP\#1:} \quad A^{*2} = B^{*2} = 0 \\ &\text{FP\#2:} \quad A^{*2} = \frac{16\alpha - (16 + 8C_{2,01})\beta}{b_{21}(3 + 2C_{2,21})}, \quad B^{*2} = 0, \\ &\text{FP\#3:} \quad B^{*2} = \frac{16\alpha - (16 - 8C_{2,01})\beta}{b_{21}(3 - 2C_{2,21})}, \quad A^{*2} = 0, \\ &\text{FP\#4:} \quad A^{*2} = \frac{8\alpha\left(1 - C_{2,21}\right) - 4\beta\left(C_{2,01}\left(2 - C_{2,21}\right) + 2\left(1 - C_{2,21}\right)\right)}{b_{21}\left(2 - C_{2,21}^2\right)}, \\ &\qquad\quad B^{*2} = \frac{8\alpha\left(1 + C_{2,21}\right) + 4\beta\left(C_{2,01}\left(2 + C_{2,21}\right) - 2\left(1 + C_{2,21}\right)\right)}{b_{21}\left(2 - C_{2,21}^2\right)}, \\ &\qquad\quad \varphi^* = \pm\frac{\pi}{2}, \pm\frac{3\pi}{2}, \ldots \end{aligned} \tag{22}$$

where * is the value at each FP. Note that there are 4 possible solutions to this equation. Here, FP#1 is a zero amplitude mode, FPs #2 and #3 are purely standing waves orthogonal to each other, and FP#4 is a mixed wave. Although not written here, if FP#4 solution is recast as two counter rotating eigenmodes, it can be shown that the dominance between CW and CCW waves for FP#4 is determined by φ^*, i.e., if $\varphi^* = \frac{\pi}{2}\left(-\frac{\pi}{2}\right)$, CW (CCW) dominates over CCW (CW). When $C_{2,01} = C_{2,21} = 0$, FP#4 becomes a purely spinning wave whose direction is determined by its initial condition. The physical realization of the above FPs depends on the stability of each FP. The stability analysis can be done by perturbing the steady-state solutions:

$$\begin{aligned} \dot{A} &= A^* + A' \quad \text{where} \quad A' \ll A^* \\ \dot{B} &= B^* + B' \quad \text{where} \quad B' \ll B^* \\ \dot{\varphi} &= \varphi^* + \varphi' \quad \text{where} \quad \varphi' \ll \varphi^* \end{aligned} \tag{23}$$

Each FP is stable when:

$$\begin{aligned} &\text{FP\#1: } \gamma \le \gamma_{Hopf,1} \\ &\text{FP\#2, 3: } \gamma_{Hopf,1} < \gamma \le \gamma_{Hopf,2} \\ &\text{FP\#4: } \gamma > \gamma_{Hopf,2} \end{aligned} \tag{24}$$

where

$$\gamma = \beta/\alpha$$

$$\gamma_{Hopf,1} = \begin{cases} \dfrac{2}{2 + C_{2,01}}, & \text{if } 0 \le C_{2,01} < 1 \text{ (FP\#2)} \\ \dfrac{2}{2 - C_{2,01}}, & \text{if } -1 < C_{2,01} < 0 \text{ (FP\#3)} \end{cases} \tag{25}$$

$$\gamma_{Hopf,2} = \begin{cases} \dfrac{2(1+C_{2,21})}{2(1-C_{2,01})+C_{2,21}(2-C_{2,01})}, \text{if } 0 \le C_{2,01} < 1 \text{ and } C_{2,01} < \dfrac{2(C_{2,21}+1)}{2+C_{2,21}} & \text{(FP\#2)} \\ \dfrac{2(1-C_{2,21})}{2(1+C_{2,01})-C_{2,21}(2+C_{2,01})}, \text{if } -1 \le C_{2,01} < 0 \text{ and } C_{2,01} < \dfrac{2(C_{2,21}-1)}{2-C_{2,21}} & \text{(FP\#3} \end{cases}$$

It has been assumed that the non-uniformity parameters, $C_{2,01}$ and $C_{2,21}$, are bounded between ± 1. This physically implies that the non-uniform parameters are less than mean value. Here, $\gamma_{Hopf,1}$ corresponds to the bifurcation from FP#1 (zero amplitude) to FP#2 or #3 (standing wave), and $\gamma_{\text{Hopf,2}}$ is the bifurcation from FP#2 or #3 (standing wave) to FP#4 (mixed wave). Figure 15 summarizes the stability of each FP in $(C_{2,01}, \gamma)$ space with different $C_{2,21}$ values. Here, the horizontal dash line indicates $\gamma = 1$, and the contour lines denote $|SR|$. Consider a case where γ is increasing with fixed values of $C_{2,01}$ and $C_{2,21}$. This is equivalent to moving in a vertical direction in the plot. As γ increases, a system transitions from FP#1 (zero amplitude) to FP#2 or #3 (standing wave), and then FP#4 (mixed wave). However, when $C_{2,01}$ is zero, the system transitions directly from FP#1 to FP#4. Specifically, when the system is azimuthally uniform, $C_{2,01} = C_{2,21} = 0$, the mode exists either as a zero amplitude or a purely spinning wave, depending upon γ. Also note from $\gamma_{Hopf,1}$ that the more $C_{2,01}$ deviates from zero, the earlier the system becomes unstable, i.e., the non-uniformity accelerates the onset of the instability. Lastly, nonzero $C_{2,21}$ causes $\gamma_{Hopf,2}$ to be asymmetric about $C_{2,01} = 0$ line. To summarize, this figure clearly shows that under unstable conditions, the system can be dominated by standing, spinning, or mixed waves, and shows how the relative dominance of these waves is controlled by linear damping/amplification effects, $(\gamma = \beta/\alpha)$, and azimuthal non-uniformities, $(C_{2,01}, C_{2,21})$.

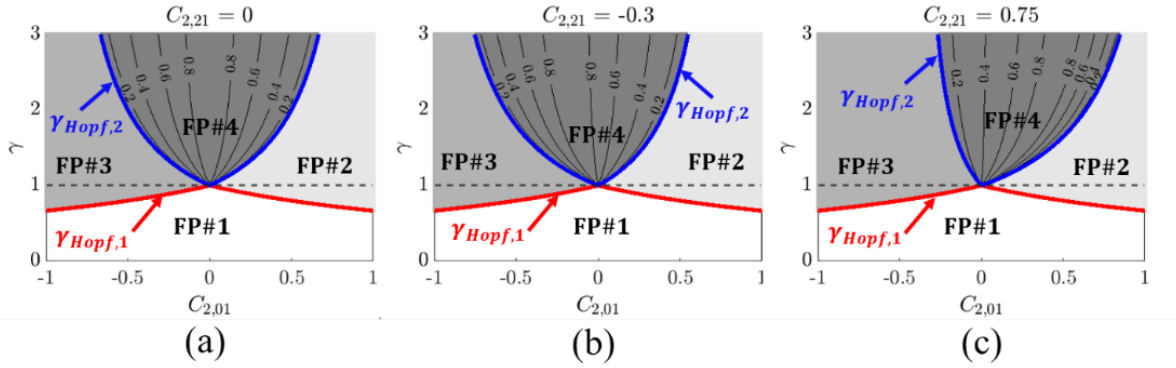

Figure 15 – Stability map in $(C_{2,01}, \gamma)$ space with difference $C_{2,21}$ values. Red and blue lines denote the first and second bifurcation boundaries. The horizontal dash line denotes $\gamma = 1$. Contour lines indicate $|SR|$.

Further insight into these FP's and their stability can be obtained from transient computations, showing the systems relaxation to these FP's from arbitrary initial conditions, see Figure 23. The first row illustrates simulations of η_1, η_2, A, B, and $\bar{\varphi}$ with different γ values. Subfigures in each plot demonstrate that the method of averaging technique closely captures the magnitudes of the second order oscillators. After each simulation, A, B, and φ are mapped into F, G, and φ_{FG}. Figure 23(a) represents the zero amplitude mode (FP#1) where $\gamma < \gamma_{Hopf,1}$, and thus, both amplitudes, A and B, decays to zero, i.e., the system is linearly stable. In this case, $\bar{\varphi}, SR$, and $\bar{\varphi}_{FG}$ do not have

any physical meaning. Figure 23(b) is the case where $\gamma_{Hopf,1} < \gamma < \gamma_{Hopf,2}$, and the system is linearly unstable. As expected, FP#2 is stable, and only A converges to a finite value since $C_{2,01} > 0$. The bottom plot shows that F and G converge to the same value, resulting in zero SR or a purely standing wave. Also note that $\bar{\varphi}_{FG}$ converges to zero, implying that the anti-nodal line ($\theta_a = -\varphi_{FG}/2$) is located horizontally. This is physically reasonable because the flames that strongly couple with acoustics are oriented in the horizontal direction for positive $C_{2,01}$. Further increase in $\gamma > \gamma_{Hopf,2}$ leads to a mixed wave as shown in Figure 23(c) where both A and B converge to finite values. This state corresponds to FP#4. In the bottom plot, F is greater than G at steady state, and thus, $SR > 0$. Notice that $\bar{\varphi}_{FG}$ converges to 1, indicating that the anti-nodal line of the mixed wave is in vertical direction.

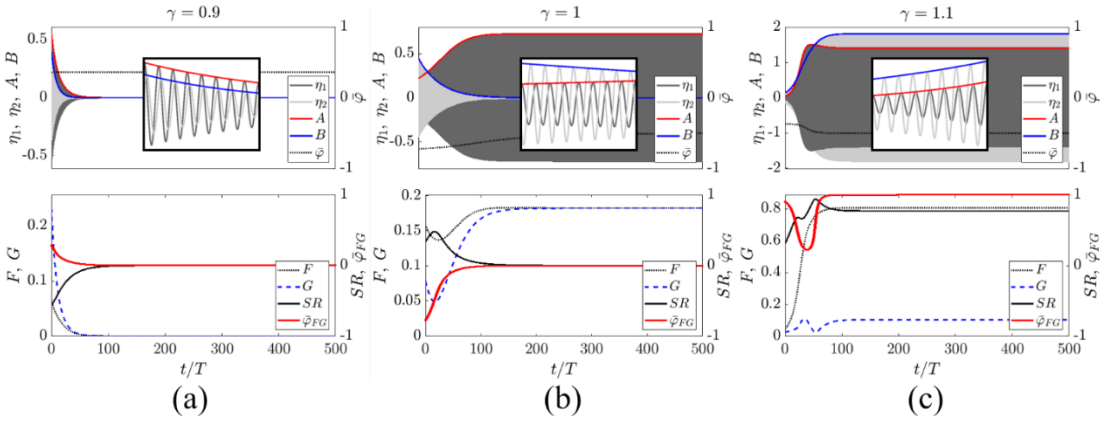

Figure 16 – First row: simulations of η_1, η_2, A, B, and $\bar{\varphi}$. Subfigures describe the dynamics of the first eight cycles. Second row: simulations of F, G, SR and $\bar{\varphi}_{FG}$. γ values are (a) 0.9, (b) 1, and (c) 1.1. The other parameters are $b_{21} = -0.05, C_{2,01} = 0.05, S_{2,10} = 0, C_{2,21} = 0.75, \bar{\omega} = 1, \Delta = 0, \Gamma = 0$. The Hopf bifurcation points are $\gamma_{Hopf,1} = 0.9757, \gamma_{Hopf,2} = 1.041$.

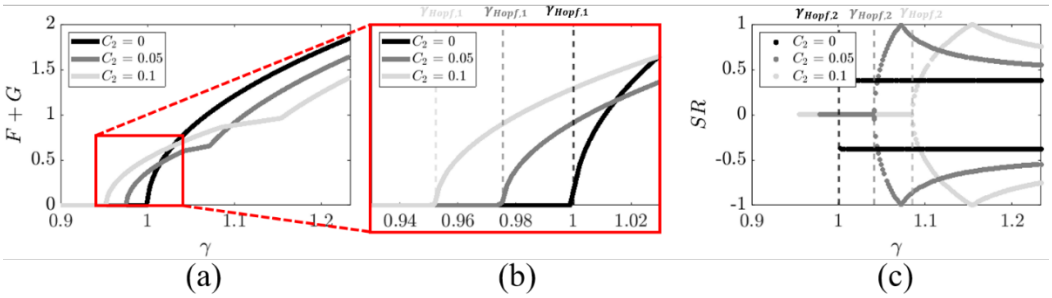

Figure 17 – (a) Pressure anti-node magnitude as a function of γ with different $C_{2,01}$ values. (b) Zoom in version of (a). (c) SR as a function of β with different $C_{2,01}$ values. The other parameters are $b_{21} = -0.05, S_{2,10} = 0, C_{2,21} = 0.75, \bar{\omega} = 1, \Delta = 0, \Gamma = 0$. The grayscale vertical lines in (b) and (c) denote the first and second bifurcation points, respectively.

Figure 17(a) describes the effect of linear damping/growth rate, γ, on the steady state pressure anti-node magnitude with different $C_{2,01}$ values, determined from computational solutions. Here, the simulation was run out to sufficient time to reach a steady state, and was repeated at different

initial conditions to explore their effects. For reference, Figure 17(b) shows a detail of Figure 17(a) with the dashed vertical lines indicating the theoretical predictions for the bifurcation points, $\gamma_{Hopf,1}$. As expected, the first Hopf bifurcation point, $\gamma_{Hopf,1}$, decreases with increasing $C_{2,01}$. In other words, the larger the azimuthal non-uniformity, the earlier the system becomes unstable. The figure also shows that the higher the non-uniformity, the slower the instability amplitude grows with γ. Figure 17(c) plots SR as a function of γ with different $C_{2,01}$ values, showing the presence of purely standing and spinning waves, as well as mixed waves. When $C_{2,01} = 0$, the azimuthal mode has a constant $SR = \pm 0.38$, or a mixed wave. For $C_{2,01} > 0$, SR starts from zero at $\gamma = \gamma_{Hopf,1}$ and maintains this value until $\gamma = \gamma_{Hopf,2}$. After $\gamma_{Hopf,2}$, SR first rapidly approaches to a pure spinning wave value of ± 1 and then decays to a mixed waves. Comparing between different $C_{2,01}$ cases, $\gamma_{Hopf,2}$ increases with increasing $C_{2,01}$, i.e., the non-uniformity delays the transition from a standing to a mixed wave. Note that there are two branches, positive and negative SR. Which branches the system is stabilized at depends on the initial conditions. Table 3 summarizes which conditions of A, B, and φ give the standing or spinning wave. For simplicity, Table 3 considers only purely standing and spinning waves. The other cases that are not described in Table 3 correspond to a mixed wave.

Table 3 – Azimuthal mode dependence on A, B, φ, F, G, and φ_{FG}

Decomposition method	Standing wave	CCW spinning wave	CW spinning wave
Two standing eigenmodes	$AB = 0$ or $\varphi = 0, \pm\pi$	$A = B$ and $\varphi = -\frac{\pi}{2}$	$A = B$ and $\varphi = \frac{\pi}{2}$
Two spinning eigenmodes	$F = G$	$F \neq 0, G = 0$	$G \neq 0, F = 0$

Next, consider the effects of frequency shift and background noise on modal interactions. Having considered the basic FPs and their stability, consider the important generalization of more general azimuthal non-uniformities (i.e., non zero $S_{2,10}$) and difference in frequencies between the two eigenmodes. Although analytical solutions are not possible for these cases, some insights into their behavior (which are confirmed from the computations shown later) can be obtained from consideration of the equation structure for small perturbations about the FPs derived earlier.
The equation for φ can be written in a "potential form" as:

$$\dot{\varphi} = -\frac{dU}{d\varphi} \tag{26}$$

where the "potential" U is given by:

$$U = -\varphi\Delta + \frac{b_{10}S_{2,10}}{2}\left(\frac{A^*/B^*}{2+\Delta} - \frac{B^*/A^*}{2-\Delta}\right)\sin\varphi + \frac{1}{2}\left(k_{\varphi A}A^{*2} + k_{\varphi B}B^{*2}\right)\cos 2\varphi \tag{27}$$

and, consistent with the approximation of considering very small departures of the system from the previous deterministic analysis, it has been assumed that the amplitudes, A and B, are constant at their FP values, A^* and B^* in this equation. The potential in Eq.(27) consists of three terms: the first term, proportional to Δ, causes φ to drift in one direction linearly with time. The second term, proportional to $S_{2,10}$, provides one-well potential at either CW or CCW spinning wave, which is determined by the sign of the second term. The third term, proportional to $k_{\varphi A}$ and $k_{\varphi B}$, provides two-well potential at both CW/CWW spinning waves. Figure 18 shows each term as a function of

φ and their contribution to the potential shape for two different cases. The figure clearly shows that $S_{2,10}$ term causes a preference to either CW or CCW spinning wave. When this term is sufficiently larger than the other terms, it will suppress one of the spinning waves, and foster the other spinning wave (Figure 18(a)). In contrast, when Δ term dominates over the other terms, φ can continuously drift in one direction (Figure 18(b)) without a local minimum, which serves as a local attractor. This drift causes not only the out-of-phase oscillations between CW/CCW amplitudes, resulting in oscillation of SR, but also the oscillation in φ_{FG}, both of which were observed experimentally.

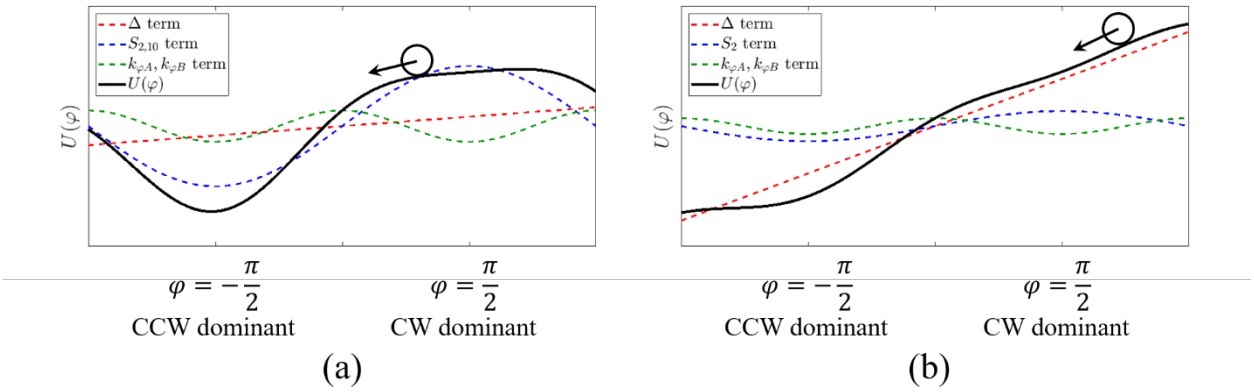

Figure 18 – Potential and contributions of each term to the potential shape for two example cases (a) $S_{2,10}$ term dominant system, leading to a local minimum in U, (b) Δ term dominant system, which has no local minimum in U.

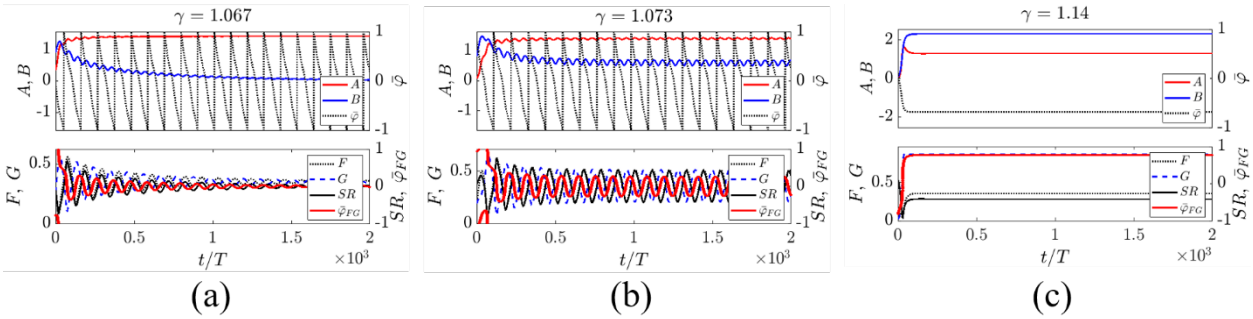

Figure 19 – First row: simulations of A, B, and $\bar{\varphi}$. Second row: simulations of F, G, SR and $\bar{\varphi}_{FG}$. γ values are (a) 1.067, (b) 1.073, and (c) 1.14. The other parameters are $b_{21} = -0.05, C_{2,01} = 0.05, S_{2,10} = 0, C_{2,21} = 0.75, \bar{\omega} = 1, \Delta = -0.01, \Gamma = 0$.

We next present computations, starting first with the case where $S_{2,10} = 0$, but $\Delta \ll 1$. Notice that in linear regime, a non-zero Δ imposes two different frequencies on the system. Depending upon the value of Δ, the ratio of the two frequencies may be irrational (i.e., quasi-periodic) or rational (leading to period-N oscillations, with the value of N being a function of Δ). We will use the word 'quasi-periodic' in the rest of this report, recognizing of course that in special cases the frequency ratio may be rational. While a non-zero Δ implies a system with two distinct frequencies in the linear case, it does not necessarily do so in the nonlinear case at steady state conditions. Nonlinearities do this in two ways- first, through amplitude dependent frequency shifts which can

synchronize the two distinct frequencies and, second, by "quenching", where two linearly unstable oscillators compete with each other and one oscillator's amplitude is driven to zero. Both behaviors are illustrated in Figure 19. The first row of Figure 19(a) shows the simulations of $A, B,$ and $\bar{\varphi}$ with a finite frequency spacing, showing how the system relaxes to "steady state" from a prescribed initial condition. In constrast to zero frequency spacing case, note from the second row of Figure 19(a) how F and G decay in an oscillatory manner towards the FP, a demonstration of quasi-periodicity. This oscillation occurs at the frequency of Δ, which will be shown later. However, the quasi-periodicity disappears at steady state because one of the oscillators (B in this case) decays to zero, resulting in a single frequency oscillation. In other words, nonlinear competition between the two standing eigenmodes leads to quenching of oscillator B, even though both oscillators are linearly unstable. This damped oscillatory behavior also manifests itself as spiral trajectories into the attractor when plotted in averaged $(SR, \bar{\varphi}_{FG})$ phase portrait. Increase in γ causes a self-sustained quasi-periodic oscillation as shown in Figure 19(b). Note from the first row that the two oscillators coexist, and their phase difference drifts in one direction, demonstrating a presence of two different frequencies in the system. The second row in Figure 19(b) shows that SR oscillates around zero, and the phase lag between $\bar{\varphi}_{FG}$ and SR is about 90°. This is in good agreement with the quasi-periodic standing wave observed in the experiments. Further increase in γ alters the system to a mixed wave as shown in Figure 19(c). The first row shows that the two oscillators coexist, but their phase difference is constant at steady state, indicating that their oscillation frequencies are synchronized. Thus, the quasi-periodicity vanishes as shown in the second row of Figure 19(c).

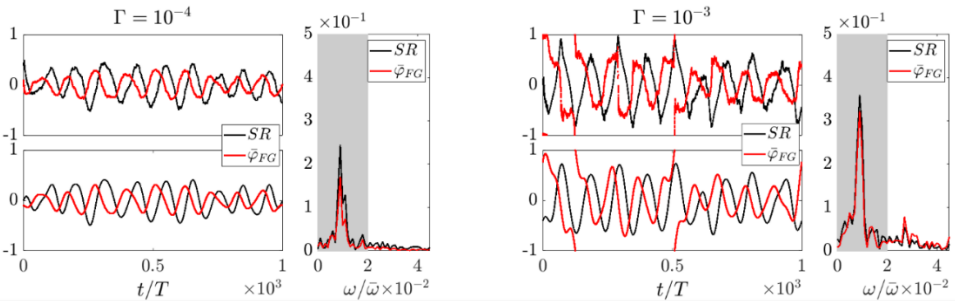

Figure 20 – Simulation of SR and $\bar{\varphi}_{FG}$ with background noise (a) $\Gamma = 10^{-4}$ and (b) $\Gamma = 10^{-3}$. Top plot: raw signal, bottom plot: filtered signal, right plot: Fourier transform. The shaded region in the Fourier transform denotes the low pass filter width. The other parameters are $\gamma = 1.067, b_{21} = -0.05, C_{2,01} = 0.05, S_{2,10} = 0, C_{2,21} = 0.75, \bar{\omega} = 1, \Delta = -0.01$.

Figure 19(a) shows that quasi-periodic behavior only appears during the initial transient. However, in the presence of background noise, the damped oscillator B will be continuously excited and the phase averaged system will be quasi-periodic. To illustrate, Figure 20 plots representative time traces, and corresponding spectra, of SR and $\bar{\varphi}_{FG}$ for computed cases with background noise of two different noise intensities. The white noise terms in the governing equation have been simulated using the Euler-Maruyama scheme. Top is the raw signal, and the bottom is the low pass filtered signal whose bandwidth is shown as the shaded region in the spectra. Notice that introducing the background noise prevents the SR and $\bar{\varphi}_{FG}$ from decaying to zero, causing them to continuously oscillate around zero, i.e., as a quasi-periodic standing wave. In

addition, noise intensity increases the oscillation amplitude. In particular, Figure 20(b) shows that sufficiently high noise intensity may cause $\bar{\varphi}_{FG}$ to jump from ± 1 to ∓ 1, e.g., at $t/T = 500$, which was also seen experimentally. Recalling that $\bar{\varphi}_{FG}$ is directly related to the anti-nodal line, this demonstrates the rotation of the anti-nodal line in CW/CCW direction.

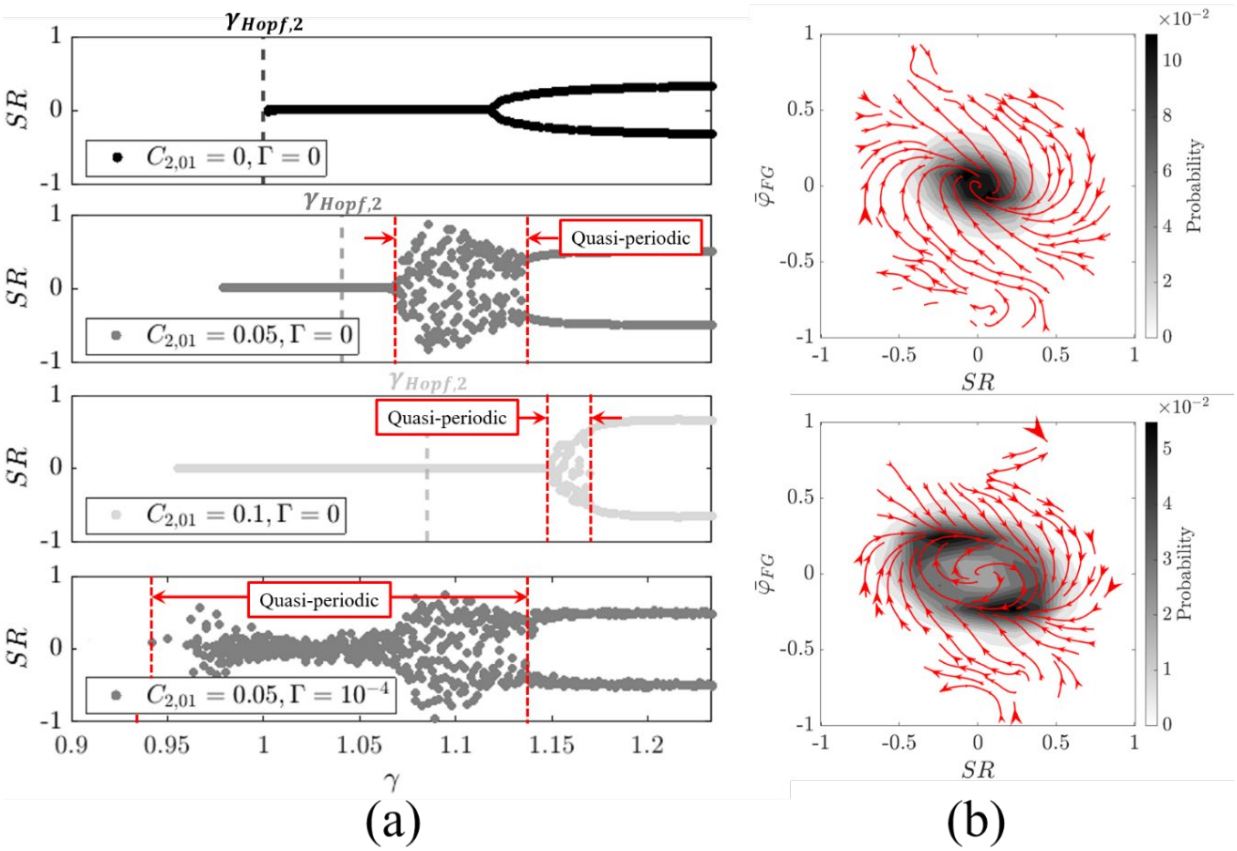

Figure 21 – (a) 1st – 3rd rows: SR as a function of γ with different $C_{2,01}$ values without noise. The grayscale vertical lines denote the second bifurcation points, $\gamma_{Hopf,2}$, when $\Delta = 0$. 4th row: SR as a function of γ with noise. The data points with anti-node magnitude less than 0.1 are omitted because of their large fluctuations. The red vertical lines denote the quasi-periodic standing wave regions. The other parameters are $b_{21} = -0.05, S_{2,10} = 0, C_{2,21} = 0.75, \bar{\omega} = 1, \Delta = -0.01$. (b) Averaged phase portrait in SR and $\bar{\varphi}_{FG}$ space. Top: $\gamma = 1.067$, bottom: $\gamma = 1.073$. The other parameters are $b_{21} = -0.05, C_{2,10} = 0.05, S_{2,10} = 0, C_{2,21} = 0.75, \bar{\omega} = 1, \Delta = -0.01, \Gamma = 10^{-4}$.

To summarize, even very small frequency shifts have profound influences on system dynamics. This is shown in the first three rows of Figure 21(a), which plots SR as a function of γ at different $C_{2,01}$ values for a noise free system, $\Gamma = 0$. $\gamma_{Hopf,2}$ for $\Delta = 0$ are indicated for comparison. Note that nonzero Δ shifts the bifurcation point from the $\gamma_{Hopf,2}$ values. The largest qualitative change is the quasi-periodic regimes. The system with non-zero Δ and $C_{2,01}$ exhibits quasi-periodic behavior for a certain range of γ without the noise contribution. However, the last row of Figure 21(a) shows that when exposed to the noise, quasi-periodic behavior occurs for the

entire range of γ before the system reaches the mixed wave solutions. This is because the noise perturbs the system from its stable FP, which relaxes back to its attractor in a weakly damped, oscillatory manner, as shown in Figure 20. This makes it difficult to differentiate between noise driven and self-sustained quasi-periodic behavior from the time trace data (Figure 20) or the bifurcation plot (the last row of Figure 21(a)). They can be differentiated, however, from the averaged phase portrait, such as shown in Figure 21(b). The phase portrait was obtained by repeating the simulations at distributed initial conditions over the phase space. The top and the bottom of Figure 21(b) are the phase portraits with the same condition as Figure 20(a) and Figure 19(b), respectively, with noise contribution. It can be seen that the center point is an attractor for the noise driven quasi-periodic case, whereas it is a repeller for the self-sustained quasi-periodic case. Also note that the trajectory and the joint PDF form a ring structure around the center.

It is also interesting to note that the trajectories are CW spiraling into/around the FP in Figure 21(b). As mentioned before, this is due to the 90° phase lag between SR and $\bar{\varphi}_{FG}$ oscillations. If SR and $\bar{\varphi}_{FG}$ exponentially decay to their FPs without oscillations such as a mixed wave solution in Figure 19(c), the trajectories in the phase portrait would directly converge to the FP without the spiraling. This behavior can be seen experimentally.

Now, consider the bifurcation plot in $(C_{2,01}, \gamma)$ space for the noise free system, but with a finite frequency spacing. Figure 22 shows regions where the system is linearly stable (zero amplitude), exhibit single frequency standing waves (i.e., nonlinear effects lead to quenching of one of the standing eigenmodes), exhibits self-sustained quasi-periodic standing waves, and exhibits single frequency mixed waves (i.e., not purely standing or spinning). This plot shows a region where the quasi-periodic behavior can occur with a noise free system. The region becomes wider with increasing frequency split. Note that even if the system's parameters are not inside the region, but close to it, the system exhibits damped oscillation as shown in Figure 19(a). However, when the system moves far away from the region, the oscillatory behavior disappears even with the noise contribution.

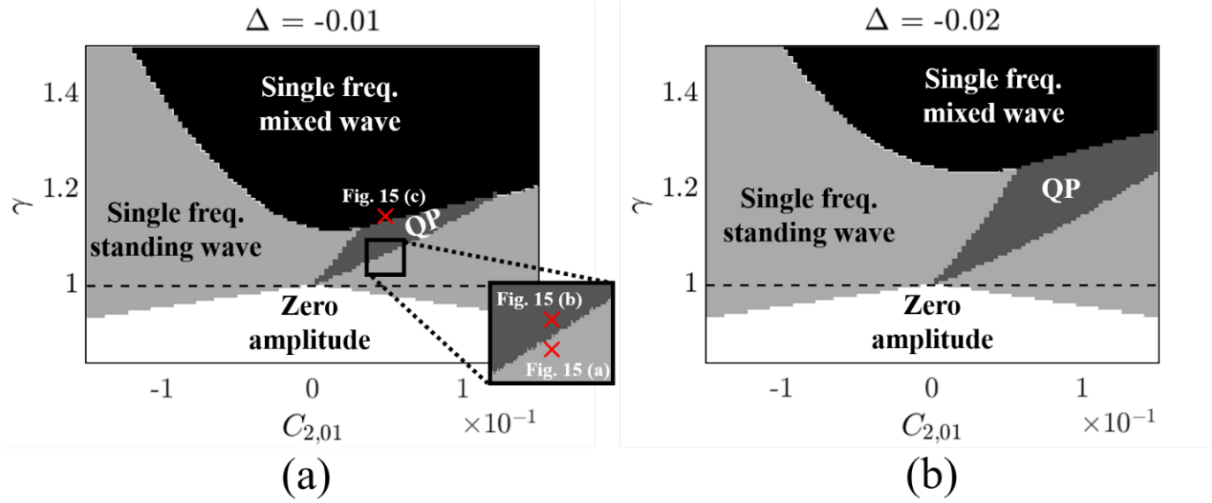

Figure 22 – Bifurcation plot in $(C_{2,01}, \gamma)$ space showing quasi-periodic behavior with two different frequency spacing values (a) $\Delta = -0.01$ and (b) $\Delta = -0.02$. Here, QP = quasi-periodic standing wave region. The horizontal dash line denotes $\gamma = 1$. The red crosses in (a) indicate $(C_{2,01}, \gamma)$ in Error! Reference source not found.**(a)-(c). The other parameters are $b_{21} = -0.05, S_{2,10} = 0, C_{2,21} = 0.75, \bar{\omega} = 1, \Gamma = 0$.**

Next, consider the effects of pressure coupled azimuthal non-uniformity and parametric noise on modal interactions. This formulation considers the case where the pressure coupled non-uniformity, $S_{2,10}$, frequency spacing, Δ, and noise, Γ, are all present. Figure 23(a) plots computated results for the anti-node pressure magnitude as a function of γ and $C_{2,01}$. Although the system is linearly stable, the magnitudes are nonzero because of the noise contribution. Other than that, Figure 23(a) exhibits similarities to the experimental data in the past report. For example, the first bifurcation point is delayed as $C_{2,01}$ gets close to zero, but its amplitude grows faster with γ.

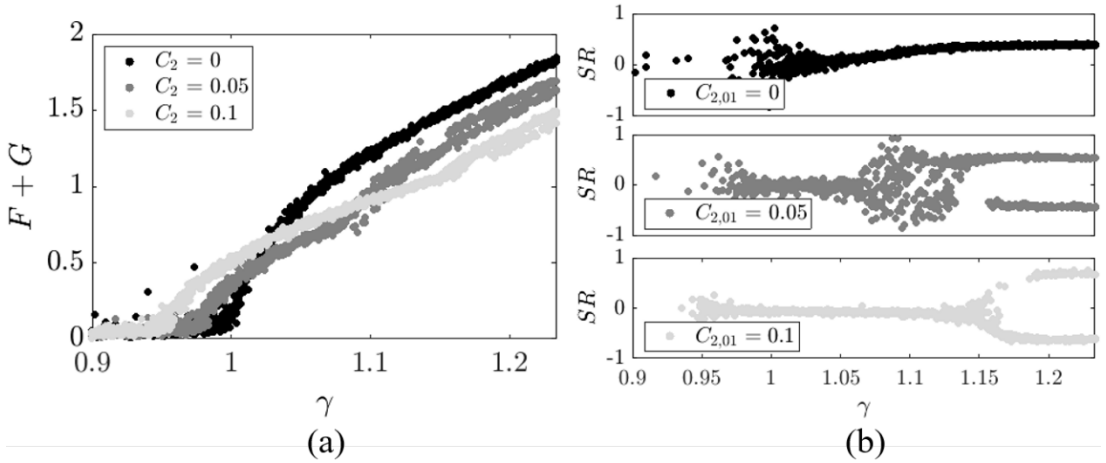

Figure 23 – (a) Pressure anti-node magnitude as a function of γ with different $C_{2,01}$ values. (b) SR as a function of γ with different $C_{2,01}$ values. The data points with anti-node magnitude less than 0.1 are omitted because of their large fluctuations. The other parameters are $b_{21} = -0.05, S_{2,10} = 0.02, C_{2,21} = 0.75, \bar{\omega} = 1, \Delta = -0.01, \Gamma = 10^{-4}$.

Figure 23(b) represents the instability amplitude and SR as a function of γ and $C_{2,01}$ with a finite non-uniformity, $S_{2,10}$. The figure clearly shows that $S_{2,10}$ imposes a preferential spinning direction. For $C_{2,01} = 0$, a system has a preference in a positive SR, or CCW direction. For $C_{2,01} = 0.05$, the system still prefers CCW to CW after the quasi-periodic standing wave, but CW direction also appears above $\gamma = 1.16$. In contrast, the system with $C_{2,01} = 0.1$ has a preference in CW direction. The change in preferential direction is due to the sign change of the second term in Eq. (2) in the previous report. To summarize, introducing the non-uniformity, $S_{2,10}$, causes a mixed/spinning wave to be biased towards either CW or CCW direction. This provides a possible explanation for why the experimental data show a bias towards positive SR values.

Next, consider parametric noise effects which, as noted in prior studies, introduces qualitatively new phenomenon. As noted earlier, certain features of the data can be understood from purely deterministic considerations, some require additive noise, and as, discussed here, some also require introducing parametric noise. In particular, within the modeling assumptions described earlier, parametric noise is required to capture the intermittency between the standing and mixed waves observed experimentally because these solutions are not simultaneously stable (whether incorporation of higher order nonlinearities, or incorporation of phase coupled nonlinearities, b_{30}, b_{12}, and b_{03}, provides solutions with intermittency is unknown). Specifically, given the fact

that the behavior of SR abruptly changes with γ, or equivalently β, for $C_{2,01} > 0$ as illustrated in Figure 23, parametric noise in β will lead to the intermittency.

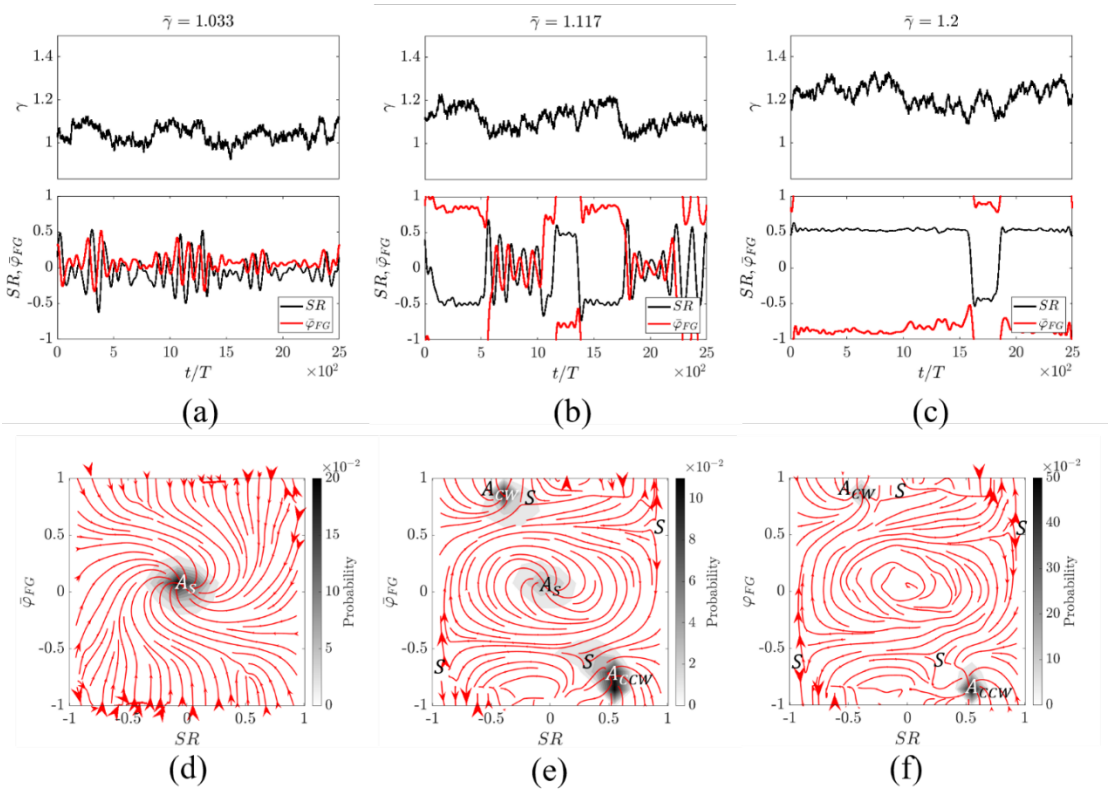

Figure 24 – Dynamics of SR and $\bar{\varphi}_{FG}$ with different mean γ that follows OU process, (a) $\bar{\gamma} = 1.033$, (b) $\bar{\gamma} = 1.117$, (c) $\bar{\gamma} = 1.2$. Simulated phase portrait for (a) $\bar{\gamma} = 1.033$, (b) $\bar{\gamma} = 1.117$, (c) $\bar{\gamma} = 1.2$. The other parameters are $b_{21} = -0.05, C_{2,01} = 0.05, S_{2,10} = 0.02, C_{2,21} = 0.75, \bar{\omega} = 1, \Delta = -0.01, \Gamma = 10^{-4}$.

To illustrate, we consider parameteric fluctuations in the parameter β, i.e., $h_2(p, \dot{p}) = \beta\dot{p}$, and assume that the noise term, $\xi_2(t)$, follows the Ornstein–Uhlenbeck (OU) process, which drifts toward its mean value over time, numerically simulated with the Euler-Maruyama scheme. This process is more appropriate than the Brownian motion, where the variance grows with time (i.e., in an unbounded fashion); in contrast, the variance for the OU process reaches a constant value. Figure 24 illustrates three representative cases with $C_{2,01} = 0.05$ where the asymptotic means of γ are $\bar{\gamma} = 1.033, 1.117$, and 1.2. Figure 24(a) – (c) describes the time trace of γ (top) as well as SR and $\bar{\varphi}_{FG}$ (bottom), and Figure 24(d) – (f) represents the average phase portrait for each case. For $\bar{\gamma} = 1.033$ (Figure 24(a)), both SR and $\bar{\varphi}_{FG}$ fluctuate around zero. Note that the modulation amplitude is not steady because of time varying $\gamma(t)$. The dynamics of SR and $\bar{\varphi}_{FG}$ resembles the experimental data. The phase portrait in Figure 24(d) shows a stable attractor at the center (A_S), and the trajectories are spiraling into the attractor. These results resemble the experimental observations. When $\bar{\gamma} = 1.117$, SR and $\bar{\varphi}_{FG}$ start to show intermittency. In particular, transition of SR and $\bar{\varphi}_{FG}$ from one state to the other occurs simultaneously, which was evident from the experimental data. In the simulation, they are hopping between three different states, i.e., quasi-periodic standing wave, and CCW/CW mixed waves. The phase portrait in Figure 24(e) reveals

three attractors, $A_S, A_{CW/CCW}$, as well as multiple saddle points. Notice that the joint PDF around A_{CCW} is denser than that around A_{CW}, manifesting the system's preference in a CCW mixed wave. The portrait reasonably concides with the experimental phase portrait. Lastly, for $\bar{\gamma} = 1.2$ (Figure 24(c)), SR stays either CW or CCW dominant wave, and $\bar{\varphi}_{FG}$ remains around ± 1. The transition between two states may occur when γ drops below a certain value. The corresponding phase portrait in Figure 24(f) manifests two stable attractors, $A_{CW/CCW}$, and multiple saddle points. Here, A_S is no longer a stable attractor, which explains the reason for no realization at the center in the experimental phase portrait. Similar to Figure 24(e), the joint PDF demonstrates the preference in CCW spinning wave.

In this task, we presented experimental and modeling work to better understand wave structures and temporal dynamics of azimuthal modes in combustors. The experimental data was obtained from an industrial scale combustor, specifically developed to control the azimuthal fuel distribution. For the uniform staging, the azimuthal mode exhibited a variety of behaviors, e.g., quasi-periodic standing, mixed waves as well as intermittency. When the fuel was staged in a non-uniform manner, however, only the quasi-periodic standing wave was observed. In order to capture these dynamics, a weakly nonlinear model formulation was used, derived from the wave equation and a generalized source term. The source term was modeled with a Taylor expansion up to fourth order with the additive and parametric noise terms. Each coefficient in the expansion was allowed to vary azimuthally. This model clearly showed that these parameters influence the azimuthal mode stability as follows.

- Linear damping/growth coefficients, α and β, determines the linear stability of two standing eigenmodes.
- The parameter, $C_{2n,01}$, describing the azimuthal non-uniform coupling between the source and $\dot{p}$, influences both linear (stability boundary) and nonlinear process (dependence of limit cycle amplitude, such as upon β).
- The parameter, $C_{2n,21}$, describing the azimuthal non-uniform coupling between the source and $p^2\dot{p}$, affects relative preference between standing and spinning/mixed waves.
- The parameter, $S_{2n,10}$, describing the azimuthal non-uniform coupling between the source and p, introduces a preference in CW/CCW spinning direction on the system.
- The parameter, $C_{2n,10}$, describing the azimuthal non-uniform coupling between the source and p, causes a frequency split between the two orthogonal standing eigenmodes, Δ, which introduces quasi-periodic oscillations. The system can decay or self-excited in oscillatory manner depending upon β.
- Additive noise, Γ, with non-zero Δ leads to quasi-periodic oscillations, even in cases where the limit cycle FP is stable, as it excites oscillatory, but decaying, disturbances around the limit cycle FP at a specific frequency, Δ.
- Parametric noise, ξ_2, is responsible for the intermittency between standing and spinning/mixed waves.

As shown, these results provide significant insight into the experimentally observed behaviors. However, a few key questions remain for future study. First, for the simplified equations considered here, further analytical work on the case where Δ is not zero will be very useful, in particular to map out parametric dependencies of the stability of the limit cycle FPs. As shown here, even in cases where the limit cycle FP is stable, in cases where the orbits decay in an oscillatory manner, the stable orbit leads to damped, quasi-periodic oscillations, such as shown in the experimental phase space plots. Second, it will be useful to analyze the effects of the neglected

parameters, $b_{30}, b_{12},$ and b_{03}, which introduce phase coupling. This could be computational or analytical work. An important conclusion from this work for the simplified equations were that both standing and spinning/mixed wave limit cycles were not simultaneously stable. However, both FP's are clearly observed in the experimental phase portraits, an observation that we could emulate by incorporation of parametric noise. However, it is possible that these additional nonlinearites could cause overlap in stability boundaries.

Task 3 – Modeling of Flame Response

The goal of this task was to enable further understanding of the flame response in multi-nozzle systems through phenomenological reduced order models with a focus on velocity-coupled and pressure-coupled flame response. The overall stability of the combustion system is determined by the coupling between unsteady pressure and unsteady heat release rate disturbances as seen from the volume integrated acoustic energy equation:

$$\frac{\partial}{\partial t}\iiint_V e_1 dV = \frac{\gamma-1}{\gamma p_0}\iiint_V \left(p_1\dot{q}_1\right)dV - \oiint_S p_1\left(\vec{u}_1\cdot d\vec{S}\right) \tag{28}$$

Thus, the acoustic energy in the domain grows if the RHS is positive:

$$\frac{\gamma-1}{\gamma p_0}\iiint_V \left(p_1\dot{q}_1\right)dV > \oiint_S p_1\left(\vec{u}_1\cdot d\vec{S}\right) \tag{29}$$

The integral on the LHS of this inequality is a gain term and corresponds to the Rayleigh Integral while that on the RHS corresponds to acoustic losses at the boundaries, specifically the inlet and outlet of the combustor volume. Thus, a necessary, but not sufficient condition for instability is that the Rayleigh Integral must be positive:

$$RI = \int_t \oint_V p_1\dot{q}_1 dV dt > 0 \tag{30}$$

Here, *RI* denotes the Rayleigh Index.

The acoustic velocity fluctuations arising from the natural modes of the combustor are the source fluctuations which also excite vortical velocity fluctuations that are due to the natural hydrodynamics in the flow. The combination of these fluctuations results in flame area and/or mass burning rate fluctuations. We refer here to the response of the flame to the acoustic velocity itself as the "direct response" (as opposed to the "indirect" response of the vortical disturbances that are excited by the acoustics).

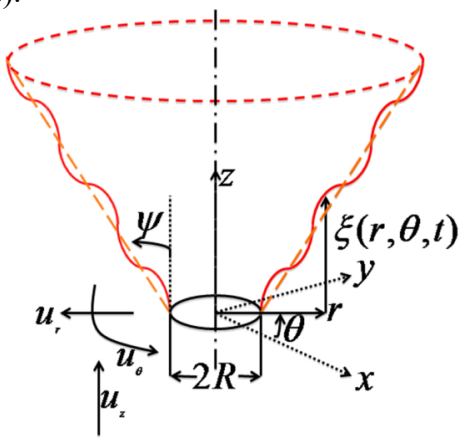

Figure 25 – Schematic of the center-body swirl-stabilized premixed flame.

The flame schematic in as shown in Figure 25. The flame base is assumed to be anchored at the center-body implying:

$$\xi\left(r=R,\theta,t\right)=0 \tag{31}$$

The flame is assumed to be located at the zero contour of an implicit function using which an explicit governing equation for the flame position in polar coordinates is obtained as:

$$\frac{\partial\xi}{\partial t}+u_r\frac{\partial\xi}{\partial r}+\frac{u_\theta}{r}\frac{\partial\xi}{\partial\theta}+s_L\left[\left(\frac{\partial\xi}{\partial r}\right)^2+\frac{1}{r^2}\left(\frac{\partial\xi}{\partial\theta}\right)^2+1\right]^{1/2}=u_z \tag{32}$$

The velocity field can be decomposed in terms of the unperturbed (subscript '0') and a spatio-temporally varying disturbance (subscript '1' for linear first-order), as:

$$u_i\left(r,\theta,t\right)=u_{i,0}\left(r,\theta\right)+\varepsilon u_{i,1}\left(r,\theta,t\right) \tag{33}$$

Where the sub-script '*i*' denotes the *r,* θ or z coordinate. Similar to the velocity decomposition in Eq.(33), the flame position is expanded as:

$$\xi(r,\theta,t)=\xi_0(r,\theta)+\varepsilon\xi_1(r,\theta,t)+O(\varepsilon^2) \tag{34}$$

The evolution equations for the unperturbed flame (ξ_0) and the local flame dynamics (ξ_1) may then be written as:

$$u_{r,0}\frac{\partial\xi_0}{\partial r}+\frac{u_{\theta,0}}{r}\frac{\partial\xi_0}{\partial\theta}=u_{z,0}-s_L\left[1+\left(\frac{\partial\xi_0}{\partial r}\right)^2+\left(\frac{1}{r}\frac{\partial\xi_0}{\partial\theta}\right)^2\right]^{1/2} \tag{35}$$

$$\frac{\partial\xi_1}{\partial t}+\vec{u}_{0,T}\cdot\vec{\nabla}\xi_1=\left(u_{z,1}-u_{r,1}\cot\psi-\frac{u_{\theta,1}}{r}\frac{\partial\xi_0}{\partial\theta}\right) \tag{36}$$

Here,

$$\frac{\partial\xi_0}{\partial r}=\cot\psi(r) \tag{37}$$

and the net tangential velocity vector along the flame surface, due to both the azimuthal and axial velocity components, is given by:

$$\vec{u}_{0,T}=\vec{u}_0-s_L\vec{e}_n \tag{38}$$

Here, $\vec{e}_n$ is the local unit normal vector, pointing from the nominal unperturbed flame surface into the products.

The swirl-stabilized premixed flame is assumed to be enclosed in a cylindrical combustor of length L_C and radius R_C. The natural acoustic disturbances (at frequencies ω_0) are:

$$\begin{aligned}&\frac{p_1(r,\theta,z,t)}{\rho_0c_0^2}=\mathrm{Re}\left\{\hat{p}_1(r,\theta,z)\exp\left(-i\omega_0t\right)\right\}\\&\hat{p}_1(r,\theta,z)=J_m(\alpha_{l,m}\beta_fr)\cos\left(m\theta-\theta_m\right)\cos\left(n\pi z\frac{\beta_f}{\beta_C}\right)\end{aligned} \tag{39}$$

Here,

$$\beta_f=\frac{L_f}{R_C}\qquad\beta_C=\frac{L_C}{R_C} \tag{40}$$

Note that the axial ends of the combustor at $z=0$ and $z=L$ are assumed to be rigid. The overhat notation is used to denote complex frequency domain equivalents of the time-domain quantities.

The axial mode number is denoted by *n*, the azimuthal mode number by *m* and the radial mode number by *l* and $\alpha_{l,m}$ is determined as roots of:

$$J'_m(\alpha_{l,m}) = 0 \tag{41}$$

The first set of roots for different radial and azimuthal mode numbers are shown in Table 4.
The non-dimensional Eigen-frequency is given by:

$$\omega_C = \frac{\omega_0 L_C}{c_0} = \sqrt{\alpha_{l,m}^2 \beta_C^2 + (n\pi)^2} \tag{42}$$

Table 4 – Roots of Eq.(41)

$\alpha_{l,m}/2\pi$	$m=0$	$m=1$	$m=2$	$m=3$	$m=4$	$m=5$
$l=1$	0	0.2930	0.4861	0.6686	0.8463	1.0211
$l=2$	0.6098	0.8485	1.0673	1.2757	1.4773	1.6743
$l=3$	1.1166	1.3586	1.5867	1.8058	2.0184	2.2261
$l=4$	1.6192	1.8631	2.0961	2.3214	2.5408	2.7554
$l=5$	2.1205	2.3656	2.6018	2.8312	3.0551	3.2747

Using the linearized Euler equation, the acoustic velocities are:

$$\begin{aligned}
\hat{u}_{z,1}(r,\theta,z) &= \frac{in\pi}{M_0\omega_C} J_m\left(\alpha_{l,m}\beta_f r\right)\cos\left(m\theta-\theta_m\right)\sin\left(n\pi z\frac{\beta_f}{\beta_C}\right) \\
\hat{u}_{r,1}(r,\theta,z) &= \frac{i\alpha_{l,m}\beta_C}{2M_0\omega_C}\left[J_{m+1}\left(\alpha_{l,m}\beta_f r\right)-J_{m-1}\left(\alpha_{l,m}\beta_f r\right)\right]\cos\left(m\theta-\theta_m\right)\cos\left(n\pi z\frac{\beta_f}{\beta_C}\right) \\
\hat{u}_{\theta,1}(r,\theta,z) &= \frac{im}{M_0\omega_C r}\left(\frac{\beta_C}{\beta_f}\right)J_m\left(\alpha_{l,m}\beta_f r\right)\sin\left(m\theta-\theta_m\right)\cos\left(n\pi z\frac{\beta_f}{\beta_C}\right)
\end{aligned} \tag{43}$$

Here, the velocities have been normalized by U_0 and the mean flow Mach number is given by:

$$M_0 = \frac{U_0}{c_0} \tag{44}$$

While the Mach number is not the natural normalization parameter for the acoustic velocity, it turns out to be a convenient for the Rayleigh index calculations. For convenience of notation, the velocity fields are decomposed into azimuthal components as:

$$\hat{u}_{i,1}(r,\theta,z) = \sum_{m=-\infty}^{+\infty} \hat{\Gamma}_{i,m}(r,z)e^{im\theta} \tag{45}$$

Thus, for a chosen azimuthal component (i.e., $\hat{\Gamma}_{i,m}(r,z)$) in the acoustic velocity, we have:

$$\begin{aligned}
\hat{\Gamma}_{z,\pm m}(r,z) &= \frac{in\pi}{2M_0\omega_C} J_{|m|}\left(\alpha_{l,m}\beta_f r\right)e^{\mp i\theta_m}\sin\left(n\pi z\frac{\beta_f}{\beta_C}\right) \\
\hat{\Gamma}_{r,\pm m}(r,z) &= \frac{i\alpha_{l,m}\beta_C}{4M_0\omega_C}\left[J_{|m|+1}\left(\alpha_{l,m}\beta_f r\right)-J_{|m|-1}\left(\alpha_{l,m}\beta_f r\right)\right]e^{\mp i\theta_m}\cos\left(n\pi z\frac{\beta_f}{\beta_C}\right) \\
\hat{\Gamma}_{\theta,\pm m}(r,z) &= \pm\frac{m}{2M_0\omega_C r}\left(\frac{\beta_C}{\beta_f}\right)J_{|m|}\left(\alpha_{l,m}\beta_f r\right)e^{\mp i\theta_m}\cos\left(n\pi z\frac{\beta_f}{\beta_C}\right)
\end{aligned} \tag{46}$$

These acoustic velocities shall be used as source terms in the flame dynamics model of Eq.(36). Next, consider the unsteady heat release disturbances from the flame. The local unsteady heat release per unit area of a premixed flame is given by:

$$\dot{q} = \rho_u s_L h_R \tag{47}$$

Here, ρ_u is the unburnt reactant density, s_L is the flame propagation speed and h_R is the heat of reaction. Note that these quantities are constant under the assumptions of the analysis and thus any oscillations are introduced purely by changes in the local flame area element given by:

$$dA = rdrd\theta\sqrt{1+\left(\frac{\partial\xi}{\partial r}\right)^2+\frac{1}{r^2}\left(\frac{\partial\xi}{\partial\theta}\right)^2} \tag{48}$$

Linearizing this equation, the unsteady heat release rate oscillations are given by:

$$\dot{q}_1 \sim \cos\psi\rho_u s_L h_R \frac{\partial\xi_1}{\partial r} = \cos\psi\rho_u s_L h_R \,\mathrm{Re}\left\{\left(\frac{d\hat{\zeta}_{1,-m}(r)}{dr}e^{-im\theta}+\frac{d\hat{\zeta}_{1,m}(r)}{dr}e^{im\theta}\right)e^{-i\tilde{\omega}t}\right\} \tag{49}$$

The Rayleigh Index is evaluated at the Eigen-frequencies:

$$RI \sim \int_t dt\int_r rdr\int_{\theta=0}^{2\pi}\mathrm{Re}\left\{\hat{p}_1\left(r,\theta,z=\xi_0(r)\right)e^{-i\tilde{\omega}t}\right\}\mathrm{Re}\left\{\left(\frac{d\hat{\zeta}_{1,-m}(r)}{dr}e^{-im\theta}+\frac{d\hat{\zeta}_{1,m}(r)}{dr}e^{im\theta}\right)e^{-i\tilde{\omega}t}\right\}d\theta \tag{50}$$

The integrated acoustic energy at the chosen Eigen-frequency is given by:

$$E \sim \int_t dt\int_r rdr\int_{\theta=0}^{2\pi}\left[\begin{array}{l}\mathrm{Re}\left\{\hat{p}_1\left(r,\theta,z=\xi_0(r)\right)e^{-i\tilde{\omega}t}\right\}\mathrm{Re}\left\{\hat{p}_1\left(r,\theta,z=\xi_0(r)\right)e^{-i\tilde{\omega}t}\right\}\\ +\frac{1}{2}\mathrm{Re}\left\{\hat{\vec{u}}_1\left(r,\theta,z=\xi_0(r)\right)e^{-i\tilde{\omega}t}\right\}\bullet\mathrm{Re}\left\{\hat{\vec{u}}_1\left(r,\theta,z=\xi_0(r)\right)e^{-i\tilde{\omega}t}\right\}\end{array}\right]d\theta \tag{51}$$

A normalized Rayleigh index is then defined as:

$$\Re = \frac{RI}{2E} \tag{52}$$

Physically, $\Re$ corresponds to the exponential growth or decay rate of the disturbances. This normalized Rayleigh Index can be calculated for different values of the control parameters and can then be used to determine if it is positive or negative for a given mode for a chosen flame/flow configuration.

The flame response in the velocity-coupled mechanism includes the direct response to the natural acoustic modes and the response to the induced axial velocity at each nozzle. We shall systematically consider the response of the flame to different cases of the velocity model and flame attributes.

Direct Flame Response: Center Nozzle Axisymmetric Mean Flame

As the first example, we shall consider the response of the flame centered in the combustor, to various transverse modes and the effect of different parameters on the stability of the flame. The following mean-flow and flame configuration is assumed:

$$\left.\begin{array}{l}u_{z,0}=U_0\\ u_{r,0}=0\\ u_{\theta,0}=\Omega r\end{array}\right\}\Rightarrow\xi_0(r)=(r-\frac{\beta_R}{\beta_f})\cot\psi;s_L=\sin\psi \tag{53}$$

Here:

$$\beta_R = \frac{R}{R_C} \tag{54}$$

$$\beta_f = \left(1-\beta_R\right)\cot\psi \tag{55}$$

The frequency domain representation for the flame dynamics is given by:

$$\xi_1\left(r,\theta,t\right) = \mathrm{Re}\left\{\hat{\xi}_1\left(r,\theta\right)e^{-i\omega t}\right\} \tag{56}$$

The flame response can be decomposed into its azimuthal components as:

$$\hat{\xi}_1\left(r,\theta\right) = \sum_{m=-\infty}^{\infty} \hat{\zeta}_{1,m}\left(r\right)e^{im\theta} \tag{57}$$

Solving, we have:

$$\hat{\zeta}_{1,m}(r) = e^{-i\chi_m r}\int_{\beta_R/\beta_f}^{r} e^{i\chi_m r}\frac{\left(\hat{\Gamma}_{z,m} - \hat{\Gamma}_{r,m}\cot\psi\right)}{\cos\psi\sin\psi}dr \tag{58}$$

Here,

$$\begin{aligned} St &= \frac{\tilde{\omega}}{\cos\psi\sin\psi} & St_\Omega &= \frac{\Omega L_f}{u_0} \\ \tilde{\omega} &= \frac{\omega_C}{M_0}\left(\frac{\beta_f}{\beta_C}\right) & \sigma &= \frac{St_\Omega}{\tilde{\omega}} \\ \chi_m &= St\left(m\sigma - 1\right) \end{aligned} \tag{59}$$

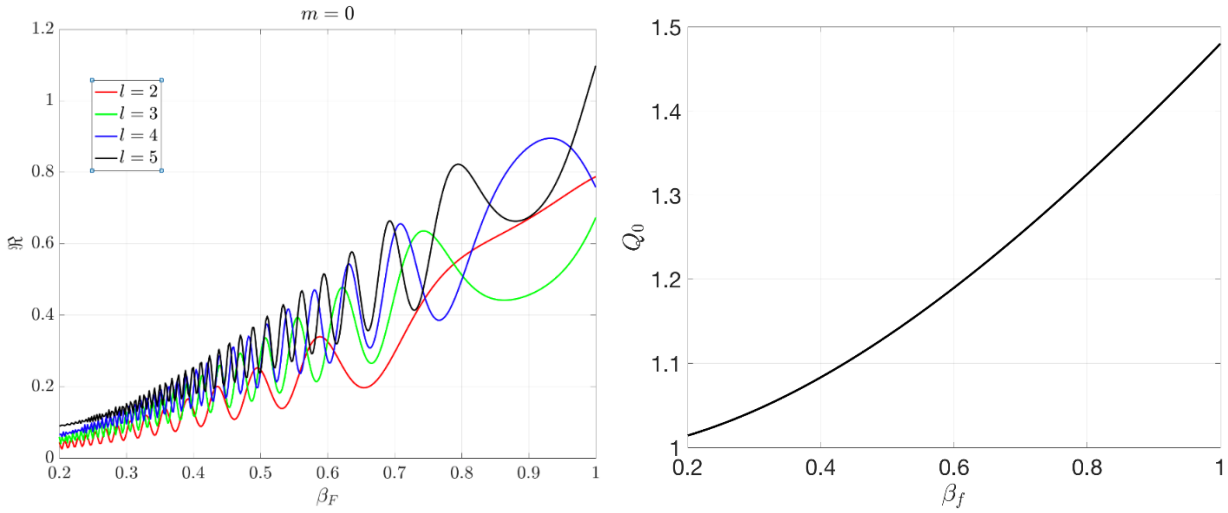

(a) **(b)**

Figure 26 – (a) Normalized Rayleigh Index map ($\Re$) as a function of flame aspect ratio (β_f) for different purely radial modes ($m = 0, 2 \le l \le 5$). (b) Normalized total heat release as a function of the flame aspect ratio.

First consider the purely radial modes corresponding to $m = 0$. Note that for this case, the normalized Rayleigh Index is not a function of the swirl parameter St_Ω. Thus, $\Re$ varies only with the flame aspect ratio β_f as shown in Figure 26(a). Note that for all the radial modes, $\Re$ is always

positive. The growth rate increases as the flame aspect ratio increases and is also seen to generally increase with the radial mode number. This behavior is also due to the fact that as the flame aspect ratio increases, the normalized total heat release increases as shown in Figure 26(b). The oscillatory pattern seen stems from the interference of wrinkles on the flame surface with spatially varying wrinkling magnitude that oscillates due to both the trigonometric terms as well as the Bessel function terms in the velocity oscillations.

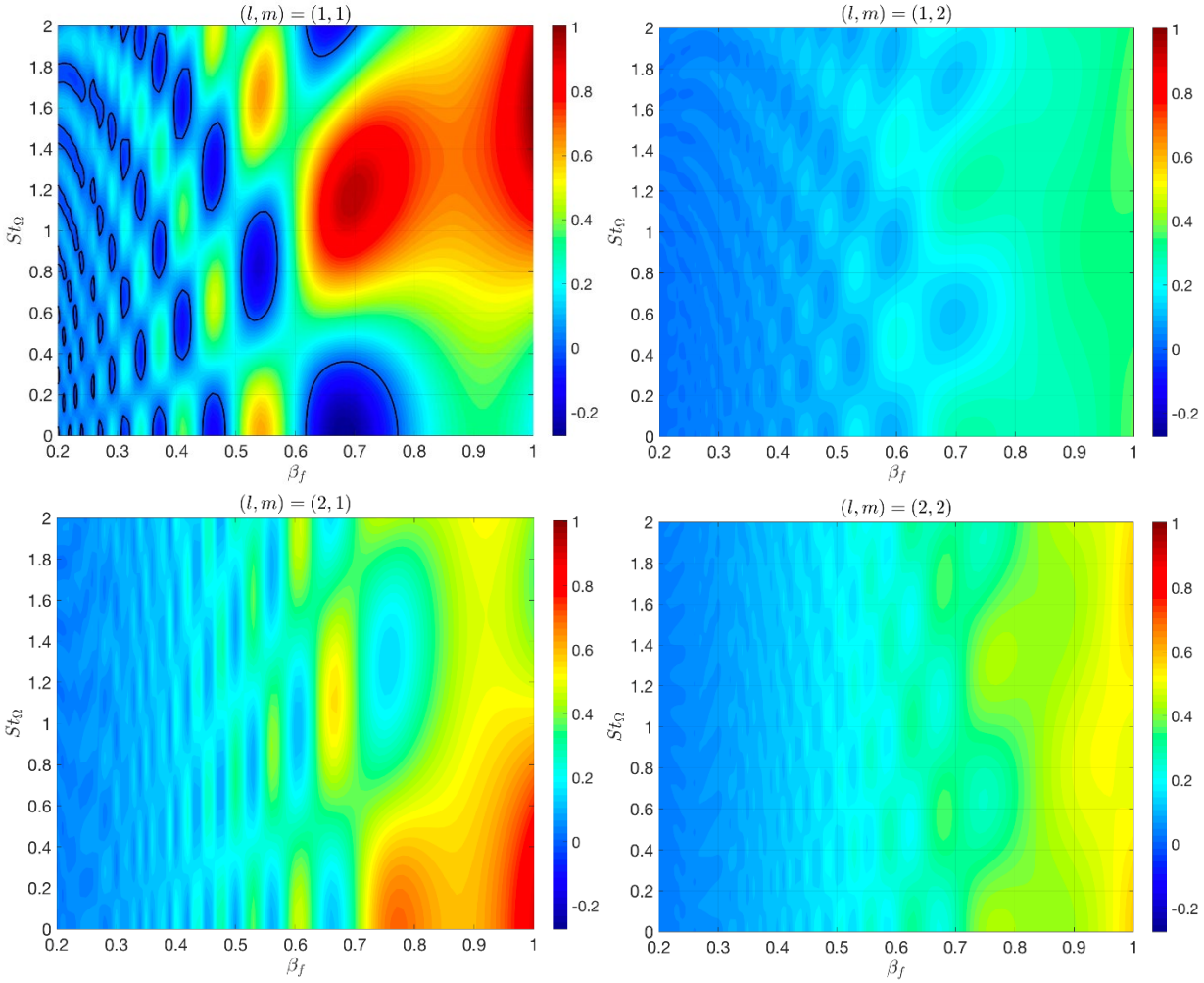

Figure 27 – Normalized Rayleigh Index map ($\Re$) as a function of flame aspect ratio (β_f) and Strouhal number based on swirling time scale (St_Ω). The black curves correspond to boundaries ($\Re = 0$) between the $\Re > 0$ and the $\Re < 0$ region. The radial and azimuthal mode numbers are indicated in the title of each plot.

Next, we consider the stability for the mixed modes ($m \neq 0$). Here, $\Re$ is a function of both the flame aspect ratio (β_f) as well as the swirl parameter (St_Ω) and so the stability maps are depicted as contour plots as shown in Figure 27. In these plots, the black curves correspond to iso-contours of $\Re = 0$. Note that these iso-contours exist only for the $(l,m) = (1,1)$ case for the chosen set of parameters. In other words, $\Re > 0$ or $\Re < 0$ for this mode. In addition, while this mode is the only one of those shown where $\Re < 0$, it also has the highest values of $\Re$ when it is positive,

corresponding to the darker shades of red in the colormap. All the other modes have $\Re > 0$ for all parameter conditions. As the radial and/or azimuthal mode number increases, $\Re$ decreases but remains positive across the entire range of values indicating that the higher azimuthal and radial mode numbers are always unstable. Also of note is that $\Re$ decreases considerably as we increase the azimuthal mode number when compared to increase in the radial mode number. This indicates a general tendency for flames to be relatively less unstable in higher azimuthal modes than in higher radial modes. Thus, using these as a guide along with a linear acoustic analysis of the combustor, an initial design point for the flame and flow configuration can be obtained in order to have relatively more stable thermoacoustic conditions.

Direct Flame Response: Outer Nozzle Axisymmetric Mean Flame

Note that center and outer nozzles do not see the same spatial variations in the mode-shape and thus will respond to the same mode differently. For a cylindrical combustor of radius R_C, the polar coordinate system used for the cylindrical combustor's axis and the relative position of the offset flame are shown in Figure 28.

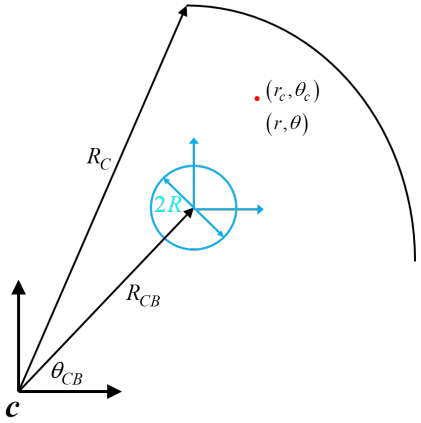

Figure 28 – Coordinate system for offset flame relative to the coordinate system for the cylindrical combustor (subscript '*c*'). The flame centered coordinate system is as shown in Figure 25.

The pressure and acoustic velocity disturbances for the purely transverse modes are given by:

$$\hat{p}_{c,1}(r_c,\theta_c) = J_{m_a}(\alpha_{l,m_a}\beta_f r_c)\cos(m_a\theta_c)$$

$$\hat{u}_{r_c,1}(r_c,\theta_c) = \frac{i}{2M_0}\left[J_{m_a+1}(\alpha_{l,m_a}\beta_f r_c) - J_{m_a-1}(\alpha_{l,m_a}\beta_f r_c)\right]\cos(m_a\theta_c) \tag{60}$$

$$\hat{u}_{\theta_c,1}(r_c,\theta_c) = \frac{im_a}{M_0\alpha_{l,m_a}\beta_f r_c}J_{m_a}(\alpha_{l,m_a}\beta_f r_c)\sin(m_a\theta_c)$$

Here,

$$\beta_f = \frac{L_f}{R_C} \qquad M_0 = \frac{U_0}{c_0} \tag{61}$$

The overhat notation is used to denote complex frequency domain equivalents of the time-domain quantities. The coordinates have been normalized by the flame length, L_f and the velocities have been normalized by U_0. For this case, the non-dimensional Eigen-frequency is given by:

$$\omega_C = \frac{\omega_0 R_C}{c_0} = \alpha_{l,m_a} \tag{62}$$

The above radial and azimuthal velocities in the combustor reference frame are transformed to the reference frame of the flame's coordinate system, using the transformation:

$$\begin{matrix} r_c(r,\theta) \\ \theta_c(r,\theta) \end{matrix} \rightarrow \begin{cases} r_c^2 = R_{CB}^2 + r^2 + 2R_{CB} r\cos(\theta - \theta_{CB}) \\ \tan\theta_c = \dfrac{R_{CB}\sin\theta_{CB} + r\sin\theta}{R_{CB}\cos\theta_{CB} + r\cos\theta} \end{cases} \tag{63}$$

The velocity field in the cylinder's coordinate system are transformed to the flame's coordinate system using:

$$\begin{aligned} \hat{u}_{r,1}(r,\theta) &= \begin{cases} \hat{u}_{r_c,1}\left(r_c(r,\theta),\theta_c(r,\theta)\right)\cos\left(\theta - \theta_c(r,\theta)\right) \\ +\hat{u}_{\theta_c,1}\left(r_c(r,\theta),\theta_c(r,\theta)\right)\sin\left(\theta - \theta_c(r,\theta)\right) \end{cases} \\ \hat{u}_{\theta,1}(r,\theta) &= \begin{cases} -\hat{u}_{r_c,1}\left(r_c(r,\theta),\theta_c(r,\theta)\right)\sin\left(\theta - \theta_c(r,\theta)\right) \\ +\hat{u}_{\theta_c,1}\left(r_c(r,\theta),\theta_c(r,\theta)\right)\cos\left(\theta - \theta_c(r,\theta)\right) \end{cases} \end{aligned} \tag{64}$$

Note that for the axisymmetric flame, the above azimuthal velocity component does not affect the flame response. However, note that the azimuthal velocity component in the acoustic field does affect the flame response through the radial velocity component. From Eq.(63), we can see that when the nozzle is not offset (i.e., $R_{CB} = 0$), we have: $r_c \equiv r$ and $\theta_c \equiv \theta$ and thus in Eq.(64) we have: $\hat{u}_{r,1} \equiv \hat{u}_{r_c,1}$ and the acoustic azimuthal velocity component does not affect the flame response. However, for any flame offset, this results in $\theta \neq \theta_c$ and thus, the acoustic azimuthal velocity component affects the flame response through the local radial velocity component of the disturbances at the flame. This has important implications on how the nozzle offset affects the local flame response and hence the stability of the mode. We shall use the same model flow-field and flame shape as earlier and consider only the first radial mode ($(l,m_a) = (2,0)$) and the first radial-azimuthal mode ($(l,m_a) = (1,1)$). The effect of nozzle positioning is determined using the radial offset parameter, R_{CB}, and the azimuthal offset parameter, θ_{CB}.

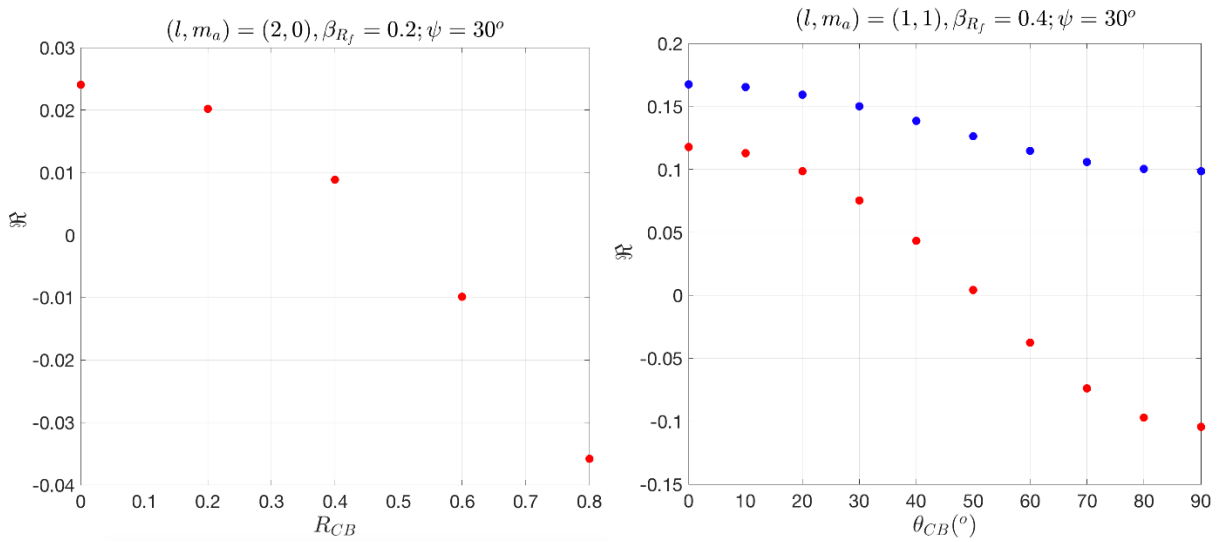

Figure 29 – (a) Effect of nozzle offset on the stability of the first radial mode. Nozzle offset is purely determined by the radial offset of the nozzle. (b) Effect of nozzle offset on the stability of the first radial-azimuthal mode. Red corresponds to $R_{CB} = 0.6$ and blue corresponds to $R_{CB} = 0.3$.

First, consider the effect of nozzle position on the stability of the first radial mode as shown in Figure 29(a). Since the radial mode is axisymmetric, the azimuthal offset parameter has no effect, and the plot shows the variation of $\Re$ with R_{CB} only. Note that for a nozzle that is centered in the combustor, $\Re > 0$ and as R_{CB} increases, the flame is relatively more stable. Beyond a certain value of R_{CB}, we have $\Re < 0$ indicating that this location of the flame in the radial mode shape becomes stable. This can be attributed to the fact that for no offset, the radial velocity of the mode is fully experienced by the flame resulting in maximum heat release oscillations. However, as the flame is offset, only the normal component of this radial velocity locally at the nozzle location results in heat release oscillations which are lower than that for a centered nozzle.

Next, consider the effect of nozzle position on the stability of the first radial-azimuthal mode as shown in Figure 29(b). Since this is an asymmetric mode, both the radial and azimuthal offset have effects on the stability of the mode. The figure shows the effect of azimuthal positioning of the nozzle for two different radial offsets, $R_{CB} = 0.6$ corresponding to the red dots and $R_{CB} = 0.3$ corresponding to the blue dots. The azimuthal position variation is shown only in the range $0 \le \theta_{CB} \le \pi/2$ since for the $(1,1)$ mode, the results are symmetric about $\theta_{CB} = 0$ and $\theta_{CB} = \pi/2$ planes. As seen in the figure, the outer flames ($R_{CB} = 0.6$) are relatively more stable than the inner flames ($R_{CB} = 0.3$). Additionally, note that the inner flames are relatively more stable towards $\theta_{CB} = \pi/2$ but still have $\Re > 0$ over the entire range. In contrast, the outer flames which are relatively more stable, have $\Re > 0$ for lower azimuthal offsets and then result in $\Re < 0$ towards $\theta_{CB} = \pi/2$. This indicates that outer flames near the $\theta_{CB} = \pi/2, 3\pi/2$ azimuths are the most stable, for the chosen flame/flow parameters. These results have important implications on the design choice for nozzle positioning in can combustors with multi-nozzle configurations depending on the nature of the acoustic mode of interest.

Direct Flame Response: Center Nozzle Non-Axisymmetric Mean Flame

The models thus far, considered only mean flames that were axisymmetric. For multi-nozzle configurations that are typical of can combustors, the strong flame-flame interactions result in center flames whose shapes are not axisymmetric. An illustrative example of this point is shown in Figure 30, showing an end-on visualization of a 5-flame configuration housed in a circular combustor. Note the nearly "squircle" (square with rounded edges) cross-section of the central flame. In our prior research, we have shown that the sensitivity of the flame to helical modes is fundamentally different in axisymmetric or non-axisymmetric environments. Thus, this serves as the motivation for this model extension.

Accounting for mean flame non-axisymmetry, the evolution equations for the unperturbed flame (ξ_0) and the local flame dynamics (ξ_1) may then be written as:

$$u_{r,0}\frac{\partial \xi_0}{\partial r}+\frac{u_{\theta,0}}{r}\frac{\partial \xi_0}{\partial \theta}=u_{z,0}-s_L\left[1+\left(\frac{\partial \xi_0}{\partial r}\right)^2+\left(\frac{1}{r}\frac{\partial \xi_0}{\partial \theta}\right)^2\right]^{1/2} \tag{65}$$

$$\frac{\partial \xi_1}{\partial t}+\vec{u}_{0,T}\cdot\vec{\nabla}\xi_1=\left(u_{z,1}-u_{r,1}\frac{\partial \xi_0}{\partial r}-\frac{u_{\theta,1}}{r}\frac{\partial \xi_0}{\partial \theta}\right) \tag{66}$$

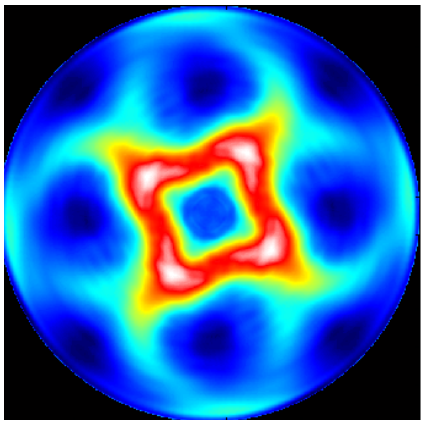

Figure 30 – Heat release intensities from the top view of a 5-flame combustor with flame-flame interactions causing a highly non-axisymmetric center flame.

For the purposes of this discussion, we shall focus on non-axisymmetries in the axial mean flow. The following mean-flow is assumed:

$$\begin{aligned} u_{z,0}(r,\theta) &= A_{z,0}(r)+\sum_{m_u}\left[A^c_{z,m_u}(r)\cos(m_u\theta)+A^s_{z,m_u}(r)\sin(m_u\theta)\right] \\ u_{r,0} &= 0 \\ u_{\theta,0}(r) &= (\sigma St)\,r \end{aligned} \tag{67}$$

Here,

$$St=\frac{\omega_0 L_f}{U_0} \qquad\qquad \sigma=\frac{\Omega}{\omega_0} \tag{68}$$

Here, St is the Strouhal number based on the acoustic and axial-convective time-scales; σ is the ratio of the acoustic to swirling-convective time-scale. The mean axial velocity has been

represented as a Fourier series of its modes (m_u) in order to denote its non-axisymmetry. Similar to the mean flow, the mean flame shape is expressed as:

$$\xi_0(r,\theta) = A_{\xi,0}(r) + \sum_{m_\xi}\left[A^c_{\xi,m_\xi}(r)\cos\left(m_\xi\theta\right) + A^s_{\xi,m_\xi}(r)\sin\left(m_\xi\theta\right)\right] \tag{69}$$

Here, the mean flame asymmetries are denoted by its Fourier modes, m_ξ .

To illustrate, consider an axisymmetric mean flow and flame that corresponded to:

$$\left.\begin{aligned} A_{z,0} &= 1 \\ A^c_{z,m_u} &= A^s_{z,m_u} \equiv 0 \end{aligned}\right\} \rightarrow \begin{cases} A_{\xi,0} = \cot\psi\left(r - \beta_R/\beta_f\right) \\ A^c_{\xi,m_\xi} = A^s_{\xi,m_\xi} \equiv 0 \end{cases} \tag{70}$$

Depending on the nature of the asymmetry in the mean flame shape, we consider non-zero values for the latter coefficients (super-scripts *c* and *s*) The frequency domain representation for the flame dynamics is given by:

$$\xi_1\left(r,\theta,t\right) = \mathrm{Re}\left\{\hat{\xi}_1\left(r,\theta\right)e^{-iSt t}\right\} \tag{71}$$

This flame response can be decomposed into its azimuthal components as:

$$\hat{\xi}_1\left(r,\theta\right) = \sum_{m=-\infty}^{\infty}\hat{\zeta}_{1,m}\left(r\right)e^{im\theta} \tag{72}$$

Representing the governing equation in the frequency domain, we have:

$$-iSt\hat{\xi}_1 + s_L\frac{\xi_{0,r}}{\sqrt{1+\xi^2_{0,r}+\xi^2_{0,\theta}/r^2}}\frac{\partial\hat{\xi}_1}{\partial r} + \sigma St\frac{\partial\hat{\xi}_1}{\partial\theta} + s_L\frac{\xi_{0,\theta}/r}{\sqrt{1+\xi^2_{0,r}+\xi^2_{0,\theta}/r^2}}\frac{1}{r}\frac{\partial\hat{\xi}_1}{\partial\theta} = -\hat{u}_{r,1}\xi_{0,r} - \frac{\hat{u}_{\theta,1}}{r}\xi_{0,\theta} \tag{73}$$

Prior research has shown that the azimuthal mode in the source terms (RHS) created the same azimuthal mode in the flame response ($\hat{\xi}_1$) since the operators and coefficients were axisymmetric. Thus, for a source acoustic azimuthal mode at $\pm m_a$, the flame response at mode *m* depends on both the mean flame shape modes $\pm m_\xi$ and $m \mp m_a$ and the flame response at mode $m \mp m_\xi$. This results in the condition: $m = \pm m_a \pm m_\xi$. This implies that different modes in the flame response are coupled to each other through the sum of the azimuthal Fourier decomposition of the mean flame and the azimuthal modes in the flow disturbances. This has important implications on how the unsteady heat release rate oscillations are spatially distributed and thus, how they couple with the azimuthally varying pressure disturbances to affect the Rayleigh Index.

In order to better understand these effects, consider the "squircle" flame configuration, mathematically expressed as:

$$\xi_0(r,\theta) = \cot\psi\left(r - \frac{\beta_R}{\beta_f}\right)\frac{\left[\left|\cos\theta\right|^{2+\mu} + \left|\sin\theta\right|^{2+\mu}\right]^{1/(2+\mu)}}{\Lambda\left(\mu\right)} \tag{74}$$

Here, note that the circular axisymmetric cross-section is obtained for $\mu \rightarrow 0$ while a sharp-cornered square cross-section is obtained for $\mu \rightarrow \infty$ and a squircle cross-section is obtained for intermediate values of μ . The normalization constant is given by:

$$\Lambda\left(\mu\right) = \frac{1}{2\pi}\int_{\theta=0}^{2\pi}\left[\left|\cos\theta\right|^{2+\mu} + \left|\sin\theta\right|^{2+\mu}\right]^{1/(2+\mu)} d\theta \tag{75}$$

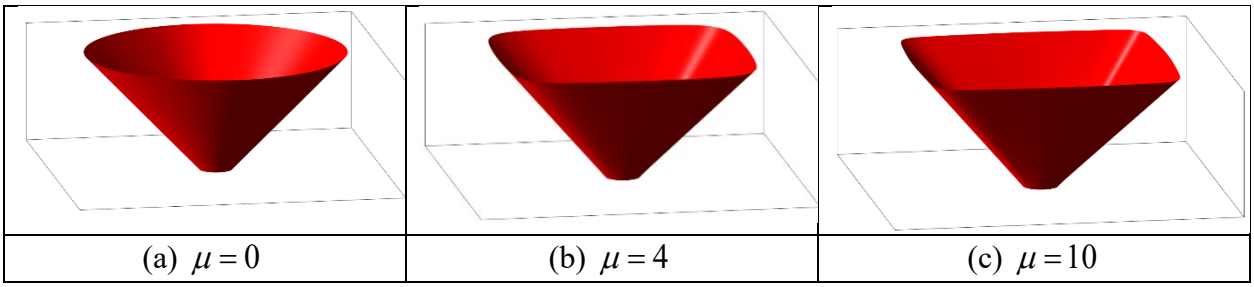

(a) $\mu = 0$	(b) $\mu = 4$	(c) $\mu = 10$

Figure 31 – Variations in flame shape with non-axisymmetry parameter, showing the isometric view of the flame from the side for: (a) axisymmetric, $\mu = 0$, (b) non-axisymmetric Squircle, $\mu = 4$, (c) non-axisymmetric Squircle, $\mu = 10$. The surface lighting is used to indicate the non-axisymmetry and the periodicity of 4.

A few representative non-axisymmetric mean flame shapes are shown in Figure 31. In order to determine the effect of the non-axisymmetry on stability, consider the ratio of the normalized Rayleigh Index from the non-axisymmetric case, with that from the axisymmetric case non-swirling case ($\mu = 0,\ \sigma = 0$), denoted by:

$$\kappa_\mu = \frac{\Re_\mu}{\Re_{\mu=0}(\sigma = 0)} \tag{76}$$

Thus, for $\kappa_\mu > 1$, implies that the mode is relatively more unstable, and vice-versa. Specifically, for $\Re_{\mu=0} > 0$, $\kappa_\mu < 0$, implies that the mode has changed from unstable to stable.

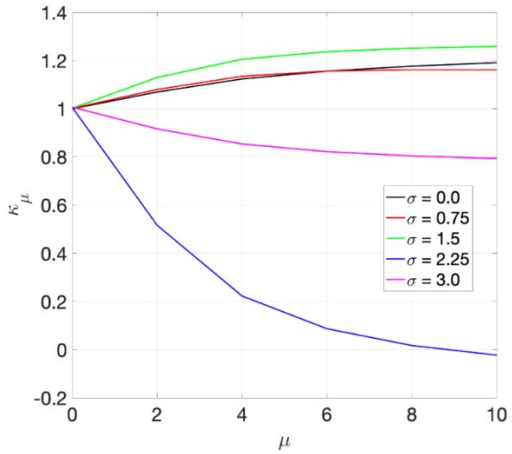

Figure 32 – Effect of mean flame asymmetry on stability of the purely-radial (2,0) mode, for different swirling strengths.

First, consider the purely radial (2,0) mode. Figure 32 shows the variation of κ_μ as we increase the degree of mean flame asymmetry (μ), for different values of swirling strength (σ). Note that, for no mean flame asymmetry ($\mu = 0$), the curves collapse to $\kappa_\mu = 1$ as for the purely radial mode, the swirling strength has no effect on stability. However, as we increase the degree of asymmetry in the mean flame, depending on the swirling strength, the mode stability changes. Note that, even in the absence of swirl (black curve), the mode stability shifts. This is due to the fact that the azimuthal flow fluctuations now directly contribute to heat release rate oscillations. It can be seen

that as the mean flame asymmetry increases, the mode becomes progressively more unstable, having a nearly 20% increase in the normalized *RI* value. As we increase the swirling strength, the mode stability shows an oscillatory trend. For the swirling strengths considered, up to $\sigma = 1.5$, the mode gets relatively more unstable with an increase of up to 25%. However, for the cases of $\sigma = 2.25$ (blue curve) and $\sigma = 3.0$ (pink curve), the mode becomes relatively more stable as the mean flame asymmetry increases. Specifically, the $\sigma = 2.25$ case shows a nearly 100% change in its normalized *RI* value. These can be attributed to net effect of complex wrinkle interference on the flame due to the swirl transport of wrinkles that changes as the mean flame surface is progressively made more asymmetric. An important observation in this example is that for the case of $\sigma = 2.25$ (blue curve), for the maximum asymmetry parameter shown ($\mu = 10$), the mode has changed from unstable to stable ($\kappa_\mu < 0$). Prior work showed that these modes were intrinsically unstable for axisymmetric flames.

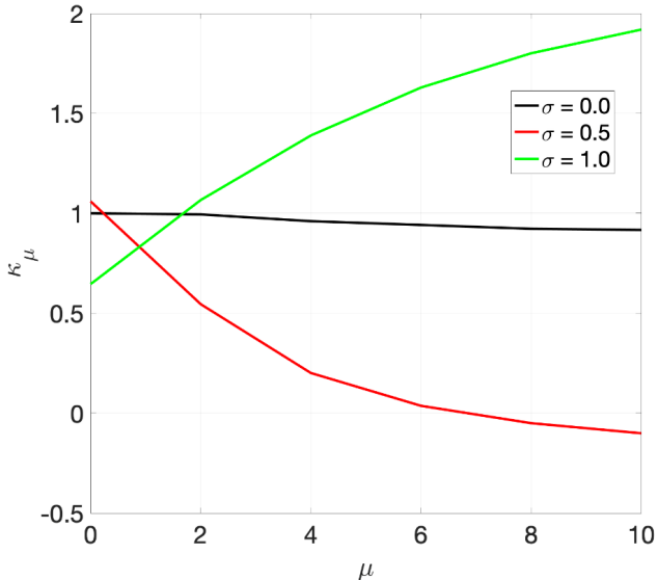

Figure 33 – Effect of mean flame asymmetry on stability of the 1-T mode (1,1), for different swirling strengths.

Next, we consider the first transverse mode (1-T) which is a mixed radial-azimuthal mode (1,1). Figure 33 shows the variation of κ_μ as we increase the degree of mean flame asymmetry (μ), for different values of swirling strength (σ). Note that, for no mean flame asymmetry ($\mu = 0$), the curves have different values. This is due to the non-axisymmetric nature of the 1-T mode. For both the non-swirling case (black curve) and the case of $\sigma = 0.5$ (red curve), the mode becomes relatively more stable as the flame asymmetry is increased. However, for the $\sigma = 1.0$ case (green curve), the mode becomes progressively more unstable. Note that the sensitivity of the mode stability for the non-swirling case, to the flame asymmetry is very less when compared to the swirling cases. For the case of $\sigma = 1.0$ (green curve), the normalized Rayleigh index is shown to increase by 200% while it decreases by nearly 125% for the $\sigma = 0.5$ case (red curve). It is also important to note that for the $\sigma = 0.5$ case (red curve), the mode changes from unstable to stable beyond a certain degree of asymmetry.

Thus, in conclusion, the results from both modes indicate that mean flame asymmetries are very crucial to the analysis of transverse modes as they can considerably shift the stability of mode for certain parameter values, and the consideration of purely axisymmetric mean flames can lead to potential erroneous deductions on mode stability.

Direct Flame Response: Uncertainty Analysis

So far, we presented such results for different flame and flow parameters which has now culminated into the studying of the sensitivity of the Rayleigh Index to the different control parameters. This is motivated by the fact that uncertainty in control parameter values in the real system means that the actual stability and the design stability may be different. Thus, it is important to identify regions where sensitivity is high and potentially unfavorable to the stability in the system. For a given mode (i.e., fixed m_a, α_{l,m_a}) and a given control parameter χ, we define the sensitivity as:

$$\delta\Re_\chi = \frac{\Delta\Re_\chi / |\Re|}{\Delta\chi/\chi} \tag{77}$$

Here, $\delta\Re_\chi$ indicates a non-dimensional change to the amplification factor with respect to a non-dimensional uncertainty in the control parameter. We perform a sweep in the $\chi \in (\psi, R_{CB}, \theta_{CB})$ space (subset of an adjoint sensitivity analysis) to determine the regions of largest unfavorable sensitivities for the amplification rates.

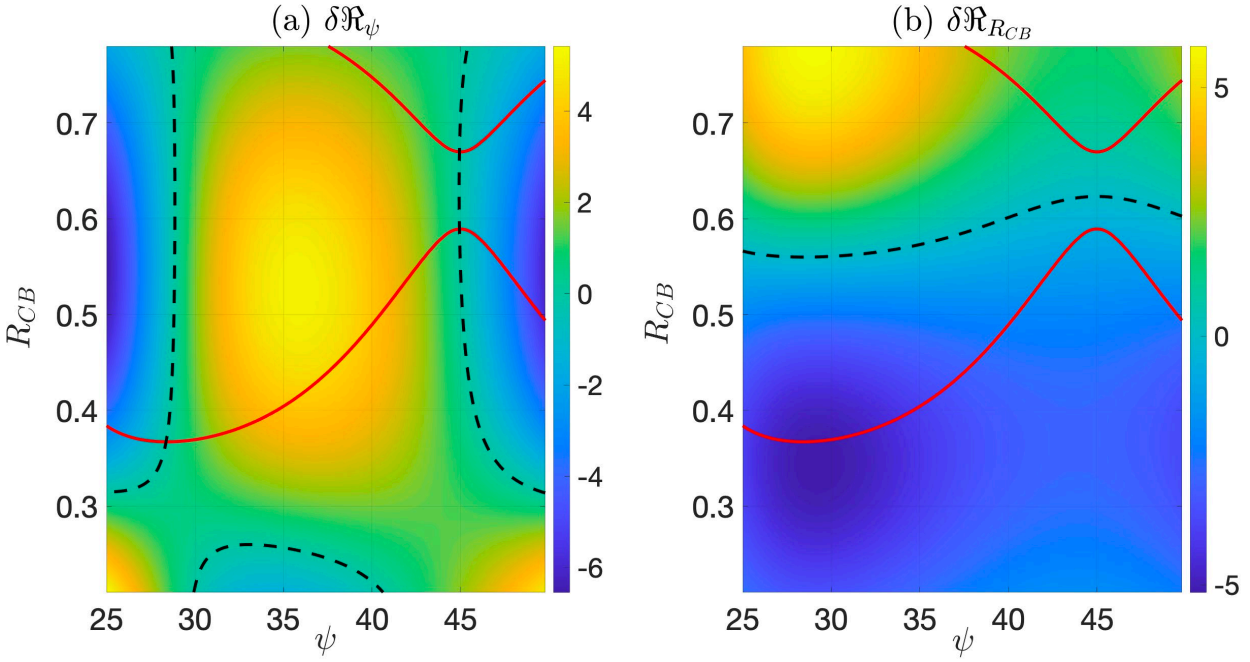

Figure 34 – Sensitivity of $\Re$ for the first radial mode $(l, m_a) = (2, 0)$ to the (a) flame angle – $\delta\Re_\psi$, and (b) radial offset of nozzle – $\delta\Re_{R_{CB}}$. The solid red curve denotes the contour $\Re = 0$ and the dashed black curves denote the respective contours for $\delta\Re = 0$.

Consider the sensitivity of the first radial mode (i.e. $(l, m_a) = (2,0)$) to changes in the flame angle (ψ) and nozzle radial offset (R_{CB}), as shown in Figure 34. Note that since this is a symmetric mode, there are no azimuthal offset effects. Between the 2 solid red curves corresponds to regions of negative amplification, i.e., $\Re < 0$. In Figure 34(a), the sensitivity color-map for $\delta\Re_{\psi}$ is shown for different radial offsets (R_{CB}) and flame angles (ψ). Note that for lower (higher) and higher (lower) flame angles (flame lengths), for larger radial offsets, changes in the flame angle are further stabilizing, i.e., in these regions, $\Re < 0$ and $\delta\Re_{\psi} < 0$. Furthermore, note that at certain points (ex. $(R_{CB}, \psi) = (0.55, 25^o)$ and $(R_{CB}, \psi) = (0.55, 50^o)$), the sensitivity is an order of magnitude higher, i.e., small changes to the flame angle cause a nearly 60 fold decrease in $\Re$. This has important implications for outer nozzles with these flame angles as small changes tend to favorably affect the system. In contrast, there is a band in the region $32^o < \psi < 40^o$, $0.4 < R_{CB} < 0.7$ where small changes to the flame angle have a strong de-stabilizing effect. Here, $\Re < 0$ but $\delta\Re_{\psi} > 0$ and in cases, the sensitivity is 50 fold, i.e. changes to $\Re$ can be up to 50 times as much as changes to the flame angle. This has important implications for outer nozzles in this flame angle band as small changes can unfavorably affect the system. Finally, if we focus on the region of neutral stability (the red curves denoting $\Re = 0$), we can see that for small and large flame angles, small changes are favorable to the system (results in $\Re < 0$) whereas for intermediate flame angles, small changes are unfavorable to the system (results in $\Re > 0$). Thus, depending on the radial offset of the nozzle and the flame angle of the flame for that nozzle, small changes to the flame angle can have substantial changes to the amplification rates for the first radial mode.

Next, consider Figure 34(b) showing the sensitivity color-map for $\delta\Re_{R_{CB}}$ for different radial offsets (R_{CB}) and flame angles (ψ). In contrast to the previous sensitivity study, note that for all flame angles considered and up to a radial offset shown by the dashed black curve, small changes to nozzle location are always favorable to the system (i.e., $\delta\Re_{R_{CB}} < 0$ regardless of the sign of the amplification rate. Specifically, in a region around $\psi = 30^o$ and $R_{CB} = 0.3$, the system has nearly neutral stability (red curve, $\Re = 0$) and small changes to the radial offset of the nozzle significantly stabilizes the system (50 fold decrease). This has important implications on considering nozzle location for response to the radial mode. Overall, for nozzle locations closer to the combustor axis, the sensitivity to change is favorable whereas for nozzles further away, the sensitivities are unfavorable. This implies that nozzles further from the combustor wall are less prone to de-stabilizing the system due to small errors in machining their location. Similar analysis has been performed for the 1-T mode $(l, m_a) = (1,1)$ drawing similar qualitative conclusions. In the next quarter, we shall expand the study to consider the significance and relevance of the direct flame response when compared to the induced axial response of the flame due to the transverse to longitudinal coupling at the combustor-nozzle juncture.

Induced Velocity Effects: Significance of Mechanism

The analysis thus far has considered only the effect of the acoustic velocity from the natural modes. The acoustic pressure oscillations at the injector lead to oscillatory axial flow into the combustor and thus an induced axial velocity disturbance at the flame. In this section, we expand the study to consider the significance and relevance of the direct flame response when compared

to the induced axial response of the flame due to the transverse to longitudinal coupling at the combustor-nozzle juncture. This study is motivated by prior studies that showed the injector coupling mechanism resulting in axial flow fluctuations as a predominant driver for the flame response. However, in the high-frequency case, the induced axial fluctuations, and the source transverse fluctuations each affect the flame through the Rayleigh criterion and thus must be explored explicitly in detail.

In this study, the nozzle location is an important geometric parameter when comparing the response between transverse and axial fluctuations. More importantly, the nozzle location results in differing induced axial fluctuations for the same transverse mode. Depending on the nature of the acoustic mode in the combustor and its pressure field, axial velocity oscillations are induced at the nozzle. The location of the nozzle within a given mode also has impacts on both the amplitude and nature of azimuthal distribution of the induced velocity. For the purpose of our modeling, we do not consider the geometric and acoustic details of the nozzle injector or any upstream section. Rather, we assume that the induced axial velocity fluctuations can be related to the pressure field at the nozzle-combustor juncture through an impedance ($\rho_0 c_0 \hat{Z}_{TL}$). Prior work by our group has shown that the induced axial velocity is related to the spatially averaged pressure field at the nozzle but incorporates the same azimuthal distribution as the pressure distribution. Thus, we consider the radially averaged pressure field at the nozzle and the induced axial velocity to be related at each azimuthal location through a specified impedance $\hat{Z}_{TL}$; i.e., the induced axial fluctuations at the nozzle outlet are given by:

$$\frac{\hat{u}_{z,N}(\theta)}{c_0} = \frac{\int_{nozzle} rJ_{m_a}\left(\alpha_{l,m_a} r_c(r,\theta)\right)\cos\left(m_a\theta_c(r,\theta)\right)dr}{\hat{Z}_{TL}\int_{nozzle} rdr} \tag{78}$$

An additional model is also needed to relate the axial velocity at the nozzle outlet to that at the flame. Here we use a traveling wave model (to denote the convection of excited vortical flow fluctuations), so that the axial velocity at the flame is given by:

$$\hat{u}_{z,1}(\theta,z) = \hat{u}_{z,N}(\theta)e^{i\alpha_{l,m_a}z} \tag{79}$$

This induced axial velocity model is used to determine the role of axial fluctuations on the overall growth/decay rate. This growth/decay rate is represented by the Rayleigh index. In this analysis we assume a constant flame speed and thus the spatio-temporal unsteady heat release is proportional to the local flame surface area oscillations. For a given mode, the growth rate due to direct excitation (denoted as $\Re_T$) will be compared to that due to the induced axial excitation (denoted as $\Re_L$) to determine the significance of the direct excitation mechanism. We shall now consider the effects of variation control parameters on the relative significance of the 2 velocity mechanisms.

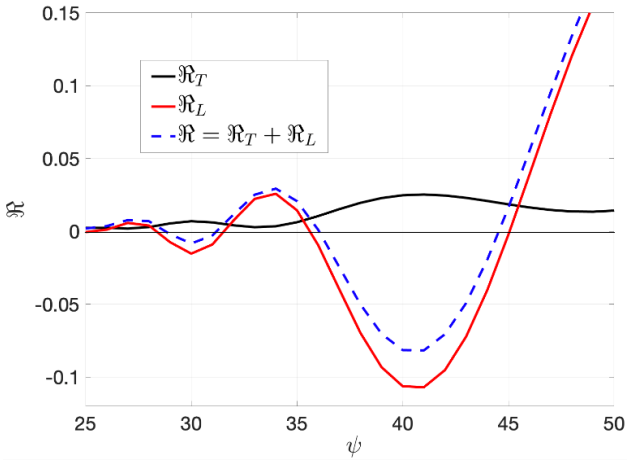

Figure 35 – Effect of flame length (shown as flame angle) on the growth rate for response to first radial (2,0) mode (black) and corresponding induced axial fluctuation (red). Net growth rate indicated by dashed blue curve.

In this example, we consider the effect of flame length (through the flame angle (ψ)) on the growth rates. First consider the response to the axisymmetric transverse radial mode $(l, m_a) = (2,0)$ and its comparison to that due to the induced axial fluctuations shown in Figure 35. For the purpose of this comparison, we set: $\beta_{R_f} = 3\beta_R = 0.15$, $M_0 = 0.1$ for a nozzle centered in the combustor (i.e., $R_{CB} = 0.0$). The nozzle impedance is set as $\hat{Z}_{TL} = 1$, which corresponds to the upstream nozzle traveling wave case, i.e., no reflected downstream acoustic waves exist. As seen in the figure, the growth rate for the transverse mode (black) is strictly positive for all cases. as shown in prior work. However, note the much larger magnitudes of the oscillatory positive and negative growth rate for the induced axial fluctuations (red). This oscillatory behavior has been alluded to before in the Introduction in the context of stability bands, as the pressure and heat release move in and out of phase. An important takeaway from this figure is that the induced axial contribution is much larger, i.e., while the natural transverse mode may have a positive growth rate, the overall growth rate can be negative in certain bands of the flame angle space. This has strong implications on the importance of the direct excitation mechanism in assessing mode behavior. As the growth rate of the induced axial fluctuations scale as $1/\left|\hat{Z}_{TL}\right|$, it is possible that under nozzle anti-resonance conditions (i.e., where the induced axial velocity is near zero), that the direct term could dominate; however, this result shows that overall, the direct term has a small magnitude relative to typical values for axial excitation.

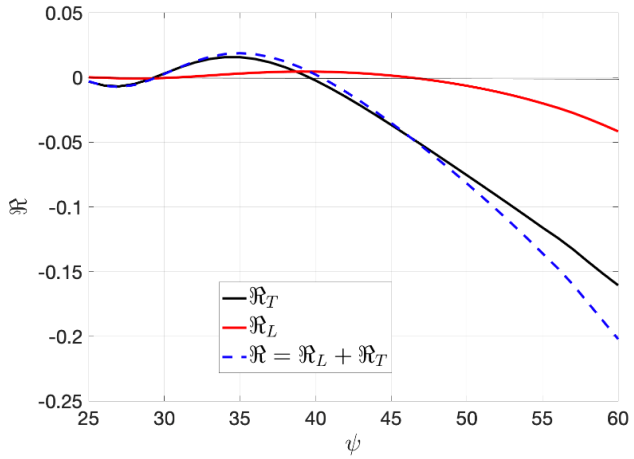

Figure 36 – Effect of flame length (shown as flame angle) on the growth rate for response to 1-T (1,1) mode (black) and corresponding induced axial fluctuation (red). Net growth rate indicated by dashed blue curve.

Next, consider the response to the first transverse mixed mode $(l, m_a) = (1,1)$ and its comparison to that due to the induced axial fluctuations shown in Figure 36. In contrast to the radial mode, the mixed mode has bands of positive and negative growth rate (see black curve) as shown in prior studies by the authors. An important result from this plot is that unlike the radial mode case, the mixed mode shows a stronger dependence of the dynamics on the direct excitation mechanism as evidenced by the total growth rate (dashed blue) and the growth rate of the transverse mode (black) closely following each other. The induced mechanism is nearly zero in this case, because the acoustic pressure has a node at the nozzle centerline. Using the axial velocity model, this implies that $u_{z,1}$ is positive on one half of the flame and negative on the other; only the fact that the flame is non-compact causes $\Re_L \neq 0$ in this case. A similar conclusion would hold for all transverse modes where $m_a \neq 0$. This implies that the direct excitation mechanism can be the dominant contributor to the growth rate, albeit with very weak amplification values. Thus, depending on the mode in question, the dominant mechanism changes.

In this next example, we consider the effect of the nozzle position (R_{CB}, θ_{CB}) on the growth rate comparisons. First, consider the symmetric radial mode, (2,0) where only R_{CB} has an effect (no effect of θ_{CB}). The comparison between the growth rates is as shown in Figure 37. For this case, we choose $\psi = 40°$ and we start with $R_{CB} \geq 2$ so that the flame surface does not pass through the origin – This is practically seen in combustors where the offset nozzle locations are chosen such that there is enough room for the center-flame. Note that as the nozzle is offset radially, the growth rate from the induced axial fluctuations varies greatly. Moreover, the growth rate changes sign at a certain radial offset location while the growth rate from the induced axial excitation remains negative. However, the overall growth rate hovers about the induced axial response (red) but is clearly affected in a non-negligible way by the transverse mode (see dashed blue curve) indicating that for certain flame angles, for nozzles that are radially offset from the combustor axis, the direct excitation mechanism is important for the first radial mode. Although not shown here, similar qualitative behavior is seen for the case of radial offset effects on the growth rate comparison for the 1-T mode.

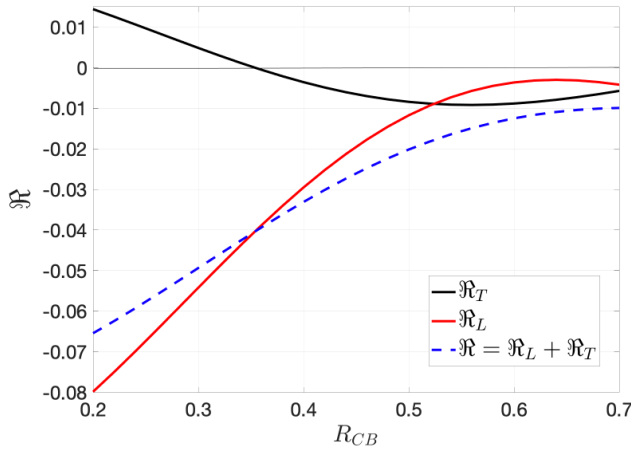

Figure 37 – Effect of radial offset of nozzle on the growth rate for response to the radial (2,0) mode (black) and corresponding induced axial fluctuations (red). Net growth rate indicated by dashed blue curve.

Next, we focus on azimuthal offset effects for the 1-T mode. For this comparison we consider the radial offset fixed at $R_{CB} = 0.3$ as the nozzle is azimuthally moved around in the combustor. First consider the flame angle case of $\psi = \pi/4$ shown in Figure 38(a). Note that as the nozzle is moved azimuthally around the combustor, the growth rate due to the induced axial fluctuations is insensitive to this movement. Also note that around $\theta_{CB} = 90°,\ 270°$, the growth rate is nearly 0 since this corresponds to the pressure nodes for the 1-T node. In contract, the direct excitation is very sensitive to azimuthal movement, as evidenced by the sharp change of the growth rate from negative to positive around $\theta_{CB} = 90°,\ 270°$. Moreover, it is clearly seen that the overall growth rate is mostly controlled by the transverse mode. This implies that outer nozzles are strongly sensitive to the direct excitation mechanism, and it is possible for the growth rate to be strongly controlled by this mechanism.

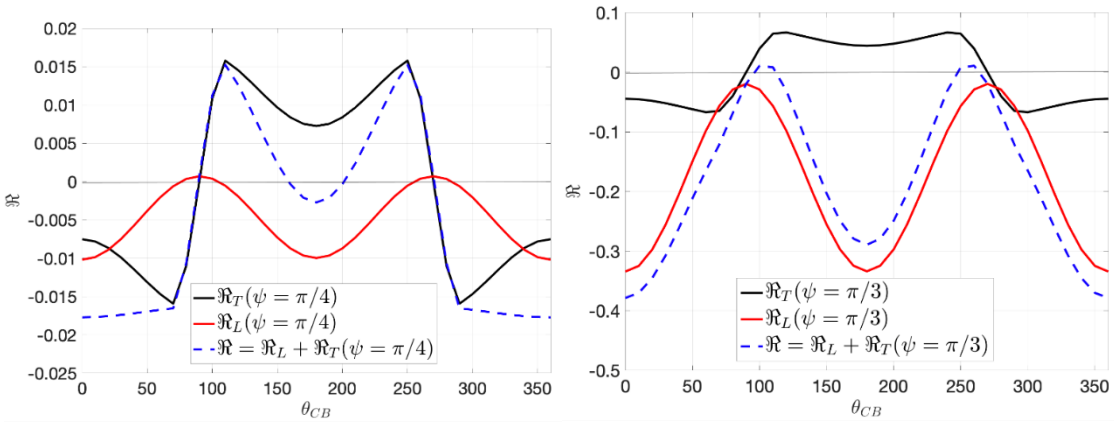

(a) $\psi = \pi/4$ **(b)** $\psi = \pi/3$

Figure 38 – Effect of azimuthal offset of nozzle (at $R_{CB} = 0.3$) on the growth rate for the response to the 1-T mode (black) and corresponding induced axial fluctuations (red). Net growth rate indicated by the dashed blue curve.

Next, consider the flame angle case of $\psi = \pi/3$ shown in Figure 38(b). Here, the sensitivity of the direct excitation growth rate (black) is lesser than that due to the induced axial mechanism. This results in the overall growth rate (dashed blue) being determined largely by the induced axial motions (red) resulting in a behavior contrary to that seen in the previous case. Thus, the azimuthal offset has differing effects on the relative response, depending on the flame length.

Thus, for nozzles centered in the combustor, the induced axial excitation dominates the growth rate for the radial (2,0) mode while the transverse excitation dominates the growth rate for the 1-T mode. For nozzles that are offset from the combustor axis, the transverse excitation mechanism was seen to be dominant for both the radial (2,0) mode as well as the mixed 1-T mode. This has important implications on modeling the combustion dynamics of multi-nozzle can combustion systems under transverse excitation.

Optimization Framework

In this section, we focus on a practical application of the modeling framework to determine optimum nozzle configurations, both in terms of positioning and operating conditions, for minimizing the Rayleigh Index. An optimization framework was developed to incorporates both the direct and induced excitation models for the overall stability of the system. The focus here is to consider multiple flames in a multi-nozzle can-combustor environment as depicted in the schematic of Figure 39. This schematic shows multiple nozzles (N = 8) around a center nozzle. Each nozzle has an anchored premixed flame.

The amplification factor for a given nozzle is given by its normalized Rayleigh index, $\mathfrak{R}^{[j]}$, which is the ratio of its Rayleigh Integral, $RI^{[j]}$, to the acoustic energy of the mode and is defined as:

$$\mathfrak{R}^{[j]} = \frac{RI^{[j]}}{2E_a} \tag{80}$$

For the linear analysis in this study, the overall stability of the multi-nozzle system is determined as:

$$\mathfrak{R} = \sum_{j=1}^{N} \mathfrak{R}^{[j]} = \frac{1}{2E_a} \sum_{j=1}^{N} RI^{[j]} \tag{81}$$

This overall growth rate is a function of the position of each nozzle ($R_{CB}^{[j]}, \theta_{CB}^{[j]}$) as well as flame/flow parameters and the acoustic mode in question (l, m_a). In the next quarter, we consider an example flow field and focus on 2 different ways in which the nozzle placing as well as operating parameter configurations can be optimized to minimize the above overall growth rate.

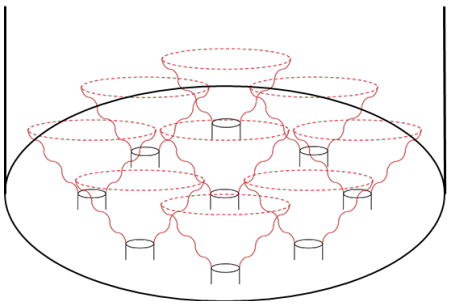

Figure 39 – Schematics showing distribution of flames in the multi-nozzle configuration.

We use the optimization framework with the same model flow fields and flame shapes as earlier to determine a combination of nozzle positions or operating parameters that can minimize the instability in the system. For nozzle *j*, the flow-field is assumed to be:

$$\left.\begin{aligned} u_{z,0}^{[j]} &= M_0^{[j]} \\ u_{r,0}^{[j]} &= 0 \\ u_{\theta,0}^{[j]} &= \frac{\Omega^{[j]} r}{c_0} = \sigma^{[j]} \alpha_{l,m_a} r \end{aligned}\right\} \Rightarrow \begin{cases} \xi_0^{[j]}(r) = (r - \beta_R^{[j]}) \cot \psi^{[j]} \\ \dfrac{s_L^{[j]}}{c_0} = M_0^{[j]} \sin \psi^{[j]} \end{cases} \tag{82}$$

Here, $\sigma^{[j]} = \Omega^{[j]} / \omega_0$ is the ratio of the acoustic timescale to the swirling timescale and $M_0^{[j]}$ is the flow Mach number for injector *j*. The center-nozzle characteristics are defined by $[j] \equiv [C]$. The above definition of the individual nozzle flow-fields and flame-shapes allows for individual selection of parameters for each of the different outer nozzles and the center nozzles. For the analysis, we focus on 2 optimization approaches –

(1) *Nozzle Optimization*: For a given set of operational flame/flow-field parameters for all nozzles, we identify the best positioning of the nozzles to minimize the overall $\Re$.

(2) *Parameter Optimization*: For a given geometric circular and even distribution of nozzles around the center nozzle, we identify the optimal flame/flow parameters that minimize the overall $\Re$.

Nozzle Optimization:

For this optimization, we keep the flame/flow control parameters fixed, namely: $\psi^{[j]}, M_0^{[j]}, \beta_R^{[j]}, \beta_{R_f}^{[j]}$, and we determine the optimal combination of $\left(R_{CB}^{[j]}, \theta_{CB}^{[j]}\right)$ that minimizes $\Re$. A classical constrained optimization approach is used. The constraints stem from how close the nozzles can be placed based on their sizing and flame extents. Note that for nozzle *j*, we assume a given flame shape, which is axisymmetric and characterized by its flame angle, $\psi^{[j]}$, and its radial extent, $\beta_{R_f}^{[j]}$. Thus, considering nozzle *j* and its neighbor *j*-1 and nozzle *j* and the center-nozzle (*C*):

$$\left.\begin{aligned} &\left(R_{CB}^{[j]}\right)^2 + \left(R_{CB}^{[j-1]}\right)^2 \\ &-2\left(R_{CB}^{[j]}\right)\left(R_{CB}^{[j-1]}\right)\cos\left(\theta_{CB}^{[j]} - \theta_{CB}^{[j-1]}\right) \end{aligned}\right\} \geq \left(\beta_{R_f}^{[j]} + \beta_{R_f}^{[j-1]}\right)^2 \tag{83}$$
$$R_{CB}^{[j]} \geq \beta_{R_f}^{[j]} + \beta_{R_f}^{[\mathrm{C}]}$$

Now, we consider the optimal nozzle positions for a differing number of nozzles (*N*) and for 2 different modes: first radial mode $(l, m_a) = (2,0)$ and 1-T mode $(l, m_a) = (1,1)$. For the following studies, we will fix the center-body and radial extent of flame as $\beta_{R_f}^{[j]} = 2\beta_R^{[j]} = 0.1$.

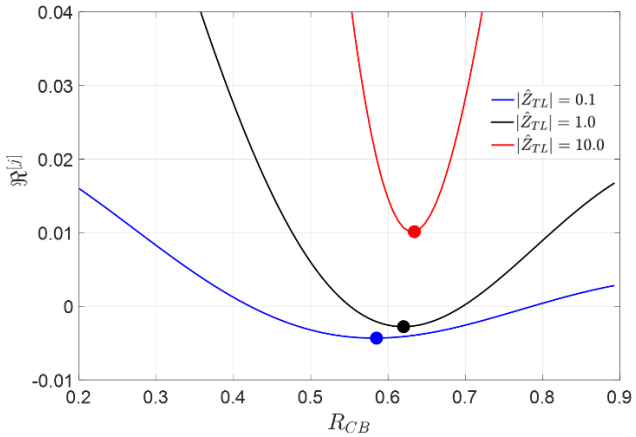

Figure 40 – Variation in growth rate for a nozzle as its radial offset is increased, for different nozzle impedances. Filled circles indicate locations of minimum growth rate.

For the first radial mode, which is a purely axisymmetric mode, only $R_{CB}^{[j]}$ is optimized since $\theta_{CB}^{[j]}$ is irrelevant. Note also that this implies, we need not select the number of outer nozzles (N). We assume the following parameters constant across all nozzles:

$$\begin{aligned} \psi^{[j]} &= \psi^{[C]} = \pi/4 \\ M_0^{[j]} &= M_0^{[C]} = 0.1 \\ \sigma^{[j]} &= \sigma^{[C]} = 0.0 \end{aligned} \tag{84}$$

Although not shown here, the results did not show strong sensitivity to the swirl parameter (σ). We will focus on the sensitivity of the optimization to the nozzle impedance, $\hat{Z}_{TL}$. Note that large values of $\left|\hat{Z}_{TL}\right|$ imply minimal impact of the induced axial mechanism and is similar to a pressure-node at the nozzle and small values denote a larger impact.

Figure 40 shows the variation of $\Re^{[j]}$ with R_{CB} for varying nozzle impedance amplitude, $\left|\hat{Z}_{TL}\right|$. Here, $R_{CB} \geq 0.2$ based on the constraints in Eq.(83). Note that for all cases, the growth rate has a minimum near $R_{CB} \approx 0.6$ (filled circles). When the nozzle impedance is increased, the minima location moves towards the wall and when it is decreased, the minima location moves towards the center. Overall, the key takeaway from this is that the nozzles are placed roughly 60% away from the center towards the wall in order to minimize the growth rate. Specifically, the minimum growth rate can be negative for certain values of the nozzle impedance, indicating that this location results in an overall stabilization of the first radial mode response. It is important to note that at this radial location, the pressure mode-shape has a node and thus results in the minimization of $\Re^{[j]}$ for flames in this region.

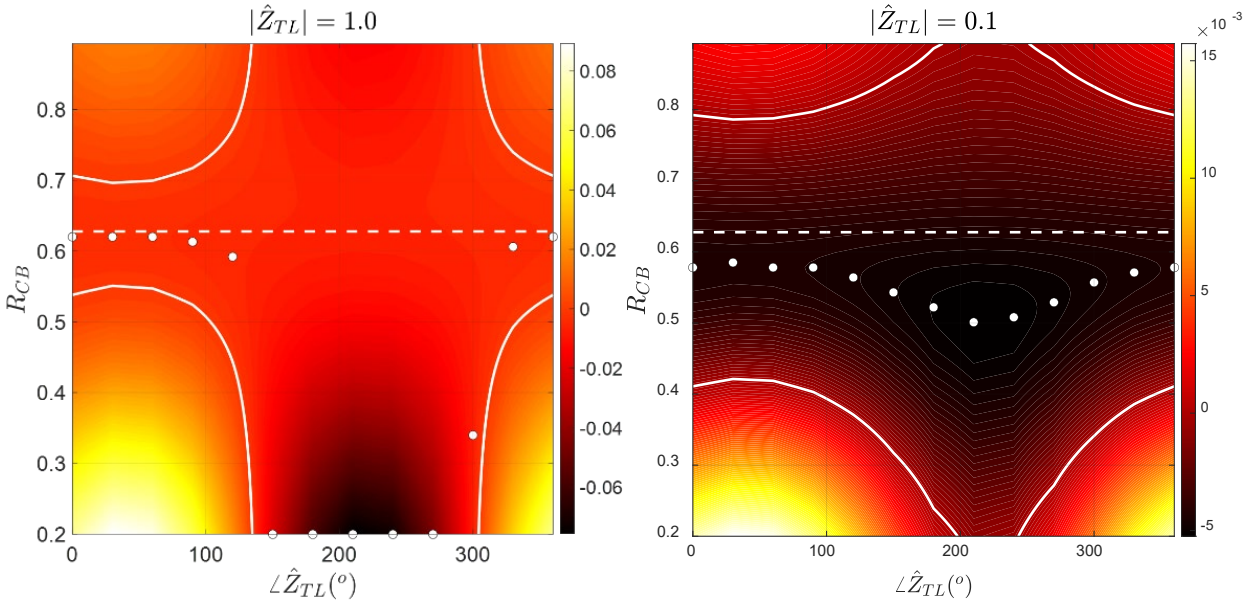

Figure 41 – Variation in growth rate for a nozzle as its radial offset (R_{CB}) is increased, for different phasing in the nozzle impedance ($\angle\hat{Z}_{TL}$). Filled white circles indicate locations of minimum growth rate for a fixed phase. Solid white lines denote contours of $\Re^{[j]} = 0$. Dashed white lines denote radial location of pressure node.

Next, consider the effect of the phasing in the nozzle impedance, $\angle\hat{Z}_{TL}$. Note that this phasing parameter greatly affects the constructive/destructive interference in the flame response to the induced axial disturbances which, in-turn affects the growth rate from the induced component and thus, the overall growth rate due to the flame on that nozzle. Figure 41(a) shows the variation of $\Re^{[j]}$ in the $R_{CB} - \angle\hat{Z}_{TL}$ space for $\left|\hat{Z}_{TL}\right| = 1.0$, for $\angle\hat{Z}_{TL} < 120°$ and $\angle\hat{Z}_{TL} > 330°$, minimum value of $\Re^{[j]}$ occurs around $R_{CB} \approx 0.6$ (filled white circles). However, when the nozzle impedance is outside this range, i.e., $120° < \angle\hat{Z}_{TL} < 330°$, the minima shift to the lowest possible location radial offset, $R_{CB} = 0.2$. Although not shown, the qualitative behavior is the same for $\left|\hat{Z}_{TL}\right| = 10.0$. Next consider the case of $\left|\hat{Z}_{TL}\right| = 0.1$ shown in Figure 41(b). Note that the variation in the minimum location is smoother and lies in the range $0.5 < R_{CB} < 0.6$ with $\angle\hat{Z}_{TL} \approx 210°$ corresponding to the closest location of the outer nozzle with respect to the center. The results indicate the growth rate is less sensitive to the phasing introduced by the nozzle impedance when the nozzle impedance amplitudes are small.

For the 1-T mode which is a non-axisymmetric mode, it requires the optimization of both $\left(R_{CB}^{[j]}, \theta_{CB}^{[j]}\right)$ depending on the number of outer nozzles, *N*. As before, we assume the following parameters across all nozzles: $\psi^{[j]} = \psi^{[C]} = \pi/4$, $M_0^{[j]} = M_0^{[C]} = 0.1$, $\sigma^{[j]} = \sigma^{[C]} = 0.0$. Figure 42 shows the optimal nozzle radial locations for different $\angle\hat{Z}_{TL}$ where $\Re^{[j]}$ is minimum. Here, $\left|\hat{Z}_{TL}\right| = 10.0$. Note that only the upper half-plane ($0 \le \theta_{CB}^{[j]} \le \pi$) is shown since the 1-T mode is

symmetric about the $0-\pi$ line. For $\angle\hat{Z}_{TL}=0$, the optimal location for the nozzles near the $\theta_{CB}^{[j]}=0$ is closer to the center nozzle whereas as $\theta_{CB}^{[j]}$ increases, around $\theta_{CB}^{[j]}=\pi/2$, the optimal location shifts to near the wall. In contrast, for $\angle\hat{Z}_{TL}=\pi/2$, for both azimuthal locations closer to $\theta_{CB}^{[j]}=0$ and $\theta_{CB}^{[j]}=\pi$, the optimal nozzle location is closer to the center while around $\theta_{CB}^{[j]}=\pi/2$, the optimal locations move further away towards the wall. Finally, for $\angle\hat{Z}_{TL}=3\pi/2$, all optimal locations are closer to the wall except around $\theta_{CB}^{[j]}=\pi/2$. The results indicate a non-monotonic trend for nozzle placement depending on the phasing for the nozzle impedances, $\angle\hat{Z}_{TL}$.

Having considered the effect of $\angle\hat{Z}_{TL}$, we next consider the effect of $\left|\hat{Z}_{TL}\right|$ as shown in Figure 43. Here we fix $\angle\hat{Z}_{TL}=0$. For the lowest impedance amplitude (higher contribution of the induced axial mechanism), note that the optimal location for all azimuthal locations is near the wall. As $\left|\hat{Z}_{TL}\right|$ is increased, note that only the region near $\theta_{CB}^{[j]}=\pi/2$ is affected where the optimal location for the nozzle moves closer to the center.

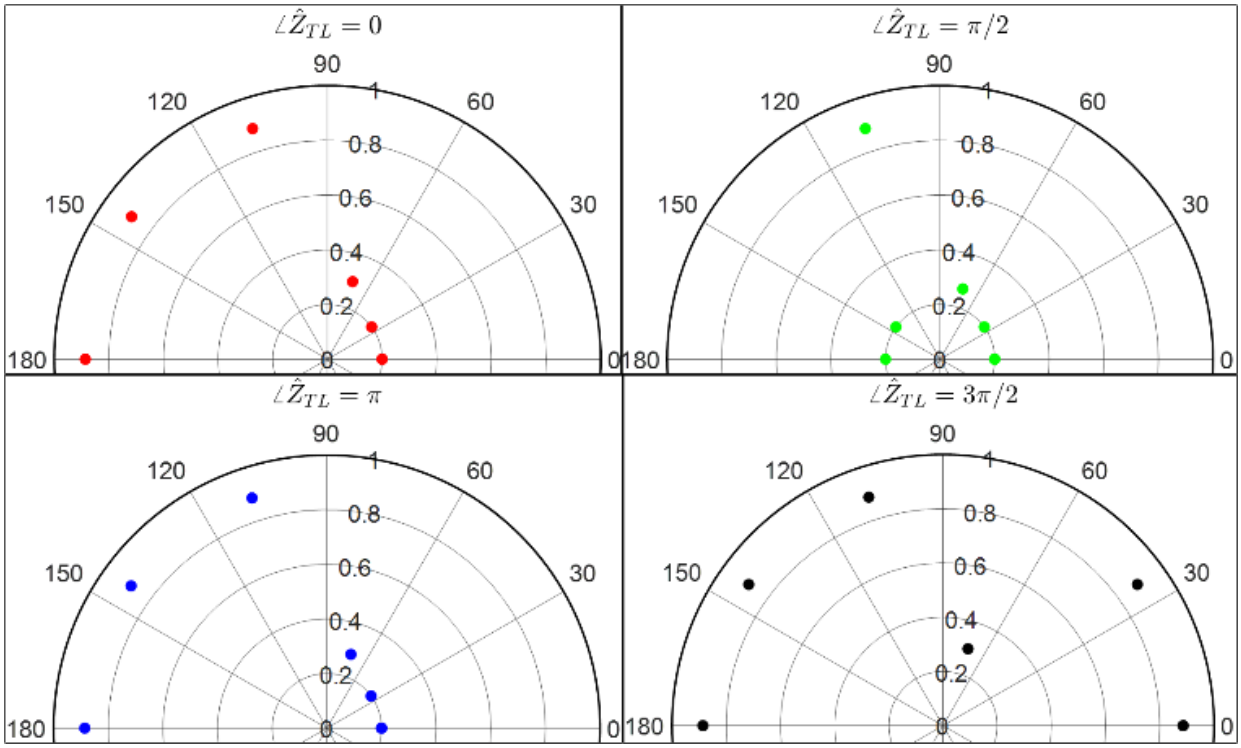

Figure 42 – Optimal radial location (R_{CB}) of nozzles at various azimuthal locations (θ_{CB}) for minimum growth rate.

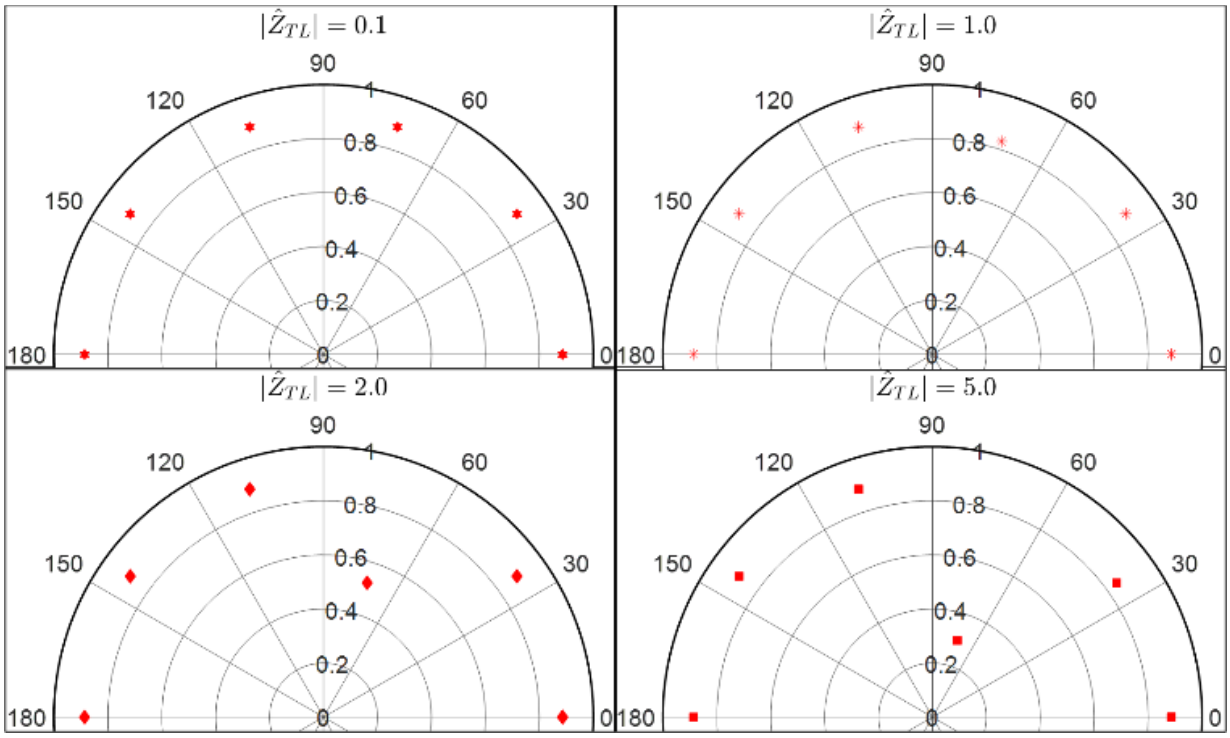

Figure 43 – Variation in growth rate for a nozzle as its radial offset (R_{CB}) is increased, for different phasing in the nozzle impedance ($\angle\hat{Z}_{TL}$). Filled white circles indicate locations of minimum growth rate for a fixed phase.

Now that we know the locations for the minima, given a certain number of nozzles *N*, we need to pick *N* locations from these, that correspond to the lowest set of values of $\Re^{[j]}$ values such that the overall $\Re$ is minimized. Consider the case of $\left|\hat{Z}_{TL}\right| = 10.0$ and $\angle\hat{Z}_{TL} = 0$ in Figure 42. For the locations shown in this figure, the variation of $\Re^{[j]}$ is as shown in Figure 44(a). Note that for all azimuthal locations, the minimum growth rate is always negative indicating that any of these locations can be chosen for an overall negative growth rate. However, note that the locations with the lowest growth rate, correspond to $\theta_{CB}^{[j]} = 0, \pi$ followed by azimuthal locations just around these points. Thus, for example, for $N = 6$ nozzles around a center nozzle, the optimal configuration that results in the lowest overall growth rate is shown in Figure 44(b). When a different nozzle impedance is considered, such as $\left|\hat{Z}_{TL}\right| = 10.0$ and $\angle\hat{Z}_{TL} = \pi/2$ in Figure 42, we can see from Figure 44(c) that for all locations the minimum growth rate is still positive. Thus, the optimal nozzle locations for this case would only minimize the positive growth rate for this mode as shown in Figure 44(d). Note that both optimal configurations are not symmetric and deviate from conventional equally distributed nozzle configurations. This indicates that the symmetric placement of nozzles can impede the overall stability of the 1-T mode. However, as discussed in the next sub-section, an optimization of the control parameters across symmetrically distributed nozzles can still result in a lower growth rate.

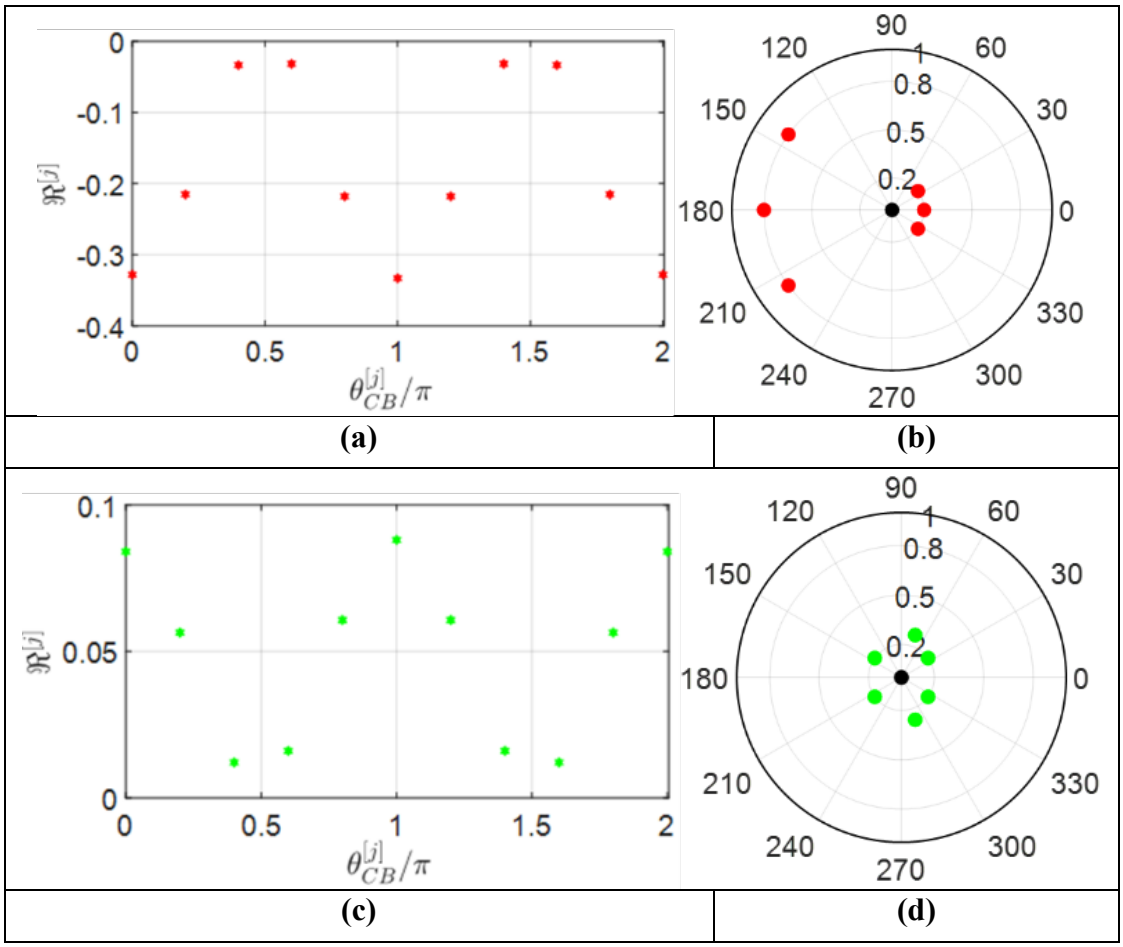

Figure 44 – Variation in minimum growth rate at different nozzle locations for (a) $\left|\hat{Z}_{TL}\right|=10.0$, $\angle\hat{Z}_{TL}=0$; (b) Corresponding optimal N = 6 configuration; (c) $\left|\hat{Z}_{TL}\right|=10.0$, $\angle\hat{Z}_{TL}=\pi/2$; (b) Corresponding optimal N = 6 configuration.

Parameter Optimization:

In the previous sub-section, we looked at unconventional but optimal distribution of nozzles for a fixed set of control parameters. However, a more practically relevant study is to consider the conventional symmetric distribution of nozzles and identify the optimal combination of flame/flow parameters that minimizes $\Re$. We shall focus on parameter optimization for fixed nozzle positions when responding to the first radial and 1-T mode.

For the first radial mode, which is a purely axisymmetric mode, $\theta_{CB}^{[j]}$ is irrelevant and hence all outer nozzles are treated to be equal but can have different flame/flow parameters than the center nozzle. For the purpose of this example, we will fix the radial offset of the outer nozzles as $R_{CB}^{[j]}=0.5$. Note that the number of outer nozzles (N) is irrelevant and hence we only determine the optimal flame angle $\left(\psi^{[j]},\psi^{[C]}\right)$ and swirl parameter $\left(\sigma^{[j]},\sigma^{[C]}\right)$ by keeping other parameters constant.

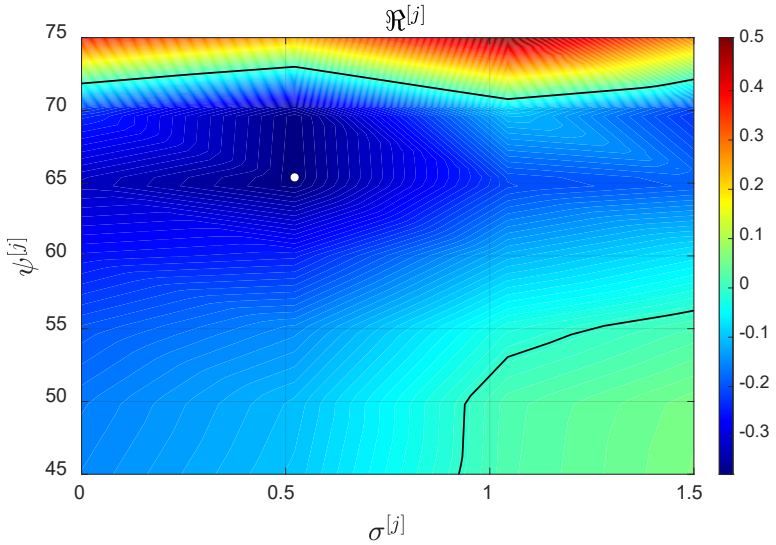

Figure 45 – Variation in growth rate with different flame angles and swirl, for first radial mode (2,0), with $\left|\hat{Z}_{TL}\right|=1.0$, $\angle\hat{Z}_{TL}=0$. White dot denotes location of lowest growth rate. Black curve denotes iso-contour corresponding to $\Re^{[j]}=0$.

Figure 45 shows the variation of the growth rate with both flame angle and swirl for an in-phase unit nozzle impedance amplitude at a radial offset of $R_{CB}^{[j]}=0.5$. Note that the minimum growth rate occurs for $\left(\psi^{[j]},\sigma^{[j]}\right)\approx\left(66°,0.52\right)$ indicated by the white dot. Thus, for nozzles fixed at $R_{CB}^{[j]}=0.5$, operating at these conditions would result in the lowest growth rate, which also happens to be negative and thus stabilizing. However, as shown in the figure, operating points within the regions enclosed by the black curves (contours of $\Re^{[j]}=0$) would all result in $\Re^{[j]}<0$ and would be suitable. Although not shown here, the center nozzle parameters corresponding to the lowest growth rate are: $\left(\psi^{[C]},\sigma^{[C]}\right)\approx\left(60°,2.6\right)$. This indicates that the center-nozzle and outer nozzles would need to operate at different conditions to minimize the overall growth rate, a feature that is followed in practical gas turbines. Note also that the center nozzle swirl is higher than the swirl for the outer nozzles.

For the 1-T mode, which is a non-axisymmetric mode, $\theta_{CB}^{[j]}$ is important and hence the distribution of the outer nozzles. We will focus on $N=6$ nozzles distributed symmetrically around a center nozzle. Similar to the previous example, we will fix the radial offset for all cases as $R_{CB}^{[j]}=0.5$. Thus, for each nozzle (i.e., each $\theta_{CB}^{[j]}$), we will determine the optimal flame angle and swirl parameter.

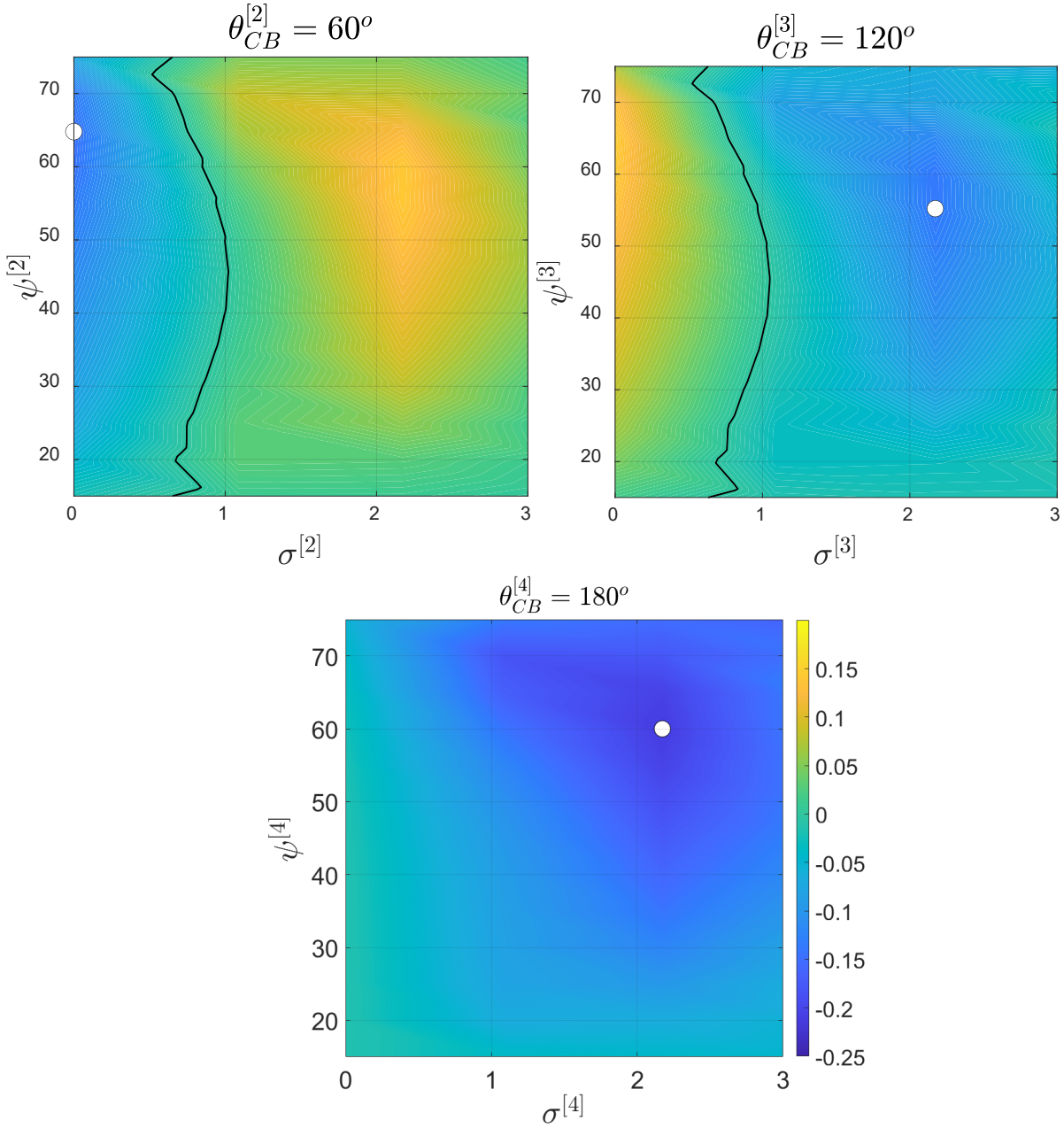

Figure 46 – Variation in growth rate with different flame angles and swirl, for nozzles numbered 2, 3, 4 for *N* = 6 responding to 1-T mode, with $\left|\hat{Z}_{TL}\right| = 1.0$, $\angle\hat{Z}_{TL} = 0$. White dot denotes location of lowest growth rate. Black curve denotes iso-contour corresponding to $\Re^{[j]} = 0$.

For $N = 6$, the nozzles are azimuthally situated at $\theta_{CB}^{[1]} = 0$, $\theta_{CB}^{[2]} = 60°$, $\theta_{CB}^{[3]} = 120°$, $\theta_{CB}^{[4]} = 180°$, $\theta_{CB}^{[5]} = 240°$ and $\theta_{CB}^{[6]} = 300°$. Note that since the 1-T mode is symmetric about the $0-180°$ plane, we focus only on the nozzles 1, 2, 3, 4 since nozzle 5 is the same as nozzle 3 and nozzle 6 is the same as nozzle 2. Although not shown here, nozzle 1 is at the pressure anti-node for the 1-T mode shape and for the parameters and location chosen, results in a minimum growth rate that is still

positive. We will focus on nozzles 2-4 to minimize their growth rate. Figure 46 shows the variation of the growth rate for these 3 nozzles with respect to both flame angle and swirl. Note that for nozzle 2 at $\theta_{CB}^{[2]} = 60°$, the optimal parameters for minimum growth rate is: $\left(\psi^{[2]}, \sigma^{[2]}\right) \approx \left(65°, 0\right)$. This corresponds to a non-swirling nozzle flow. However, as indicated by the black contour in the figure (corresponding to $\Re^{[2]} = 0$), all parameter values to the left of this curve result in a negative growth rate and can be chosen as the operating point for nozzle 2 and thus nozzle 6. Similarly, for nozzle 3 at $\theta_{CB}^{[2]} = 120°$, the optimal parameters for minimum growth rate are: $\left(\psi^{[3]}, \sigma^{[3]}\right) \approx \left(55°, 2.17\right)$. This corresponds to a swirling nozzle. As with the case of nozzle 2, the black contour in the figure (corresponding to $\Re^{[2]} = 0$) indicates that all parameter values to the right of this curve result in a negative growth rate and can be chosen as the operating point for nozzle 3 and thus nozzle 5. Finally, for nozzle 4, the plot shows that all parameter values result in a negative growth rate with the minimum growth rate occurring for: $\left(\psi^{[4]}, \sigma^{[4]}\right) = \left(60°, 2.17\right)$. Thus, apart from the center nozzle, there are 4 different operating points for the different nozzle sets: nozzle 1; nozzle 2 & 6; nozzle 3 & 5; nozzle 4. As mentioned before, this is similar to the staging of the different outer nozzles that is followed for practical multi-nozzle gas turbines.

Optimization Framework for Injectors: Hydrodynamic Considerations

In the previous framework, the coupled hydrodynamic stability of individual nozzles was not considered but are an important aspect for operability and flame dynamics. In this section, we circle back to the optimization problem where we optimize the injectors in a multi-nozzle system based on its hydrodynamic tendencies at different locations in the transverse acoustic mode.

We shall use the same base flow and acoustic flow models presented earlier. The vortical flow components stem from the hydrodynamic instability characteristics of the base flow. The velocity field along coordinate *j* is typically of the form:

$$\hat{u}_{j,1}^{v}(r,\theta,z) = \sum_{m=-\infty}^{+\infty} \hat{V}_{j,m}^{v}(r) \exp\left(-i\hat{k}_m z + im\theta\right) \tag{85}$$

The superscript *v* refers to the vortical component. Here, $\hat{V}_{j,m}^{v}(r)$ is the radially varying spatial amplitude for a given helical mode *m* at the acoustic mode frequency α_{l,m_a}. The disturbance has a complex axial wave number $\hat{k}_m$ whose real part consists of the propagation speed and imaginary part determines the axial growth/decay of disturbances. Several studies have focused on the use of a linear hydrodynamic stability framework resulting in a dispersion relation for the frequency (α_{l,m_a}), the complex wave number ($\hat{k}_m$) and the helical mode number (m). This is typically represented as:

$$\Im(\alpha_{l,m_a}, m, \hat{k}_m, \text{flow}) = 0 \tag{86}$$

Note that the helical mode number (m) is the local flow helical mode number at the nozzle and is different from the azimuthal mode number (m_a) for the natural acoustics. While a forced hydrodynamics study is more relevant to the framework, we use the linear stability framework without forcing and use the relative amplitudes of the different helical modes in the acoustic velocity at each nozzle, to scale the linear stability solutions. For a given acoustic mode (frequency

α_{l,m_a} is fixed), the different helical mode numbers at a given nozzle are determined from the modal decomposition of Eq.(64) thus fixing the range of helical modes (*m*) to be used with the dispersion relation. Thus, for each of these helical modes, the dispersion relation in Eq.(86) is then used to determine its axial wave number $\hat{k}_m$. Define the inversion of Eq.(86) as:

$$\hat{k}_m = \kappa(m, \alpha_{l,m}, \text{flow}) \tag{87}$$

Several prior studies have shown that the acoustic component determines the frequency of the disturbances and excites the vortical component but that the latter is the dominant contributor to the flame response. While it is possible to include both components for the analysis, we make this assumption to focus on illustrating how the injector parameters can be optimized to minimize $\Re$. Under this assumption, the acoustic velocity functions are still used to determine the helical mode numbers of importance. The helical mode expansion for an acoustic velocity component is defined as:

$$\begin{aligned} \hat{u}^a_{j,1}(r,\theta) &= \sum_{m=-\infty}^{+\infty} \hat{V}^a_{j,m}(r) e^{im\theta} \\ \hat{V}^a_{j,m}(r) &= \frac{1}{2\pi} \int_{\theta=0}^{2\pi} \hat{u}^a_{j,1}(r,\theta) e^{-im\theta} d\theta \end{aligned} \tag{88}$$

From Eq.(64), we can see that for the radial acoustic component, the modal amplitude is given by:

$$\hat{V}^a_{r,m}(r) = \frac{1}{2\pi} \int_{\theta=0}^{2\pi} \left[\begin{cases} \hat{u}^a_{r_c,1}(r_c,\theta_c)\cos(\theta-\theta_c) \\ +\hat{u}^a_{\theta_c,1}(r_c,\theta_c)\sin(\theta-\theta_c) \end{cases} \right] e^{-im\theta} d\theta \tag{89}$$

Note that $r_c \equiv r_c(r,\theta)$ and $\theta_c \equiv \theta_c(r,\theta)$ as shown in Eq.(63). For combustor centered injectors, the helical mode number is equal to the acoustic mode number m_a only and as the injector is offset from the center, the values of *m* where the helical mode amplitudes are non-zero is a strong function of the nozzle location and aspects of the acoustic mode of interest. The effective amplitude of a given mode *m* is defined as:

$$\upsilon^a_{r,m} = \frac{1}{R_f} \int_{r=0}^{R_f} \left| \hat{V}^a_{r,m}(r) \right| dr \tag{90}$$

Here, the integral is equivalent to the average amplitude in the region over the radial extent of the flame. Using this effective amplitude from the acoustic component we can then scale the amplitudes for the vortical components as:

$$\frac{\upsilon^v_{r,m}}{\upsilon^v_{r,m=0}} = \frac{\upsilon^a_{r,m}}{\upsilon^a_{r,m=0}} \tag{91}$$

Note that we assume the scaling is relative to the $m=0$ mode and thus we can assume $\upsilon^v_{m=0} = 1$. This assumption does not affect the goal of minimizing the overall $\Re$. For linear stability, the overall amplification factor is a linear superposition of the individual nozzle amplification factors and thus:

$$\Re = \sum_{j=1}^{N} \Re^{[j]} = \frac{1}{2E_a} \sum_{j=1}^{N} RI^{[j]} \tag{92}$$

With the many different control parameters for this configuration, in the next quarter, we consider an example flow field to illustrate how we can optimize individual nozzle hydrodynamics for overall minimization of $\Re$.

Using the same example flow-field as earlier, we shall first consider the linear stability characteristics to determine the dispersion relation. For nozzle $[j]$, the dispersion relation can be derived as:

$$\begin{aligned}&\Im(\tilde{\alpha}^{[j]}, m, \lambda_m^{[j]}, \sigma^{[j]})\\&= -\mu^{[j]}\left(\sigma^{[j]}\tilde{\alpha}^{[j]}\right)^2 + \left(\tilde{\alpha}^{[j]} - \hat{\lambda}_m^{[j]}\right)^2 \frac{K_m(\hat{\lambda}_m^{[j]})}{\hat{\lambda}_m^{[j]} K_m'(\hat{\lambda}_m^{[j]})} - \frac{\mu^{[j]}\left[\left(\varsigma^{[j]}\right)^2 - 4\left(\sigma^{[j]}\tilde{\alpha}^{[j]}\right)^2\right]}{\left[\eta^{[j]}\dfrac{J_m'(\eta^{[j]})}{J_m(\eta^{[j]})} - \dfrac{2m\sigma^{[j]}\tilde{\alpha}^{[j]}}{\varsigma^{[j]}}\right]} = 0\end{aligned} \tag{93}$$

Here, the reduced parameters are defined as:

$$\begin{aligned}&\hat{\lambda}_m^{[j]} = \hat{k}_m^{[j]}\beta_{R_f}^{[j]} \qquad\qquad \tilde{\alpha}^{[j]} = \frac{\alpha_{l,m_a}\beta_{R_f}^{[j]}}{M_0^{[j]}}\\&\varsigma^{[j]} = \tilde{\alpha}^{[j]}\left[1 - m\sigma^{[j]}\right] - \lambda_m^{[j]}\\&\eta^{[j]} = \frac{\lambda_m^{[j]}}{\varsigma^{[j]}}\sqrt{\left(2\sigma^{[j]}\tilde{\alpha}^{[j]}\right)^2 - \left(\varsigma^{[j]}\right)^2}\\&\mu^{[j]} = \frac{\rho_b^{[j]}}{\rho_u^{[j]}}\end{aligned} \tag{94}$$

Here, $\mu^{[j]}$ is the density jump across the flame at nozzle $[j]$. Accounting for density effects is important for hydrodynamic stability but for the rest of the analysis, we assume $\mu^{[j]} \equiv 1$. This has been done so that the coupling between density jump, flame speed, flame shape and swirl can be neglected as it is not analytically tractable. For a given acoustic mode (α_{l,m_a}) and chosen flow and injector geometry ($\beta_{R_f}^{[j]}$), we can determine the unknown reduced wave number ($\lambda_m^{[j]}$) for the different helical modes (m) of interest. From the above dispersion relation, we define the inverse relation as:

$$\hat{\lambda}_m^{[j]} = \kappa(\tilde{\alpha}^{[j]}, m, \sigma^{[j]}) \tag{95}$$

The velocity disturbance at the flame is defined as:

$$\hat{u}_{r,1}^{v,[j]}(r,\theta) = \sum_{m=-\infty}^{+\infty} \upsilon_{r,m}^{v,[j]} \exp\left(i\hat{\lambda}_m^{[j]}\xi_0^{[j]}(r) + im\theta\right) \tag{96}$$

The complex wave number is decomposed into its real and imaginary parts: $\hat{k}_m = k_{m,R} + ik_{m,I}$. The flame response solution for this velocity field was derived earlier as:

$$\hat{\xi}_1^{[j]}(r,\theta) = \sum_{m=-\infty}^{+\infty} \frac{\upsilon_{r,m}^{v,[j]}}{\cos^2\psi^{[j]}}\left[\frac{1 - e^{-i\hat{\chi}_m^{[j]}\xi_0^{[j]}(r)}}{i\hat{\chi}_m^{[j]}}\right] e^{\left(i\hat{\lambda}_m^{[j]}\xi_0^{[j]}(r) + im\theta\right)} \tag{97}$$

Here,

$$\chi_m^{[j]}\left(\tilde{\alpha}^{[j]}, m, \sigma^{[j]}\right) = \hat{\lambda}_m^{[j]} + \frac{\tilde{\alpha}^{[j]}}{\cos^2\psi^{[j]}}\left[m\sigma^{[j]} + 1\right] = \kappa\left(\tilde{\alpha}^{[j]}, m, \sigma^{[j]}\right) + \frac{\tilde{\alpha}^{[j]}}{\cos^2\psi^{[j]}}\left[m\sigma^{[j]} + 1\right] \tag{98}$$

For the rest of the example, we shall assume the following to be equal across all nozzles/injectors:

$$M_0^{[j]} = 0.1 \qquad \beta_{R_f}^{[j]} = 0.1 \qquad \beta_R^{[j]} = 0 \tag{99}$$

The local heat release rate can be determined and then is used to determine the Rayleigh Integral for each nozzle/injector. For a chosen nozzle location (R_{CB}, θ_{CB}) and acoustic mode ($\tilde{\alpha}^{[j]}$), we can sweep the swirl parameter ($\sigma^{[j]}$) and determine the wave numbers ($\hat{\lambda}_m^{[j]}$) at each helical mode in the flow. The overall $RI^{[j]}$ is minimized over this sweep and the optimal choice of parameters is then determined.

Before we consider the nozzles individually, consider the dispersion relation for a non-swirling injector, i.e., $\sigma^{[j]} = 0$ resulting in:

$$\frac{\left(\tilde{\alpha}^{[j]} - \hat{\lambda}_m^{[j]}\right)^2}{\hat{\lambda}_m^{[j]}} \left[\frac{K_m(\hat{\lambda}_m^{[j]})}{K_m'(\hat{\lambda}_m^{[j]})} + i \frac{J_m(i\hat{\lambda}_m^{[j]})}{J_m'(i\hat{\lambda}_m^{[j]})} \right] = 0 \tag{100}$$

From this equation, we have a solution that is independent of helical mode number, given by:

$$\hat{\lambda}_0^{[j]} = \hat{\lambda}_m^{[j]} = \tilde{\alpha}^{[j]} \tag{101}$$

And a solution that varies with helical mode number *m*, determined by:

$$K_m(\hat{\lambda}_m^{[j]}) J_m'(i\hat{\lambda}_m^{[j]}) + i J_m(i\hat{\lambda}_m^{[j]}) K_m'(\hat{\lambda}_m^{[j]}) = 0 \tag{102}$$

We shall consider 2 specific transverse mode cases as examples.

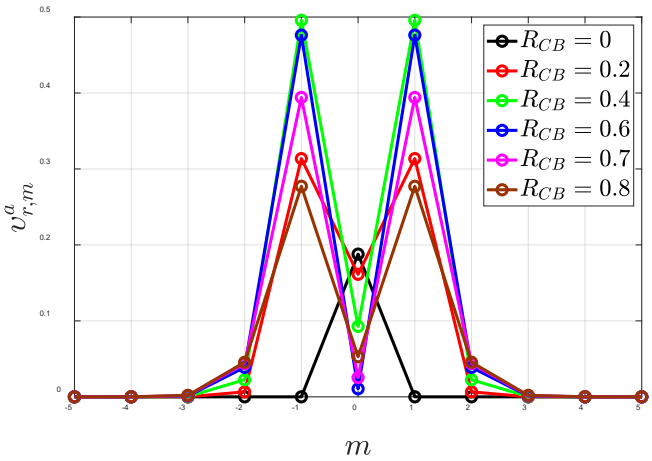

Figure 47 – Variation in effective amplitude of the radial acoustic component at the injector as a function of injector location and helical mode number for 1-R mode.

The 1-R mode corresponds to the acoustic mode numbers $(l, m_a) = (2, 0)$ with frequency $\alpha_{2,0}/2\pi = 0.6098$. First, consider the helical mode content in the acoustic velocity components as the injector is shifted from the center. Since the 1-R mode is an axisymmetric mode, the azimuthal offset (θ_{CB}) is immaterial. The coordinate transformation becomes:

$$\begin{aligned} r_c &= \sqrt{R_{CB}^2 + r^2 + 2R_{CB} r \cos\theta} \\ \theta_c &= \tan^{-1}\left(\frac{r \sin\theta}{R_{CB} + r\cos\theta} \right) \end{aligned} \tag{103}$$

The local radial velocity from the acoustic component is given by:

$$\hat{u}^{a}_{r,1}\left(r,\theta\right)=iJ_1\left(\alpha_{2,0}\sqrt{R_{CB}^2+r^2+2R_{CB}r\cos\theta}\right)\cos\left(\theta-\tan^{-1}\left(\frac{r\sin\theta}{R_{CB}+r\cos\theta}\right)\right) \tag{104}$$

Note that the azimuthal dependence results in a multitude of helical modes even though the acoustic mode is a symmetric mode. Thus, the effective amplitude can be determined as a function of both (R_{CB},m) and is shown in Figure 47. Note that the center injector ($R_{CB}=0$) shows only the axisymmetric helical mode as expected. As the nozzle is radially shifted outward, the amplitude of the axisymmetric helical mode decreases with increasing radial offset. The dominant helical modes are the $|m|=1$ modes with non-negligible amplitudes seen at $|m|=2$ as well. This has important implications as it results in "exciting" these modes in the vortical flow component.

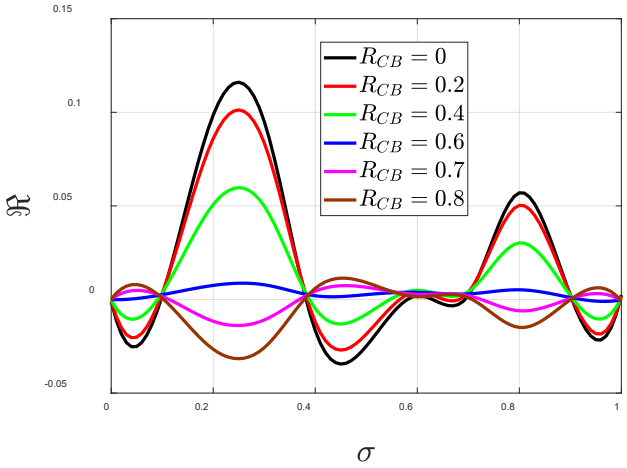

Figure 48 – Variation in amplification factor at different radial offsets and swirl for the flame response to the vortical component due to 1-R acoustic mode.

Next, consider the parameters for the vortical flow component mainly λ_m. We drop the superscript $[j]$ since this is immaterial for the 1-R mode, i.e., all nozzles would use the same parameters since there is no azimuthal offset dependence. For the 1-R mode, we have: $\tilde{\alpha}=2\pi\left(0.6098\right)$. The helical modes considered are $-2\le m\le 2$ as seen from Figure 47. We vary the swirl parameter, σ and find the solutions for λ_m. Using these solutions, we determine the $\Re$ for each σ at different radial offsets R_{CB} as shown in Figure 48. For this example, we fix all flame angles to be equal at $\psi^{[j]}=\pi/4$.

Note that at the center, $\Re$ is quite sensitive to swirl and as the radial offset increases, the sensitivity decreases to its lowest at around $R_{CB}\sim 0.6$ before a slight increase in sensitivity. For each of the radial offset locations we find that there is a swirl value where $\Re$ is minimum. The variation of the σ at minimum $\Re$ with radial offset is shown in Figure 49. Note that for injectors situated in the $0\le R_{CB}\le 0.4$, the optimal swirl parameter to minimize $\Re$ is around $\sigma\big|_{\min(\Re)}\sim 0.45$ and increases to $\sigma\big|_{\min(\Re)}\sim 0.96$ in the region around $R_{CB}\sim 0.5-0.6$ and for locations furthest from the center (closer to the outer wall), the required swirl is the lowest at $\sigma\big|_{\min(\Re)}\sim 0.25$. The region

around $R_{CB} \sim 0.5-0.6$ also corresponds to the region where the nodal line exists for the 1-R mode – a potential reason for the deviation from the swirl numbers seen closer to the center and near the walls.

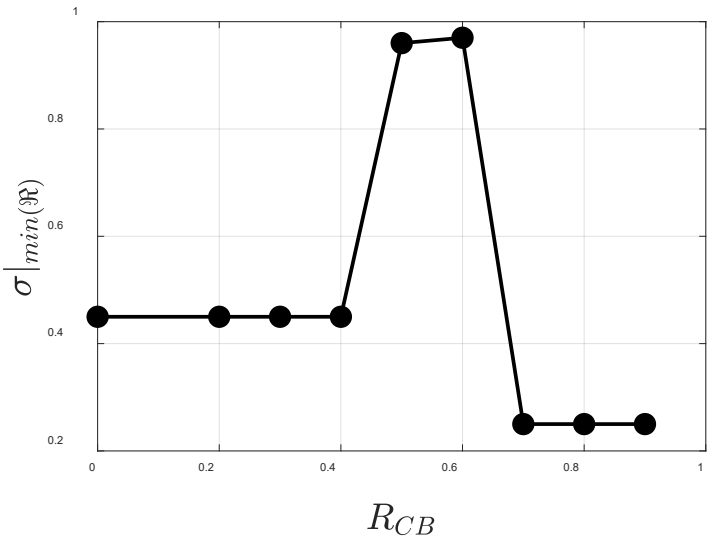

Figure 49 – Optimal swirl parameter to minimize amplification factor as a function of the radial location (R_{CB}) for the nozzle/injector.

In order to understand the key importance of the optimization study here, namely, the inclusion of hydrodynamic stability, we consider the results from the prior optimization study that used only the acoustic components. In that study it was determined that for nozzles positioned at $R_{CB} \sim 0.5$, the optimal swirl parameter to minimize $\Re$ was around $\sigma|_{\min(\Re)} \sim 0.5$. However, as seen here, the optimal swirl parameter is much higher at $\sigma|_{\min(\Re)} \sim 0.96$ indicating a strong effect of hydrodynamics on the results and thus mandating the need for including this piece of physics. Thus, depending on where the nozzles/injectors are to be positioned relative to the center, the swirler can be chosen appropriately to minimize the overall thermoacoustic response of the system. Furthermore, the inclusion of hydrodynamic stability in addition to the acoustics is important to accurately determine the optimal set of parameters.

Next, we consider the 1-T mode. The 1-T mode corresponds to the acoustic mode numbers $(l, m_a) = (1,1)$ with $\alpha_{2,0}/2\pi = 0.2930$. Like in the previous example, consider the helical mode content in the acoustic velocity components as the injector is shifted from the center. Unlike the 1-R mode which was axisymmetric, the 1-T mode is non-axisymmetric and so, both the radial (R_{CB}) and azimuthal offset (θ_{CB}) are important.

The coordinate transformation and the local radial velocity are used to determine the effective amplitude as shown in Figure 50. Each plot corresponds to a different helical mode number, each line-color corresponds to a different radial offset (R_{CB}) and the amplitude variations are with respect to the azimuthal offset (θ_{CB}). The azimuthal offset range is shown only between $0 \le \theta_{CB} \le \pi$ since the 1-T mode is symmetric about $\theta_{CB} = 0, \pi$. First consider the $m = 0$ mode

shown in Figure 50(a). As expected, the amplitude is 0 at the center (no radial offset) since 1-T is a non-axisymmetric mode. As the radial offset increases, amplitude increases indicating that the symmetric mode in the swirling flow can be increasing excited as the nozzle moves radially outward. The excitation is maximum near $\theta_{CB} = 0, \pi$ and is absent for $\theta_{CB} = \pi/2$ since this is the pressure node where the velocity field is anti-symmetric.

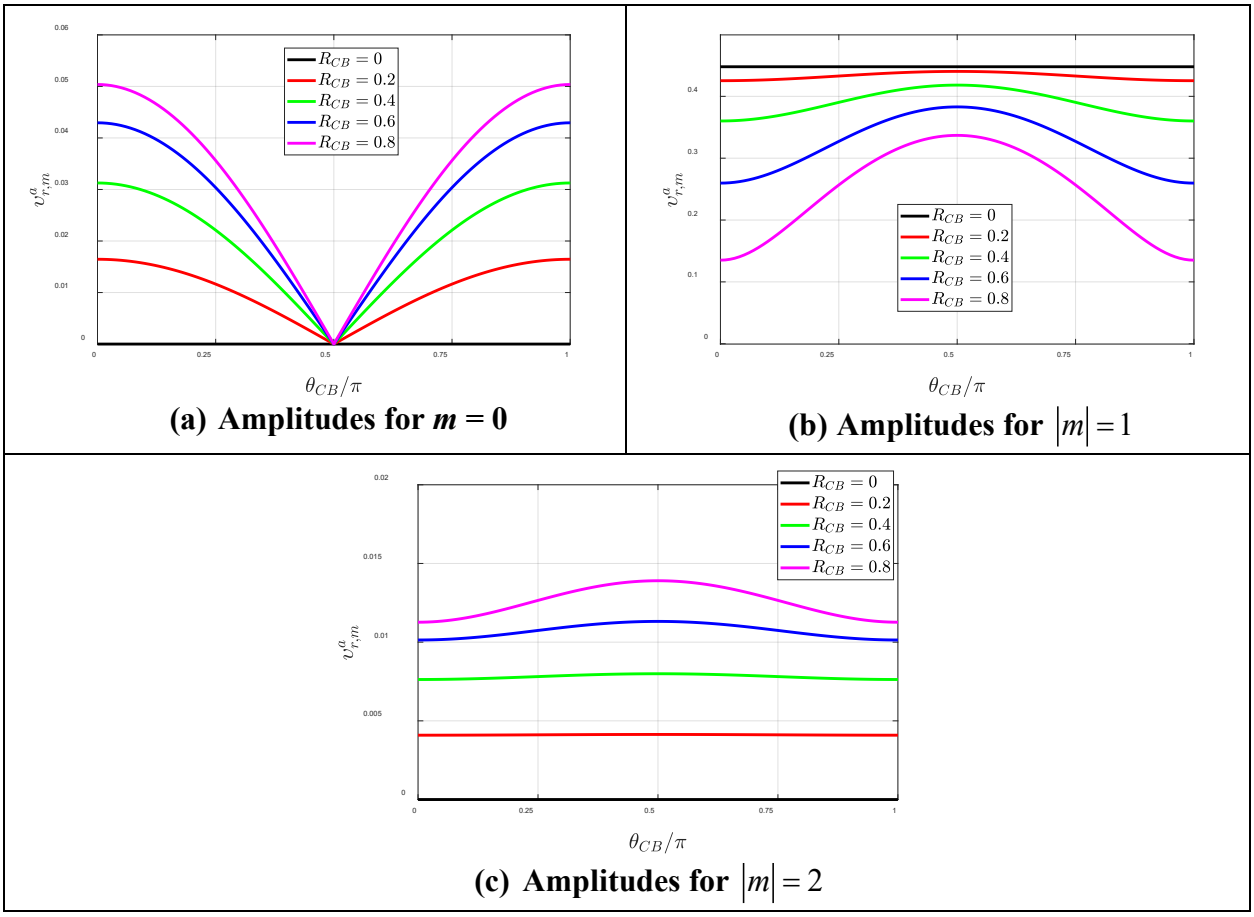

Figure 50 – Variation in effective amplitude of the radial acoustic component at the injector as a function of injector location and helical mode number, for 1-T mode.

Next, consider the $|m| = 1$ mode shown in Figure 50(b). Both the positive and negative mode numbers have the same amplitudes. The amplitude is non-zero at all locations as expected since the 1-T mode is a $m = 1$ mode about the centerline. The peak values for the amplitudes are seen at $\theta_{CB} = \pi/2$ since the velocity field is anti-symmetric at this point. However, note that as the radial offset increases, the amplitude decreases. This is due to the increase in dominance of the symmetric mode which reduces the amplitude of this mode. Finally, for the $|m| = 2$ mode shown in Figure 50(c), note that the amplitude peaks at the pressure node location and decreases away from it. The amplitudes also increase with increasing radial offset. Overall, the $|m| = 1$ amplitudes dominate the velocity field followed by the axisymmetric mode. Higher order modes, though not shown, are present but are of negligible amplitude.

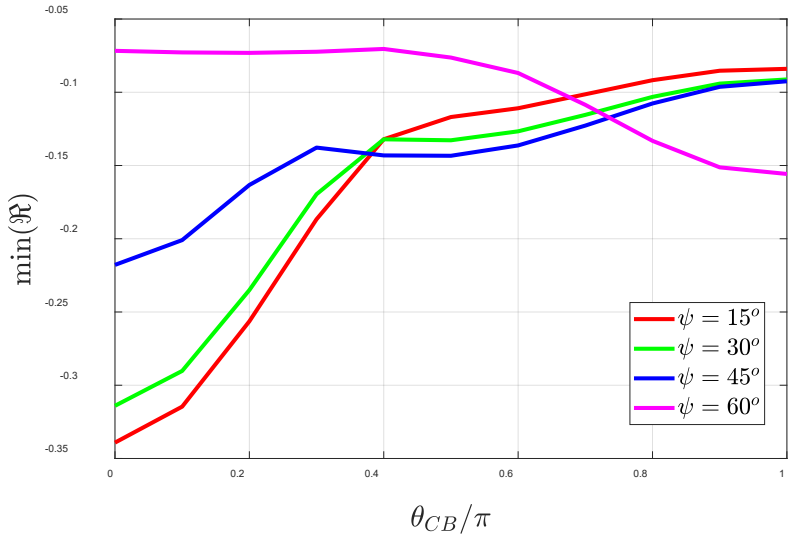

Figure 51 – Variation in the minimum $\Re$ at different azimuthal offset locations for different flame angles.

For the optimization study in this example, we shall vary both the swirl number and the flame angle but for nozzles at a fixed radial offset of $R_{CB} = 0.5$. We shall consider a discrete set of flame angles: $\psi^{[j]} = 15°, 30°, 45°, 60°$ to illustrate how different flame angles can behave in very different ways across the combustor dump plane (varying θ_{CB}). Note that a more rigorous optimization is possible that finds the more precise flame angle for a given set of parameters, but this has not been considered for the example. The focus of this example is to show how this property changes with nozzle location due to changes to its local hydrodynamic stability characteristics. The swirl parameter range being explored is: $-1 \le \sigma^{[j]} \le 1$, allowing for swirl in both clockwise and anti-clockwise directions. Note that unlike the 1-R example where the nozzle number was immaterial, here the nozzle number, i.e., the azimuthal offset/location is important and results in differing values for optimization.

First consider the minimum $\Re$ that is possible at each azimuthal location for the different flame angles, as shown in Figure 51. Note that for the lower flame angles (15-45 degrees), the minimum possible $\Re$ increases as the azimuthal offset increases and for the largest flame angle (60 degrees), the trend is reversed. A key takeaway from this figure is for nozzles closer to $\theta_{CB} = 0$, the lower flame angles are preferred since they offer the lowest of the minimum $\Re$ values. However, at $\theta_{CB} = \pi$, the largest flame angle provides the lowest of the minimum $\Re$. At the intermediate locations, the choice depends on the number of nozzles in the system. For a 4 around 1 configuration, we have nozzles at: $\theta_{CB}^{[1]} = 0$, $\theta_{CB}^{[2]} = \pi/2$, $\theta_{CB}^{[3]} = \pi$ and $\theta_{CB}^{[4]} = 3\pi/2$. Thus, we have: $\psi^{[1]} = 15°$, $\psi^{[3]} = 60°$ as discussed above. Both nozzles $j = 2, 4$ are identical due to the relative position in the pressure mode shape and from Figure 51 it is evident that the optimal flame angle is: $\psi^{[2]} = \psi^{[4]} = 45°$. This shows for the best possible stability, all injectors cannot have the same flame angle.

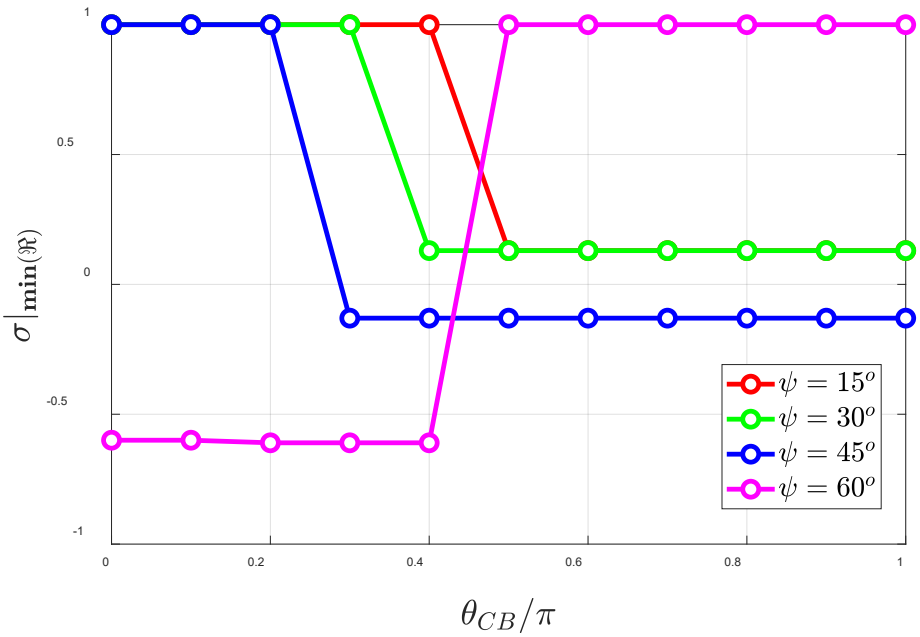

Figure 52 – Variation in optimal swirl parameter for minimum $\Re$ at different azimuthal offset locations for different flame angles.

An additional optimal parameter to consider is the optimal swirl parameter for each of the above cases, as shown in Figure 52. Since $\psi^{[1]} = 15°$, the swirl number for this nozzle is $\sigma^{[1]} = 1$ as shown in the figure. Similarly, for $\psi^{[3]} = 60°$, we have: $\sigma^{[3]} = 1$. Finally, for $\psi^{[2]} = \psi^{[4]} = 45°$ at $\theta_{CB} = \pi/2$, we have: $\sigma^{[2]} = \sigma^{[4]} = -0.2$ indicating that these injectors must have clockwise swirl when compared to the anticlockwise swirl of the other 2 injectors. Collectively, for $N = 4$ we have:

$$\begin{aligned} j = 1 &\rightarrow \theta_{CB}^{[1]} = 0 \rightarrow \psi^{[1]} = 15°, \sigma^{[1]} = 1.0 \\ j = 2 &\rightarrow \theta_{CB}^{[2]} = \pi/2 \rightarrow \psi^{[2]} = 45°, \sigma^{[2]} = -0.2 \\ j = 3 &\rightarrow \theta_{CB}^{[3]} = \pi \rightarrow \psi^{[3]} = 60°, \sigma^{[3]} = 1.0 \\ j = 4 &\rightarrow \theta_{CB}^{[4]} = 3\pi/2 \rightarrow \psi^{[4]} = 45°, \sigma^{[4]} = -0.2 \end{aligned} \tag{105}$$

As an additional example, consider the case of $N = 6$ injectors, located at: $\theta_{CB}^{[1]} = 0$, $\theta_{CB}^{[2]} = \pi/3$, $\theta_{CB}^{[2]} = 2\pi/3$, $\theta_{CB}^{[2]} = \pi$, $\theta_{CB}^{[2]} = 4\pi/3$ and $\theta_{CB}^{[2]} = 5\pi/3$. Note that nozzles $j = 2,6$ are identical due to the relative position in the pressure mode shape and so are nozzles $j = 3,5$. From Figure 51 and Figure 52, the optimal flame angle and swirl parameters for $N = 6$ are:

$$
\begin{aligned}
&j=1, \theta_{CB}^{[1]}=0 \rightarrow \psi^{[1]}=15°, \sigma^{[1]}=1.0 \\
&j=2, \theta_{CB}^{[2]}=\pi/3 \rightarrow \psi^{[2]}=15°, \sigma^{[2]}=1.0 \\
&j=3, \theta_{CB}^{[3]}=2\pi/3 \rightarrow \psi^{[3]}=45°, \sigma^{[3]}=-0.2 \\
&j=4, \theta_{CB}^{[4]}=\pi \rightarrow \psi^{[4]}=60°, \sigma^{[4]}=1.0 \\
&j=5, \theta_{CB}^{[5]}=4\pi/3 \rightarrow \psi^{[5]}=45°, \sigma^{[3]}=-0.2 \\
&j=6, \theta_{CB}^{[6]}=5\pi/3 \rightarrow \psi^{[6]}=15°, \sigma^{[4]}=1.0
\end{aligned}
\tag{106}
$$

We can see that the injectors must be operated with very different flame and flow parameters for optimal system stability. This contrasts with the prior optimization that considered only the acoustic components, wherein the optimal flame angle was determined to be around 55-60 degrees for all nozzles. Thus, the inclusion of the vortical mode, which is often the dominant flame response driver, also has significant impact on the results of the optimization.

Summary

To summarize, the flame response modeling task in this program addressed several different levels of fidelity and considerations for the flame configuration and position in a multi-nozzle system.

1. Nozzle positioning studies helped understand how flame dynamics changed for centered nozzles vs. outer nozzles and for different azimuthal locations of outer nozzles.
2. Mean flame shape studies were performed to understand how changes in mean flame shape can affect stability. Specifically, it was shown that purely-radial modes which were considered to be unconditionally and intrinsically unstable for axisymmetric mean flames, can be stable for increased mean flame asymmetries for certain swirling strength values.
3. The geometric nature of the injector connected to the combustor implies that the natural transverse acoustic mode induced axial velocity disturbances. Models were considered to account for both mechanisms and the relative importance of the 2 mechanisms were studied. For nozzles centered in the combustor, the radial mode response was seen to be insignificant when compared to the induced axial response. In contrast, the opposite was seen for the 1-T mode. When the nozzles were offset from the combustor axis, it was shown that depending on the radial offset, azimuthal offset, and flame angle, either mechanisms could be dominant or both mechanisms could be collectively important. This implies that depending on flame properties and the nozzle in question (in the multi-nozzle can), modeling the growth rate may require the inclusion of the induced axial mechanism along with the direct excitation mechanism.
4. Given the above studies on single nozzles, a natural extension was the multi-nozzle study for which an optimization framework was developed to understand how we can optimize both nozzle positioning and nozzle operation for the best stability of the overall system. The nozzle optimization study for the (2,0) radial mode indicated that outer nozzles must be located around 60% of the radial distance to the outer wall. This also corresponds to the region near the pressure node for the radial mode shape. However, the nozzles can be placed symmetrically in the combustor. In contrast, since the 1-T mode shape is non-axisymmetric, depending on the number of nozzles, the radial offset at different azimuthal locations were seen to be different. The resulting nozzle locations deviated significantly from conventional symmetric nozzle placements seen in gas turbines. While the optimum locations are not generally practically feasible, it sheds light on how the lowest possible

growth rate requires drastically different nozzle placements. The parameter optimization study is the more practically relevant study where multiple outer nozzles are placed symmetrically around a center nozzle and each nozzle can have different operating parameters. For the first radial mode, an optimal combination of flame angle / nozzle swirl was identified for the lowest growth rate, but it was seen that a large parameter space existed where the growth rate was still negative. For the 1-T mode study, a 6 around 1 configuration was used, and it was shown that apart from the center nozzle, 4 different operating parameters must be used across the outer nozzles to minimize the growth rate (i.e., the different nozzles would require different operating conditions). This is similar to staging concepts used for the multiple outer nozzles in practical gas turbines.

5. Finally, the optimization study was extended to consider the hydrodynamic stability characteristics of individual injectors. The flow disturbances affecting the flame response comprise of the natural acoustic velocities and the excited vortical flow components from the interaction of acoustics with the natural hydrodynamics of the mean flow. The optimization model was applied to injectors positioned at different locations and responding to the 1-R mode and the 1-T mode in separate examples. The results showed that optimal parameters such as the swirl parameter can be determined depending on the location of the injector. This helps provide a design guidance to optimize injectors with swirlers that lead to an overall improvement in thermoacoustic stability. Furthermore, the results from including hydrodynamics were starkly different from prior work where only acoustics was considered, thus mandating the need for hydrodynamic stability modeling.